UNIVERSITY OF CALIFORNIA

Los Angeles

Studying and Controlling the Structure of Doped Semiconducting Polymers

A dissertation submitted in partial satisfaction of the

requirements for the degree

Doctor of Philosophy in Chemistry

by

Yutong Wu

2022

ABSTRACT OF THE DISSERTATION

Studying and Controlling the Structure of Doped Semiconducting Polymers

by

Yutong Wu

Doctor of Philosophy in Chemistry

University of California, Los Angeles, 2022

Professor Sarah H. Tolbert, Chair

This thesis focuses on studying and controlling the structure of pristine and doped semiconducting polymers. Semiconducting polymers have many applications in flexible electronics due to their structural tunability, low cost and solution processability. Intrinsically, semiconducting polymers have poor conductivities due to a lack of mobile carriers. Charge transfer between a semiconducting polymer and a dopant molecule is necessary to introduce carriers into a polymer system. If an electron is fully transferred, commonly called “integer charge transfer (ICT)”, this will result in a polaron and a dopant anion. On the other hand, the electron charge could be shared between the polymer and a dopant molecule to form a “charge transfer complex (CTC)”. In the first part of the thesis, we explored factors that affect the charge transfer pathways in doped semiconducting polymers and were able to control the formation of CTCs.

Semiconducting polymers are composed of both crystalline and amorphous parts. Compared to crystalline regions, amorphous polymer parts are disordered, thus the dopant anion are usually close to the polarons, resulting in poor carrier mobility due to columb attraction between polarons and counterions. CTCs also tend to form in amorphous polymer regions compared to crystallites and result in less carriers due to the charge sharing nature of CTC. In our second project, we explored ways to suppress the formation of both CTCs and localized carriers even in highly amorphous polymer films, using large boron cluster-based dopants. The electron density of these dopants is core-localized and is shield from the holes on the polymer, resulting in increased crystallinity and higher film conductivities. In our third project, we further explored how polymer crystallite orientation influences the ease of doping and found that polymer regions with structures similar to the final doped structure could be doped more easily. In the last chapter, we designed amphiphilic semiconducting polyelectrolytes that form ordered cylindrical micelles in water. Our results demonstrate that we can achieve relatively precise control between electron donor and acceptor co-assemblies by varying the structural properties of component amphiphilic polymers and acceptors, which can provide guidelines for designing systems with controllable excited-state transfers.

The dissertation of Yutong Wu is approved.

William M. Gelbart

Justin R. Caram

Richard B. Kaner

Sarah H. Tolbert, Committee Chair

University of California, Los Angeles

2022

To my parents, my love, and everyone
who supports me along the way

TABLE OF CONTENTS

List of Figures & Tables

ACKNOWLEDGMENTS

It has been a long journey since I came to UCLA chemistry department in Fall 2017. There are a couple of people I want to acknowledge here who shape me to who I am.

I want to thank my parents Yuying Ding and Guosheng Wu for supporting and loving me all the time. They give me the courage to be myself and I know that they will always back me up no matter what choice I make.

My partner Bocheng Cao is my biggest mental support in graduate school. We went through countless happiness, bitterness together in the past years and I am glad we both get Ph.D. now

I would like to thank my advisor Prof. Sarah Tolbert. She helped me grow to a scientist and form a researcher mindset. She can always give students insightful research instructions and help students grow. She is also a great presenter and makes us realize the importance of giving good presentations. I definitely appreciate the presentation skills I learned in the Tolbert group. More importantly, she is a role model for us as a female scientist. I become more tough and strong over the years and have a clear goal for my career path.

I also want to thank Prof. Benjamin Schwartz and Prof. Yves Rubin for their advices and help on all the projects that I collaborated with their group. I gratefully acknowledge Prof. William Gelbart, Prof. Richard Kaner and Prof. Justin Caram for being my committee members. They all helped me at different times.

None of the projects could be done without my collaborators. Alex Simafranca, I appreciate your talent, capability and curiosity when I know you more and more. We are really good research partners and collaborated on a few cool papers together. It is the experience discussing research with you that assures myself that I really like doing research. I will always remember those

afternoons in the group office when we discussed science together. Dane Stanfield collaborated with me on the CTC project. He found the interesting spectroscopy data and started our project, which turns out to be a really interesting one. I really enjoy working with you and I appreciate that you are always calm when most people around are stressed. Quynh Duong is my collaborator who not only does good research, but also has the ability to build devices and make things work. He spent tremendous efforts rub-aligning the polymer and it turns out to be a great platform for a bunch of projects. Charlene Salamat organizes the synchrotron very well for our group. She helps us keep getting beamtimes without which we could not have gathered so many data. We also work on a bunch of projects closely in the last two years. Omar Ruiz is very helpful and nice. He tells you everything he knows when you ask him for help. It's great that we get one paper together.

I want to name my friends in Tolbert lab as well as in Chemistry department. Joe Mazzetti is my best lab buddy. We went through a lot together since we were in first year. We are comfortable to share our feelings with each other and your support is a huge thing to me when I was really stuck in my first two years. Yiyi Yao is very nice and friendly, I felt welcomed by her when I joined the group and we ate many hotpots together. Stephen Sasaki, Ty Karaba, Jeff Kurish, Matthew Voss helped me with my experiments at different times. I also had many funs with Jinhui Xu, Jun Shen, Yao Gong, Xun Guan, Jiahui Lu in the past few years.

Finally, I want to thank myself for never giving up no matter how tough life is, and persisting to the last.

Chapter 2 is a version of Stanfield, D. A.; Wu, Y.; Tolbert, S. H.; Schwartz, B. J. "Controlling the Formation of Charge Transfer Complexes in Chemically Doped Semiconducting Polymers". Chem. Mater. 2021, 33, 7, 2343–2356. Copyright (2021) American Chemical Society. The full article can be accessed at https://pubs.acs.org/doi/10.1021/acs.chemmater.0c04471?ref=pdf. This

work was supported by the National Science Foundation under grant number CHE-20003755. Use of the Stanford Synchrotron Radiation Lightsource, SLAC National Accelerator Laboratory, is supported by the U.S. Department of Energy, Office of Science, Office of Basic Energy Sciences under Contract No. DE-AC02-76SF00515. This project was inspired by Dane and Tyler Scholes. Dane took and analyzed all the spectroscopy and conductivity data. I took and analyzed all the GIWAXS data. Jonathan Onorato synthesized the highly regioregular P3HT, UV-Vis-NIR and FTIR data for the varied crystallinity study was acquired and provided by Tyler Scholes. All coauthors assisted in editing the manuscript. The PIs and/or project directors were: Benjamin Schwartz and Sarah Tolbert.

Chapter 3 is a version of Wu, Y.; Salamat, c.z.; Ruiz, O.L.; Simafranca, A. F.; Wu, E. C.; Doud, E.; Lindemuth, J. R.; Phan, M. D.; Spokoyny, A. M.; Schwartz, B. J.; Tolbert, S. H. "Bulky Charge-Shielding Dodecaborane-Based Dopants: An Effective Strategy Towards the Production of Mobile Charge Carriers in the Amorphous Regions of Semiconducting Polymers". This work was supported by the National Science Foundation under grant number NSF DMR-2105896. This research used resources at the Advanced Photon Source (APS), a U.S. DOE Office of Science User Facility operated by Argonne National Laboratory (ANL) under contract No. DE-AC02-06CH11357. Research at the Spallation Neutron Source, a U.S. DOE Office of Science User Facility operated by the Oak Ridge National Laboratory (ORNL) was sponsored by the Scientific User Facilities Division, Office of Basic Energy Sciences, DOE. Use of the Stanford Synchrotron Radiation Lightsource (SSRL), SLAC National Laboratory, is supported by the U.S. DOE Office of Science, Office of Basic Energy Sciences under contract No. DE-AC02-76SF00515. I made all the samples, took the spectroscopy data and analyzed all the X-ray and neutron reflectometry (NR) data. I also wrote the first manuscript of the paper. Charlene took the GIWAXS data and helped

with NR analysis, manuscript editing. Omar took the conductivity of the films. Alex took the GISAXS data and came up with explanation. Alex also rewrote most of the manuscript. Eric helped with RRa P3HT structure simulation. Evan synthesized the boron cluster. Jeffrey took the AC-Hall data. Minh took the NR data. Sarah and Ben gave research suggestions and edited the final manuscript. The PIs and/or project directors were: Alexander Spokoyny, Benjamin Schwartz and Sarah Tolbert.

Chapter 4 is a version of Wu, Y.; Duong, Q.; Simafranca, A. F.; Salamat, c.z.; Schwartz, B. J.; Tolbert, S. H. "Tuning the crystal structure of P3HT by Rub-Aligning Controls the Propensity for Chemical Doping". I came up with the idea of the paper, took and analyzed all the GIWAXS data. I also wrote the first manuscript. Quynh made all the samples, took the spectroscopy data and helped with the manuscript. Alex discussed the data interpretation with me, came up with the idea to explain GIWAXS data and helped with the manuscript. Charlene took parts of the GIWAXS data. Sarah and Ben gave research suggestions and edited the final manuscript. The PIs and/or project directors were: Benjamin Schwartz and Sarah Tolbert.

Chapter 5 is a version of Wu, Y.; Li, Y.L.; Salamat, c.z.; Winchell, K. J.; Schwartz, B. J.; Rubin, Y. F.; Tolbert, S. H. "Controlling Co-assemblies of Amphiphilic Polymers and Small Molecule Acceptors that Facilitate Excited-State Electron Transfer". I made all the samples, took and analyzed all the spectroscopy and solution SAXS data. I also wrote the first manuscript. Yolanda synthesized all the chemicals and helped with manuscript editing. Charlene helped make samples for solution SAXS and manuscript editing. KJ helped with polymer structure modeling. Sarah gave research suggestions and edited the final manuscript. The PIs and/or project directors were: Benjamin Schwartz, Yves Rubin and Sarah Tolbert.

VITA

University of California, Los Angeles 2017-2019

M.S. in Chemistry, major in Materials and Nanoscience

Jilin University 2013-2017

B.S. TangAoqing Honors Program

PUBLICATIONS

Wu, Y.; Li, Y.L.; Salamat, c.z.; Winchell, K. J.; Schwartz, B. J.; Rubin, Y. F.; Tolbert, S. H. Controlling Co-assemblies of Amphiphilic Polymers and Small Molecule Acceptors that Facilitate Excited-State Electron Transfer. *In-preparation* **(Chapter 5)**

Wu, Y.; Duong, Q.; Simafranca, A. F.; Salamat, c.z.; Schwartz, B. J.; Tolbert, S. H. Tuning the crystal structure of P3HT by Rub-Aligning Controls the Propensity for Chemical Doping. *In-preparation* **(Chapter 4)**

Wu, Y.; Salamat, c.z.; Ruiz, O.L.; Simafranca, A. F.; Wu, E. C.; Doud, E.; Lindemuth, J. R.; Phan, M. D.; Spokoyny, A. M.; Schwartz, B. J.; Tolbert, S. H. Bulky Charge-Shielding Dodecaborane-Based Dopants: An Effective Strategy Towards the Production of Mobile Charge Carriers in the Amorphous Regions of Semiconducting Polymers. *In-preparation* **(Chapter 3)**

Lin, Z.; Wan, Z.; Song, F.; Huang, B.; Jia, C.; Qian, Q.; Kang, J. S.; **Wu, Y.**; Yan, X.; Peng, L.; et al. High-Yield Exfoliation of 2D Semiconductor Monolayers and Reassembly of Organic/Inorganic Artificial Superlattices. *Chem* **2021**, 1–16.

Stanfield, D. A.; † **Wu, Y.**; † Tolbert, S. H.; Schwartz, B. J. Controlling the Formation of Charge Transfer Complexes in Chemically Doped Semiconducting Polymers. *Chem. Mater.* **2021**, *33* (7), 2343–2356. **(co-first author) (Chapter 2)**

CONFERENCES

American Chemical Society National Meeting, Talk, "Controlling Co-assemblies of Amphiphilic Polymers and Small Molecule Acceptors that Facilitate Excited-State Electron Transfer." Wu, Y.; Li, Y.L.; Salamat, c.z.; Winchell, K. J.; Schwartz, B. J.; Rubin, Y. F.; Tolbert, S. H., San Diego, CA, August 2019

Chapter 1. Introduction

1.1 Molecular Doping of Semiconducting Polymers

Semiconducting polymers have many applications in modern electronic techniques.[1–7] They have the advantage of being cheap, flexible and solution processable. The elemental composition and molecular structure of semiconducting polymers make them both low-cost and relatively easy to be manufactured in solution without using expensive techniques.[8–10] Recent progress in organic chemistry enables the synthesis of a wide range of semiconducting polymers for photovoltaic and organic light-emitting diode (OLED) applications.[11–15] Semiconducting polymers also have the advantage of being tunable in a variety of ways. When the backbone composition, conjugation length, bond angle of the semiconducting polymers are different, they have distinct structure and electronic properties.[16–18]The side chain structure, geometry, hydrophobicity and branching point on the polymer backbone also play an important role on polymer solubility and processed film microstructure.[19–21]

Semiconducting polymers intrinsically are not conductive due to the relative wide band-gap, carriers cannot be thermally excited to conduction band (Figure 1.1a). Thus doping, a redox process with another molecule is necessary to induce charge carriers. For inorganic semiconductors such as silicon, doping is a substitutional process. The Si atom in the lattice is substituted with another atom either has an extra electron (n-type impurity) or lacks an electron (p-type impurity). Thus, the extra electron or the left hole serves as the charge carrier in the conducting network.[22] Different from the inorganic semiconductors, semiconducting polymer doping is an interstitial charge transfer process. When electrons are removed from polymer valence band and transfer to acceptor molecule, it is an oxidation process (p-type doping) and when electrons transfer from the donor molecule to polymer conduction band, it is a reduction process

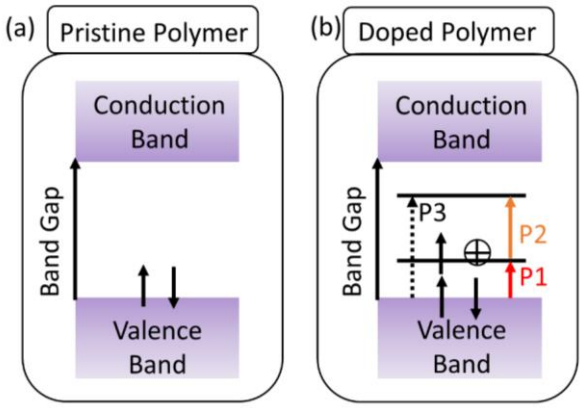

Figure 1.1: Band diagram of neutral (a) and doped (b) semiconducting polymer. New intraband states and electron transitions form in doped polymer.

(n-type doping). Many progresses have been made on n-type doped semiconducting polymer, however, the unstable doped phase and the need to find donor molecule with compatible band levels are potential drawbacks. This thesis focuses on p-type doping of semiconducting polymers.

P-type doping requires the dopant's lowest unoccupied molecular orbital (LUMO) is deeper than the polymer highest occupied molecular orbital (HOMO). The energy gap between these two levels is the driving force for the charge transfer process. Our previous work shows that dopant molecules with larger energetic offsets can dope the same polymer to larger extent and generate more mobile carriers.[23] Kiefer et, al, shows that when dopant molecule LUMO is deep enough, the dopant anion can further dope the host polymer and form a dianion molecule.[24] Recent work from Watanabe's group came up with the anion exchange doping by mixing ionic salts with the doped semiconducting polymers.[25,26] They found that the salt anion can switch out the dopant anion, resulting in much higher doping efficiency and conductivity.

A variety of p-type dopant molecules have been reported so far.[27–30] It has been shown that dopant molecular size, geometry, redox potential can influence their packing and charge transfer pathways with semiconducting polymers. When semiconducting polymers get doped, electrons

are removed from the polymer valence band, the left holes (also referred as polarons) serve as the charge carries in the polymer network. Two extra intragap states also form in the bandgap as shown in Figure 1.1b. New allowed electron transitions thus form: P1 corresponds to the transition from valence band to lower intraband state; P2 corresponds to the transition from lower intraband state to higher intraband state and P3 which is the transition from valence band to higher intraband state is usually forbidden. Spectroscopy is a direct and useful tool to identify and quantify the semiconducting polymer doping process by observing the electron transitions within the bandgap and we will heavily use this method to study polymer doping throughout this thesis.

1.2 Charge Transfer Pathways of Semiconducting Polymers

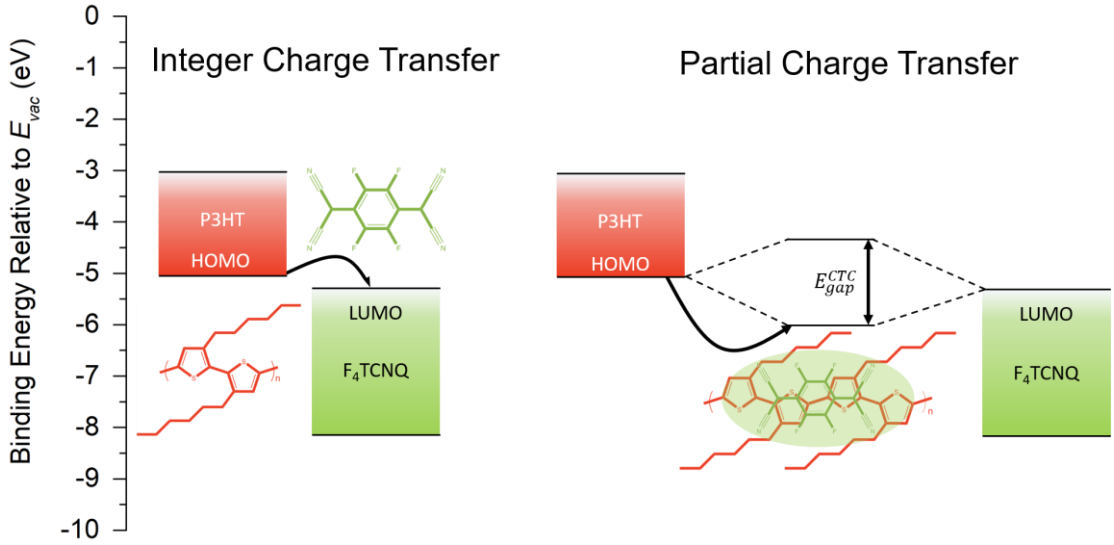

Figure 1.2: Schemes of P3HT integer and partial charge transfer.

As stated in the last section, when electrons transfer to the dopant molecules and form dopant anions, holes are left on the polymer backbone, this process is known as the integer charge transfer (Figure 1.2). The dopant molecule, however, can also form hybridized orbitals with the polymer when they π-stack with the polymer backbone and go through partial charge transfer (Figure 1.2).[21,31–33] Partial charge transfer results in the charge transfer complex (CTC) formation which is detrimental to conductivity. This is because not all the dopant molecules contribute to mobile

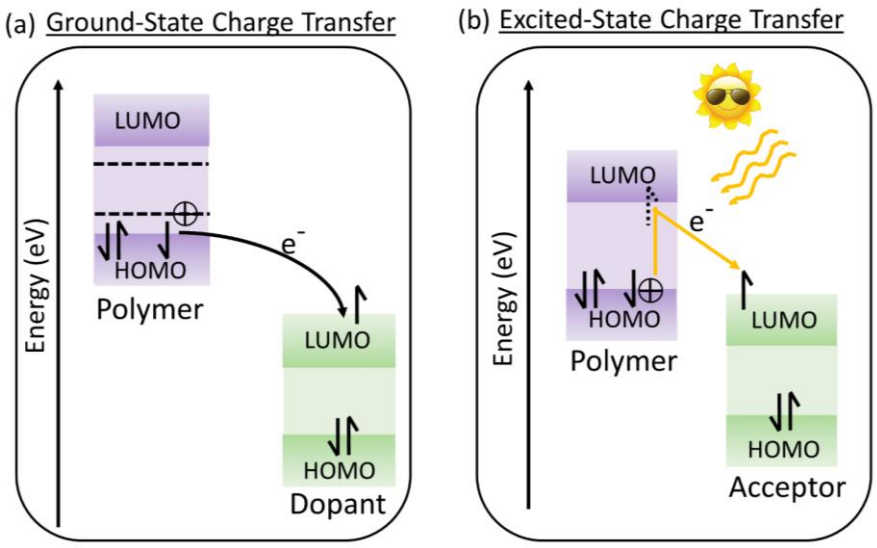

Figure 1.3: Schemes for p-type semiconducting polymer doping through ground-state charge transfer (a) and excited-state charge transfer (b).

carriers (polarons) formation. Since conductivity is proportional to the number of mobile carriers and carrier mobility, CTC formation generates fewer mobile carriers, thus results in lower conductivity.

The above discussion introduces the p-type doping of semiconducting polymer through a redox reaction with a dopant molecule (chemical doping). This process is also referred as ground-state charge transfer due to the direct electron transfer from polymer HOMO level to dopant molecule (Figure 1.3a). However, p-type doping can also be achieved through an excited-state charge transfer process as indicated in Figure 1.3b. Electrons are excited from polymer HOMO to LUMO level by visible light, and if there is an acceptor molecule nearby with appropriate LUMO level, electrons can then migrate to acceptor molecule instead of relaxing back to polymer HOMO.[34–36] This process requires that the polymer LUMO level is shallower than the acceptor LUMO level.[37] Polymers and the acceptor molecules also need to be close enough to enable this process.[38–40] This thesis will mainly focus on studying the ground-state charge transfer of p-type

doped semiconducting polymers in solid-state. The excited-state charge transfer will be discussed at last.

1.3 Structure Change of Semiconducting Polymer Doping

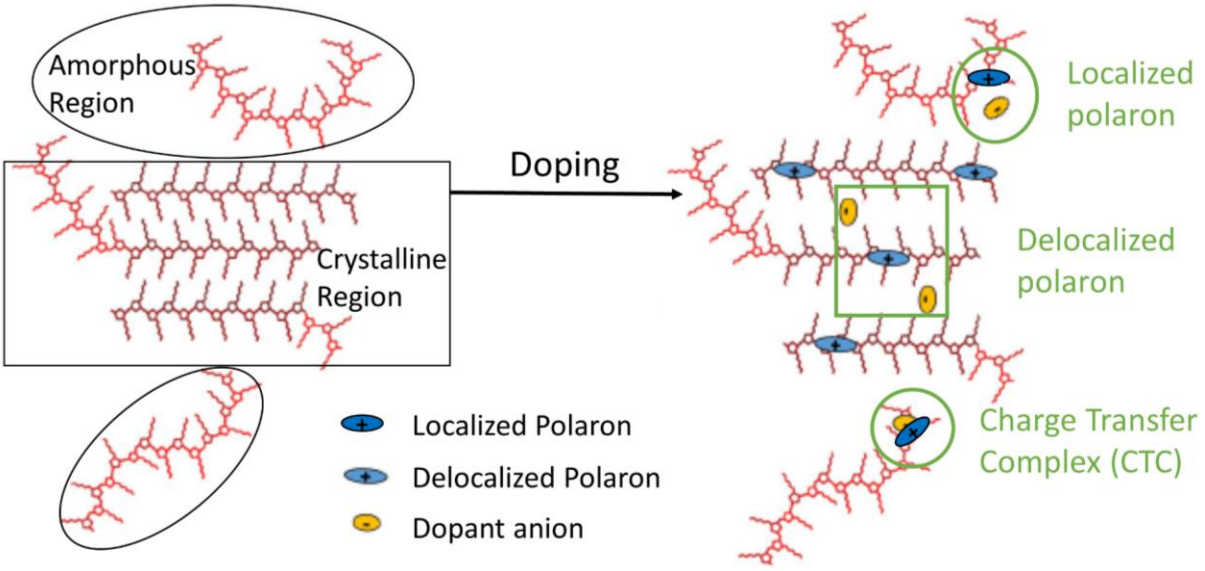

Figure 1.4: Schemes of different locations of dopant molecules in semicrystalline polymer (P3HT) matrix. Polaron mobility are higher when they are further away from the anion molecules. If dopant molecule π-stack with the polymer backbone, they form CTC. Figure source: Adapted from *Scholes, D. T. et, al. Adv. Funct. Mater.* ***2017****, 27 (44), 1–13.*

Semiconducting polymers are usually semicrytalline and consist both semi-ordered and amorphous region.[41] The location of the dopant molecule in the semiconducting polymer matrix determines the charge transfer pathway as well as the mobility of the polarons. Figure 1.4 shows the possible location of the dopant molecule in the polymer matrix. If the dopant molecule π-stacks with the polymer backbone, they form CTCs. Neelamraju et, al. found that CTCs tend to form in semiconducting polymer amorphous region compared to crystalline region.[32] Our previous study shows that CTCs form even in highly crystalline P3HT film.[42] If the dopant molecule goes through integer charge transfer with polymer amorphous region, this will result in the formation of polaron and dopant anion even though the generated polarons are usually localized due to the closeness

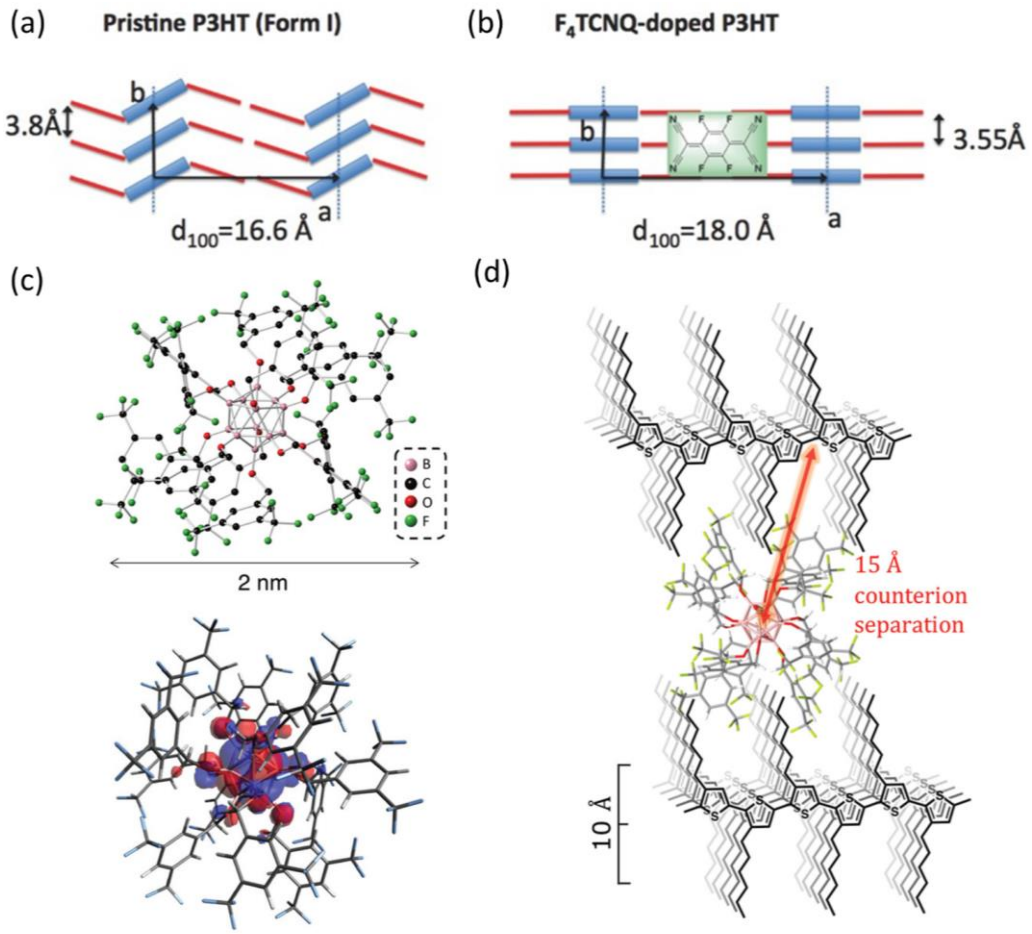

Figure 1.5: Cartoons shows the pristine P3HT with a monoclinic unit cell (a), F4TCNQ doped P3HT causes phase transition of the unit cell (b). (c) (Top) Ball-and-stick representation of the X-ray crystal structure of DDB-F72; (bottom) DDB-F72 anion SOMO calculated by TD-DFT shows the electron density locates at the cluster center. (d) DDB-F72 in the P3HT lamellar region. Figure a, b source: *Hamidi-Sakr, A. et, al. Adv. Funct. Mater.* ***2017****, 27 (25), 1–13.* Figure c source: *Aubry, T. J. et, al. Adv. Mater.* ***2019****, 31 (11), 1–8.* Figure d source: *Aubry, T. J. et, al. Adv. Funct. Mater.* **2020,** ***2001800***, 1–13.

with the dopant anion. More commonly, dopant molecules locate in polymer side chain regions to fill the lamellar void space instead of π-stacking with polymer backbone since the latter is thermodynamically unfavorable.[42] Such packing also keeps all the dopant molecules in a certain position and distance from the polarons on the backbone, resulting in high carrier mobility which is crucial to the film conductivity.[14,41,43] The distribution of polymer chains in amorphous region, however, are disordered as compared to the crystalline region. The distance between the dopant

anion and the polaron on the polymer backbone is of a wide range distribution, so the dopant anions have a higher chance sitting close to the polarons in the amorphous region, resulting in localized polarons.

When semiconducting polymers get doped by the dopant molecule, there is usually structure change caused by the infiltration of dopant molecule in the polymer lamellar side chain region. Brinkmann's group observed that the pristine P3HT unit cell is monoclinic (γ=86.5 deg) and the side chains are tilted (Figure 1.5a).[44] When it is doped by F4TCNQ molecule, the dopant molecule causes the phase transition of the P3HT unit cell and straightens the lamellar side chain (Figure 1.5b).[45] Moreover, recent study from Aubry et, al. shows that when dodecaborane-based (DDB) dopants ($C_{108}H_{36}B_{12}O_{60}F_{72}$, referred as DDB-F72) with a size around 2nm are used for doping, they also locate in the polymer lamellar side chain regions and largely expands the unit cell.[43,46] This further confirms that dopant molecules prefer to reside in crystalline lamellar side chain region.

1.4 Overview of Thesis

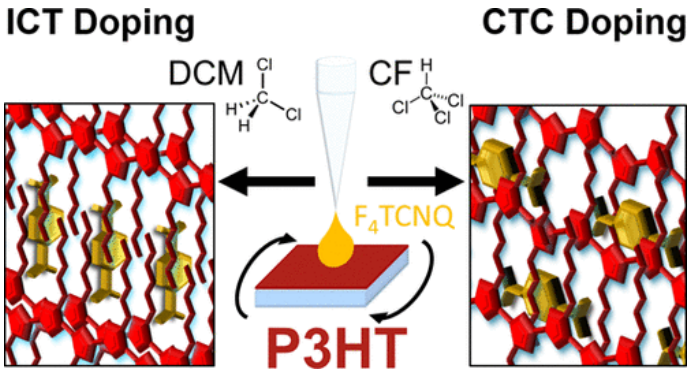

Figure 1.6: TOC figure for chapter 2. Figure source: *Stanfield, D. A. et, al. Chem. Mater.* ***2021****, 33 (7), 2343–2356.*

This thesis focuses on studying and controlling the structure of pristine and doped semiconducting polymers and provides perspectives on increasing semiconducting polymer film ordering in different regions.

Chapter 2 is about controlling the formation of charge transfer complexes in chemically doped semiconducting polymers (Figure 1.6). In this work, we use F4TCNQ doped P3HT to demonstrate how simply adjusting the dopant processing solvent can fundamentally alter the nature of doping in this well-studied system, leading to tunable production of CTCs. Using solvent blends of dichloromethane and chloroform, selected for their low and high solubility toward P3HT, respectively, we show that the relative amount of polymer-dopant CTCs can be readily controlled over an order of magnitude. Increasing the amount of chloroform in the dopant solvent blend favors the creation of CTCs, while increasing the dichloromethane content results in doping by the more standard ICT; the results allow us to explain why CTC formation is common in charge-transfer salts but generally less so in doped conjugated polymers. We also explore the role of the doping method and the crystallinity of P3HT films in controlling the relative amounts of ICT and CTC formation. We find that the use of evaporation doping and higher-crystallinity material discourages CTC formation, but that even in the most favorable case of evaporation doping with high polymer crystallinity, fractional charge transfer always occurs to some extent. Finally, we show that brief thermal annealing can convert CTCs to integer charge transfer species, indicating that ICT is the thermodynamically preferred doping mechanism in conjugated polymers, and that fractional charge transfer is the result of kinetic trapping. With this understanding, we offer guidelines for limiting the occurrence of charge transfer complexes during sequential doping of conjugated polymers, thus avoiding the deleterious effects of CTCs on charge transport.

As stated in the previous section, CTCs tend to form in the polymer film amorphous region. Amorphous region also has the disadvantages of forming localized polarons compared with crystalline region. Semicrystalline polymer film cannot avoid the formation of amorphous region even though the crystalline region dictates the film conductivity, thus it would be useful to convert polymer amorphous region to crystallites. Meanwhile, dopant molecules can be designed to suppress the CTC formation and overcome the localized polaron issues in the amorphous region.

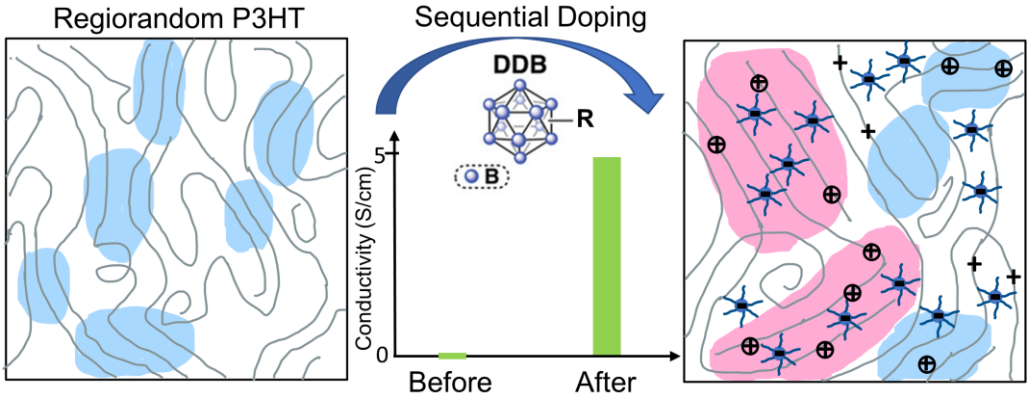

Figure 1.7: TOC figure for Chapter 3.

In chapter 3, we specifically chose regiorandom (RRa) P3HT as a platform to study how the high redox potential DDB dopants dope RRa P3HT (Figure 1.7). RRa P3HT forms disordered aggregates instead of crystallites, thus it provides insights on doping in polymer amorphous region. DDB dopants are of sphere shape with a size of ~ 2nm and their electron density is restricted in the center. This prevents the orbital overlapping of DDB dopants with polymer backbone which is necessary for CTC formation. The large dopant size can also shield the interaction between the polaron and the DDB dopant anion, resulting in high carrier mobility. Spectroscopy data confirms the successful doping of the RRa P3HT with a conductivity of ~ 5 S/cm. AC Hall measurement shows comparable carrier mobility as generated in the regioregular (RR) P3HT. The increased

short-range and long-range ordering of the doped RRa P3HT, together with the successful separation of mobile carrier from counterions result in the high conductivity of RRa P3HT.

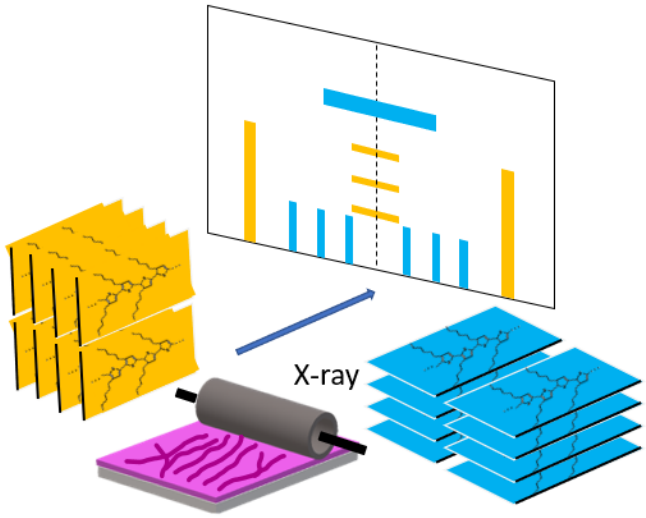

Figure 1.8: Rub-aligned P3HT consists of both edge-on and face-on polymorphs.

Semiconducting polymer amorphous region hinders the charge transport due to lacking of coherence and its disordering nature, even though they can tie the crystallites together.[47] Chapter 3 introduces how to increase the ordering and conductivity in the amorphous region. In the next chapter, we aim to increase the ordering of the crystalline region. Mobile charges can conduct in different directions in doped semiconducting polymers. The fastest conducting direction is along the polymer backbone, followed by the π-π stacking direction. Carrier mobility along the lamellar side chain is slower compared with the other two directions.[48] Pristine P3HT is usually in edge-on texture (i.e., side-chains perpendicular to the substrate) and the crystallite orientation are isotropic in plane. By aligning the polymer backbone in one direction, the long-range ordering can increase in both the polymer backbone and π-π stacking direction.

Chapter 4 studies how P3HT crystalline orientation influences the propensity for chemical doping. Pre-cast P3HT films are rub-aligned using a micro-fiber wheel. Spectroscopy and X-ray characterization confirm that the aligned polymer film is composed of both edge-on and face-on

(i.e., π-stacking perpendicular to the substrate) polymorphs with the backbone of both aligned with rub-aligning direction (Figure 1.8). These two polymorphs show different crystalline structures. Grazing-incidence wide-angle X-ray scattering (GIWAXS) shows these two polymorphs need to overcome different energetic costs when doped by 2,3,5,6-tetrafluoro-7,7,8,8-tetracyanoquinodimethane (F4TCNQ), with doping occurring first in face-on-oriented P3HT polymorph. Detailed structural analysis reveals that this preferential doping is driven by its structure similar to the final doped phase. This finding suggests that doping of semiconducting polymers can be encouraged by polymer orientations that minimize the structural differences between doped and undoped phases.

All the above chapters study controlling the polymer structure in solid-state, however, it has the disadvantages of forming kinetically trapped states when the films are processed. Besides, rub-aligning the polymer film is hard to scale up. A better method is to order the polymer in solution and reserve such ordering when casting the polymer film.

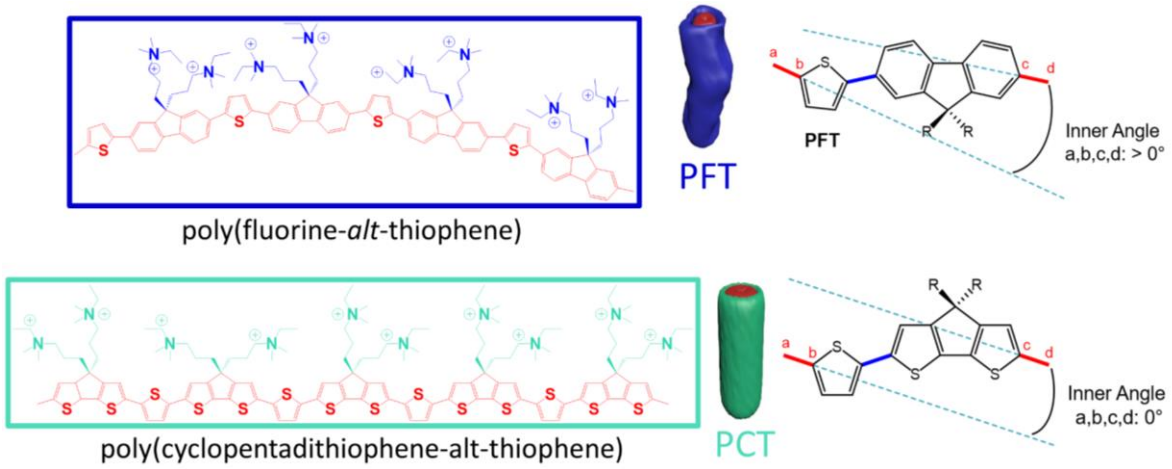

Figure 1.9: Molecular structure of PFT and PCT. PFT and PCT all form cylindrical micelles in water, PCT is straighter and more ordered compared with PFT.

Chapter 5 is based on the previous work in our group.[49,50] We designed and studied two amphiphilic semiconducting polymers poly(fluorine-alt-thiophene) (PFT) and

poly(cyclopentadithiophene-alt-thiophene) (PCT). These two polymers (Figure 1.9) are conjugated polyelectrolytes which consist of a conjugated backbone with charged alkyl side chains and are capable of self-assembling into cylindrical micelles in polar solvents such as water. In this work, we demonstrate how these amphiphilic polymers act as the scaffold for co-assemblies with electron acceptors. We probe the excited-state electron transfer of these co-assemblies by varying the acceptor size and solvation conditions necessary to form said co-assemblies. We find that tightly packed polymer micelles assemble more easily with flatter perylene diimide based acceptors than larger fullerene-based acceptors, as verified through a combination of photoluminescence (PL) spectroscopy and solution small angle X-ray scattering (SAXS). Initial geometric mismatch between tightly packed donor micelles and acceptors can be overcome by solvent annealing to drive additional acceptor incorporation. In contrast, looser and more disordered micelles form similar co-assembled structures, independent of acceptor shape. Our results demonstrate that we can achieve relatively precise control between electron donor and acceptor co-assemblies by varying the structural properties of component polymers and acceptors, which can provide guidelines for designing systems with controllable excited state electron transfers.

1.5 References

(1) Tiwari, S.; Singh, A. K.; Joshi, L.; Chakrabarti, P.; Takashima, W.; Kaneto, K.; Prakash, R. Poly-3-Hexylthiophene Based Organic Field-Effect Transistor: Detection of Low Concentration of Ammonia. *Sensors Actuators, B Chem.* **2012**, *171–172*, 962–968.

(2) Chung, D. Y.; Huang, J.; Bradley, D. D. C.; Campbell, A. J. High Performance, Flexible Polymer Light-Emitting Diodes (PLEDs) with Gravure Contact Printed Hole Injection and Light Emitting Layers. *Org. Electron.* **2010**, *11* (6), 1088–1095.

(3) Ragoussi, M. E.; Torres, T. Organic Photovoltaics. *Rev. Virtual Quim.* **2015**, *7* (1), 112–125.

(4) Zhang, S.; Ye, L.; Hou, J. Breaking the 10% Efficiency Barrier in Organic Photovoltaics: Morphology and Device Optimization of Well-Known PBDTTT Polymers. *Adv. Energy Mater.* **2016**, *6* (11), 1–20.

(5) Hou, L.; Zhang, X.; Cotella, G. F.; Carnicella, G.; Herder, M.; Schmidt, B. M.; Pätzel, M.; Hecht, S.; Cacialli, F.; Samorì, P. Optically Switchable Organic Light-Emitting Transistors. *Nat. Nanotechnol.* **2019**.

(6) Li, H.; Plunkett, E.; Cai, Z.; Qiu, B.; Wei, T.; Chen, H.; Thon, S. M.; Reich, D. H.; Chen, L.; Katz, H. E. Dopant-Dependent Increase in Seebeck Coefficient and Electrical Conductivity in Blended Polymers with Offset Carrier Energies. *Adv. Electron. Mater.* **2019**, *5* (11).

(7) Zapata-Arteaga, O.; Dörling, B.; Perevedentsev, A.; Martín, J.; Reparaz, J. S.; Campoy-Quiles, M. Closing the Stability-Performance Gap in Organic Thermoelectrics by Adjusting the Partial to Integer Charge Transfer Ratio. *Macromolecules* **2020**, *53* (2), 609–620.

(8) Lee, M.; Jeon, H.; Jang, M.; Yang, H. A Physicochemical Approach Toward Extending Conjugation and the Ordering of Solution-Processable Semiconducting Polymers. *ACS Appl. Mater. Interfaces* **2016**, *8* (7), 4819–4827.

(9) Allard, S.; Forster, M.; Souharce, B.; Thiem, H.; Scherf, U. Organic Semiconductors for Solution-Processable Field-Effect Transistors (OFETs). *Angew. Chemie - Int. Ed.* **2008**, *47* (22), 4070–4098.

(10) Knobloch, A.; Manuelli, A.; Bernds, A.; Clemens, W. Fully Printed Integrated Circuits from Solution Processable Polymers. *J. Appl. Phys.* **2004**, *96* (4), 2286–2291.

(11) Mooney, M.; Nyayachavadi, A.; Rondeau-Gagné, S. Eco-Friendly Semiconducting Polymers: From Greener Synthesis to Greener Processability. *J. Mater. Chem. C* **2020**, *8* (42), 14645–14664.

(12) Scharber, M. C.; Sariciftci, N. S. Low Band Gap Conjugated Semiconducting Polymers. *Adv. Mater. Technol.* **2021**, *6* (4).

(13) Liang, Y.; Wu, Y.; Feng, D.; Tsai, S. T.; Son, H. J.; Li, G.; Yu, L. Development of New Semiconducting Polymers for High Performance Solar Cells. *J. Am. Chem. Soc.* **2009**, *131* (1), 56–57.

(14) Scholes, D. T.; Yee, P. Y.; Lindemuth, J. R.; Kang, H.; Onorato, J.; Ghosh, R.; Luscombe, C. K.; Spano, F. C.; Tolbert, S. H.; Schwartz, B. J. The Effects of Crystallinity on Charge Transport and the Structure of Sequentially Processed F4TCNQ-Doped Conjugated Polymer Films. *Adv. Funct. Mater.* **2017**, *27* (44).

(15) Phan, S.; Luscombe, C. K. Recent Advances in the Green, Sustainable Synthesis of Semiconducting Polymers. *Trends Chem.* **2019**, *1* (7), 670–681.

(16) Zhao, Y.; Zhao, X.; Zang, Y.; Di, C. A.; Diao, Y.; Mei, J. Conjugation-Break Spacers in Semiconducting Polymers: Impact on Polymer Processability and Charge Transport Properties. *Macromolecules* **2015**, *48* (7), 2048–2053.

(17) Duong, D. T.; Wang, C.; Antono, E.; Toney, M. F.; Salleo, A. The Chemical and Structural Origin of Efficient P-Type Doping in P3HT. *Org. Electron. physics, Mater. Appl.* **2013**, *14* (5), 1330–1336.

(18) Perez, L. A.; Zalar, P.; Ying, L.; Schmidt, K.; Toney, M. F.; Nguyen, T. Q.; Bazan, G. C.; Kramer, E. J. Effect of Backbone Regioregularity on the Structure and Orientation of a Donor-Acceptor Semiconducting Copolymer. *Macromolecules* **2014**, *47* (4), 1403–1410.

(19) O'Hara, K.; Takacs, C. J.; Liu, S.; Cruciani, F.; Beaujuge, P.; Hawker, C. J.; Chabinyc, M. L. Effect of Alkyl Side Chains on Intercrystallite Ordering in Semiconducting Polymers. *Macromolecules* **2019**, *52* (7), 2853–2862.

(20) Yang, Y.; Liu, Z.; Zhang, G.; Zhang, X.; Zhang, D. The Effects of Side Chains on the Charge Mobilities and Functionalities of Semiconducting Conjugated Polymers beyond Solubilities. *Adv. Mater.* **2019**, *31* (46).

(21) Thomas, E. M.; Davidson, E. C.; Katsumata, R.; Segalman, R. A.; Chabinyc, M. L. Branched Side Chains Govern Counterion Position and Doping Mechanism in Conjugated Polythiophenes. *ACS Macro Lett.* **2018**, *7*, 1492–1497.

(22) Oba, F.; Tatsumi, K.; Adachi, H.; Tanaka, I. N- and p-Type Dopants for Cubic Silicon Nitride. *Appl. Phys. Lett.* **2001**, *78* (11), 1577–1579.

(23) Aubry, T. J.; Winchell, K. J.; Salamat, C. Z.; Basile, V. M.; Lin-, J. R.; Stauber, J. M.; Axtell, J. C.; Kubena, R. M.; Phan, M. D.; Bird, J.; et al. Tunable Dopants with Intrinsic Counterion Separation Reveal the Effects of Electron Affinity on Dopant Intercalation and Free Carrier Production in Sequentially Doped Conjugated Polymer Films. 1–41.

(24) Kroon, R.; Kemerink, M.; Hynynen, J.; Cano, A.; Nai, D.; McCulloch, I.; Liu, X.; Hofmann, A. I.; Marder, S. R.; Stegerer, D.; et al. Double Doping of Conjugated Polymers with Monomer Molecular Dopants. *Nat. Mater.* **2019**, *18* (2), 149–155.

(25) Yamashita, Y.; Tsurumi, J.; Ohno, M.; Fujimoto, R.; Kumagai, S.; Kurosawa, T.; Okamoto, T.; Takeya, J.; Watanabe, S. Efficient Molecular Doping of Polymeric Semiconductors Driven by Anion Exchange. *Nature* **2019**, *572* (7771), 634–638.

(26) Kohno, S.; Yamashita, Y.; Kasuya, N.; Mikie, T.; Osaka, I.; Takimiya, K.; Takeya, J.; Watanabe, S. Controlled Steric Selectivity in Molecular Doping towards Closest-Packed Supramolecular Conductors. *Commun. Mater.* **2020**, *1* (1), 1–8.

(27) Wegner, B.; Lungwitz, D.; Mansour, A. E.; Tait, C. E.; Tanaka, N.; Zhai, T.; Duhm, S.; Forster, M.; Behrends, J.; Shoji, Y.; et al. An Organic Borate Salt with Superior P-

Doping Capability for Organic Semiconductors. *Adv. Sci.* **2020**, 1–11.

(28) Karpov, Y.; Kiriy, N.; Formanek, P.; Hoffmann, C.; Beryozkina, T.; Hambsch, M.; Al-Hussein, M.; Mannsfeld, S. C. B.; Büchner, B.; Debnath, B.; et al. Sequentially Processed P3HT/CN6-CP•−NBu4+ Films: Interfacial or Bulk Doping? *Adv. Electron. Mater.* **2020**, *6* (5).

(29) Saska, J.; Gonel, G.; Bedolla-Valdez, Z. I.; Aronow, S. D.; Shevchenko, N. E.; Dudnik, A. S.; Moulé, A. J.; Mascal, M. A Freely Soluble, High Electron Affinity Molecular Dopant for Solution Processing of Organic Semiconductors. *Chem. Mater.* **2019**, *31* (5), 1500–1506.

(30) Scholes, D. T.; Hawks, S. A.; Yee, P. Y.; Wu, H.; Lindemuth, J. R.; Tolbert, S. H.; Schwartz, B. J. Overcoming Film Quality Issues for Conjugated Polymers Doped with F4TCNQ by Solution Sequential Processing: Hall Effect, Structural, and Optical Measurements. *J. Phys. Chem. Lett.* **2015**, *6* (23), 4786–4793.

(31) Jacobs, I. E.; Cendra, C.; Harrelson, T. F.; Bedolla Valdez, Z. I.; Faller, R.; Salleo, A.; Moulé, A. J. Polymorphism Controls the Degree of Charge Transfer in a Molecularly Doped Semiconducting Polymer. *Mater. Horizons* **2018**, *5* (4), 655–660.

(32) Neelamraju, B.; Watts, K. E.; Pemberton, J. E.; Ratcliff, E. L. Correlation of Coexistent Charge Transfer States in F 4 TCNQ-Doped P3HT with Microstructure. *J. Phys. Chem. Lett.* **2018**, *9* (23), 6871–6877.

(33) Watts, K. E.; Neelamraju, B.; Ratcliff, E. L.; Pemberton, J. E. Stability of Charge Transfer States in F4TCNQ-Doped P3HT. *Chem. Mater.* **2019**, acs.chemmater.9b01549.

(34) Mohapatra, P. K.; Singh, N. R. Teaching the Z-Scheme of Electron Transport in Photosynthesis: A Perspective. *Photosynth. Res.* **2015**, *123* (1), 105–114.

(35) Morishima, Y.; Tominaga, Y.; Kamachi, M.; Okada, T.; Hirata, Y.; Mataga, N. Photoinduced Charge Separation by Chromophores Encapsulated in the Hydrophobic Compartment of Amphiphllic Polyelectrolytes with Various Aliphatic Hydrocarbons. *J. Phys. Chem.* **1991**, *95* (15), 6027–6034.

(36) Melkozernov, A. N.; Barber, J.; Blankenship, R. E. Light Harvesting in Photosystem I Supercomplexes. *Biochemistry* **2006**, *45* (2), 331–345.

(37) Kavarnos, G. J.; Turro, N. J. Photosensitization by Reversible Electron Transfer: Theories, Experimental Evidence, and Examples. *Chem. Rev.* **1986**, *86* (2), 401–449.

(38) Imahori, H.; Tamaki, K.; Araki, Y.; Sekiguchi, Y.; Ito, O.; Sakata, Y.; Fukuzumi, S. Stepwise Charge Separation and Charge Recombination in Ferrocene-Meso,Meso-Linked Porphyrin Dimer-Fullerene Triad. *J. Am. Chem. Soc.* **2002**, *124* (18), 5165–5174.

(39) Kashiwagi, Y.; Ohkubo, K.; McDonald, J. A.; Blake, I. M.; Crossley, M. J.; Araki, Y.; Ito, O.; Imahori, H.; Fukuzumi, S. Long-Lived Charge-Separated State Produced by Photoinduced Electron Transfer in a Zinc Imidazoporphyrin-C60 Dyad. *Org. Lett.* **2003**, *5* (15), 2719–2721.

(40) Imahori, H.; Guldi, D. M.; Tamaki, K.; Yoshida, Y.; Luo, C.; Sakata, Y.; Fukuzumi, S.

Charge Separation in a Novel Artificial Photosynthetic Reaction Center Lives 380 Ms. *J. Am. Chem. Soc.* **2001**, *123* (27), 6617–6628.

(41) Noriega, R.; Rivnay, J.; Vandewal, K.; Koch, F. P. V; Stingelin, N.; Smith, P.; Toney, M. F.; Salleo, A. A General Relationship between Disorder, Aggregation and Charge Transport in Conjugated Polymers. *Nat. Mater.* **2013**, *12* (11), 1038–1044.

(42) Stanfield, D. A.; Wu, Y.; Tolbert, S. H.; Schwartz, B. J. Controlling the Formation of Charge Transfer Complexes in Chemically Doped Semiconducting Polymers. *Chem. Mater.* **2021**, *33* (7), 2343–2356.

(43) Aubry, T. J.; Winchell, K. J.; Salamat, C. Z.; Basile, V. M.; Lindemuth, J. R.; Stauber, J. M.; Axtell, J. C.; Kubena, R. M.; Phan, M. D.; Bird, M. J.; et al. Tunable Dopants with Intrinsic Counterion Separation Reveal the Effects of Electron Affinity on Dopant Intercalation and Free Carrier Production in Sequentially Doped Conjugated Polymer Films. *Adv. Funct. Mater.* **2020**, *2001800*, 1–13.

(44) Kayunkid, N.; Uttiya, S.; Brinkmann, M. Structural Model of Regioregular Poly(3-Hexylthiophene) Obtained by Electron Diffraction Analysis. *Macromolecules* **2010**, *43* (11), 4961–4967.

(45) Hamidi-Sakr, A.; Biniek, L.; Bantignies, J. L.; Maurin, D.; Herrmann, L.; Leclerc, N.; Lévêque, P.; Vijayakumar, V.; Zimmermann, N.; Brinkmann, M. A Versatile Method to Fabricate Highly In-Plane Aligned Conducting Polymer Films with Anisotropic Charge Transport and Thermoelectric Properties: The Key Role of Alkyl Side Chain Layers on the Doping Mechanism. *Adv. Funct. Mater.* **2017**, *27* (25), 1–13.

(46) Aubry, T. J.; Axtell, J. C.; Basile, V. M.; Winchell, K. J.; Lindemuth, J. R.; Porter, T. M.; Liu, J. Y.; Alexandrova, A. N.; Kubiak, C. P.; Tolbert, S. H.; et al. Dodecaborane-Based Dopants Designed to Shield Anion Electrostatics Lead to Increased Carrier Mobility in a Doped Conjugated Polymer. *Adv. Mater.* **2019**, *31* (11).

(47) Salleo, A.; Kline, R. J.; DeLongchamp, D. M.; Chabinyc, M. L. Microstructural Characterization and Charge Transport in Thin Films of Conjugated Polymers. *Adv. Mater.* **2010**, *22* (34), 3812–3838.

(48) Tremel, K.; Ludwigs, S. *P3HT Revisited – From Molecular Scale to Solar Cell Devices*; 2014; Vol. 265.

(49) Huber, R. C.; Ferreira, A. S.; Thompson, R.; Kilbride, D.; Knutson, N. S.; Devi, L. S.; Toso, D. B.; Challa, J. R.; Zhou, Z. H.; Rubin, Y.; et al. Long-Lived Photoinduced Polaron Formation in Conjugated Polyelectrolyte-Fullerene Assemblies. *Science (80-.).* **2015**, *348* (6241), 1340–1343.

(50) Clark, A. P. Z.; Shi, C.; Ng, B. C.; Wilking, J. N.; Ayzner, A. L.; Stieg, A. Z.; Schwartz, B. J.; Mason, T. G.; Rubin, Y.; Tolbert, S. H. Self-Assembling Semiconducting Polymers - Rods and Gels from Electronic Materials. *ACS Nano* **2013**, *7* (2), 962–977.

Chapter 2. Controlling the Formation of Charge Transfer Complexes in Chemically Doped Semiconducting Polymers

2.1 Introduction

Conjugated organic semiconductors offer great promise as the active materials for applications in flexible electronics, including light-emitting diodes, photovoltaics, and thermoelectric devices.[1–5] For many of these applications, it is necessary to introduce equilibrium charge carriers into the π-systems of these materials. This is often achieved by chemical doping, which involves the introduction of a strong oxidizing (or reducing) agent to remove (or add) electrons from (to) an organic semiconductor. In organic light-emitting diodes and photovoltaic cells, for example, chemical doping of an interfacial conjugated polymer layer can lower barriers and enhance charge injection. Additionally, for organic thermoelectric materials, doping dramatically affects both the Seebeck coefficient and the electrical conductivity, two of the factors that comprise the thermoelectric figure of merit.[3,6,7] Most organic semiconductors are p-type materials, so they are best doped by using strong oxidizing agents to remove electrons from the π-conjugated backbone.

The idea of chemical doping of organic semiconductors has its roots in the study of charge-transfer salts, which dates back to the 1970s.[8–10] The classic example of a charge-transfer salt is a mixture of tetrathiafulvalene (TTF) and 7,7,8,8- tetracyanoquinodimethane (TCNQ).[11] In such charge-transfer salts, acceptor molecules like TCNQ act as oxidizing agents, removing part of an electron from conjugated donors like TTF. The co-crystals are characterized by charge-transfer complexes (CTCs), which result in delocalized electronic states with a band structure that has the valence band predominantly derived from the donor HOMO and the conduction band from the acceptor LUMO.[12] Such charge-transfer salts can exhibit a metallic behavior if they form in the

right co-crystal structure and have sufficient driving force for charge separation (i.e., the energetic offset between the oxidation potential of the donor and the reduction potential of the acceptor is sufficiently large), both of which determine the fraction of an electron that is locally transferred from the donor to the acceptor.[10,13]

Unlike the donors in small-molecule charge-transfer salts, when solution-processable conjugated polymers are mixed with small-molecule oxidizing agents, the result is nearly always integer charge transfer (ICT);[14–24] the types of CTCs that are readily observed with small conjugated molecules in charge transfer salts have been less commonly seen.[25–30] In fact, one needs to go to great lengths to produce CTCs from chemically doped conjugated polymers. For example, CTCs can be observed when the polymer and dopant are spun from a hot solution onto a pre-heated substrate[26] or when branched side chains are employed to force the dopant counterion into specific locations in the polymer crystal lattice.[27] CTCs are usually not desirable for most doped conjugated polymer applications since they produce a smaller fraction of doping induced carriers than ICTs; thus, their relative rarity is generally advantageous.[31] However, it is still not clear why ICT is favored when chemically doping conjugated polymers. This leads to the central question explored in this work: why do mixtures of acceptors with small-molecule donors, including the oligomers of many common conjugated polymers, usually produce CTCs,[32] while mixtures of conjugated polymers with the same acceptors usually lead to ICT?

To address this question, in this paper we re-examine the well-studied conjugated polymer, poly(3-hexylthiophene-2,5-diyl) (P3HT) doped with the strong electron acceptor 2,3,5,6-tetrafluoro-7,7,8,8-tetracyanoquinodimethane (F4TCNQ) to gain new insights into the process of how conjugated polymers produce CTCs or undergo ICT upon chemical doping. We track the degree of charge transfer using a combination of UV−Visible spectroscopy, to monitor the

electronic transitions produced following doping, and FTIR spectroscopy, to determine the amount of charge transferred from the polymer to the F4TNCQ acceptor; we also monitor the structure of the doped films using 2D grazing-incidence wide-angle X-ray scattering (GIWAXS). We find that we can control the relative amounts of CTCs and ICT that take place upon F4TCNQ doping of P3HT by using a tunable blend of solvents (dichloromethane, DCM, and chloroform, CF) to infiltrate the dopant into the polymer layer via sequential processing. Using pure DCM to deposit F4TCNQ onto pre-cast P3HT films, we see relatively little CTC formation, whereas the use of pure CF increases CTC formation by over an order of magnitude. Sequentially depositing the dopant from blends of DCM and CF allows the amount of CTC formed to be tuned anywhere in between.

With this control in hand, we now have a toolkit for studying CTC formation without resorting to extreme processing conditions or synthetically modified conjugated polymers. This allows us to explore how different aspects of the materials and processing conditions affect the tendency to undergo CTC formation. In particular, we compare the use of evaporation doping (i.e., subliming the F4TCNQ dopant onto pre-cast conjugated polymer film)[33] to the typical solution-based sequential doping method to investigate the role of dopant transport on CTC formation. We then study the role of the pre-formed polymer film crystallinity to elucidate the preference of crystalline and amorphous polymer domains to participate in CTC formation.

P3HT films are always composed of some combination of crystalline and amorphous regions, and we find that the more crystalline a P3HT film is prior to sequential doping, the smaller the fraction of CTC states generated. However, we also find that CTC doping cannot be entirely eliminated, even for the most crystalline P3HT films, showing that there is still room to improve sequential doping methods. We also show that doping via vapor transport produces a smaller

fraction of CTC states relative to solution sequential doping, providing significant clues to the role of kinetics in forming CTC states.

The structure of most conjugated polymers consists of semicrystalline regions characterized by a π-stacking spacing between the polymer backbones and a lamellar spacing along the polymer side chains. We and other research groups have argued in previous works that dopant molecules prefer to reside in the polymer lamellae as the barrier to dopant insertion into the easily disordered side chains is lower than breaking up the polymer π-stacks to insert the dopant.[7,17,21,22,24] Placing dopants in the lamellae, where they reside far from the polymer backbone, leads to ICT, as there is insufficient wave function overlap between the donor and acceptor for CTC formation to take place. Instead, CTC states only occur when the F4TCNQ dopant is able to π-stack with the conjugated polymer.[26–30] These results lead us to an improved picture of the kinetic competition between the two doping mechanisms, where the choice of processing conditions can alter the kinetic barrier for placing dopants in the polymer π-stacks. All of the results explain how solvent blends and polymer crystallinity can control the preference for ICT vs CTC formation in doped conjugated polymers, and why CTC is the preferred doping mechanism in small-molecule charge transfer salts.

Finally, we show that ICT is not only kinetically preferred but is also thermodynamically favored for the F4TCNQ/P3HT combination of dopant and conjugated polymer. By exposing doped films to brief thermal annealing treatments, we find that the fraction of CTCs produced upon doping can be converted to ICT, further indicating that CTCs are kinetically trapped in doped conjugated polymer films. Overall, our work shows the steps that can be taken to minimize CTC formation for electronic applications (or to enhance CTC formation for study), including

increasing the polymer crystallinity and using dopants that physically cannot π-stack or have wave function mixing with the conjugated polymer backbone.[21,23]

2.2 Experimental and Methods

Materials.

Electronic-grade P3HT (4002-EE; 91−94%, Mw = 46−57 kg/mol, PDI = 2.3) was purchased from Rieke Metals, and sublimation-grade F4TCNQ (purity, >98%) was purchased from TCI America. The synthesis and preparation of the P3HT denoted "100% RR" has been described by us in prior work.[21] All materials and solvents were used as received without any further purification.

Fabrication and Doping of Polymer Films.

Glass and silicon substrates were first degreased by sequentially sonicating for 10 min in a detergent solution, deionized water, acetone, and finally isopropyl alcohol. Substrates were then dried and stored in a nitrogen glove box where all subsequent solution processing steps takes place. For experiments using doping solvent blends, thin films of P3HT were prepared by spin-coating a polymer solution (20 mg mL^{-1}) out of odichlorobenzene (ODCB) at 1000 rpm for 20 s. Directly after spin-coating, the still wet films were moved to an open Petri dish until they finished drying. All dopant solutions of F4TCNQ (1 mg mL^{-1}) for the set of solvent blends containing chloroform (CF) and dichloromethane (DCM) were generated by adding the desired volume of each solvent to a vial with F4TCNQ powder. Sequential doping was carried out by pipetting dopant solution solvent blends (100 μL) onto pristine P3HT films and spin-coating at 4000 rpm for 10 s to remove the excess material. Additional experimental details can be found in the Supporting Information.

For the experiments comparing the vapor and solution sequential doping methods, 110 and 400 nm-thick pristine P3HT films were prepared by spin-coating from 20 and 50 mg mL^{-1} ODCB solutions respectively at 1000 rpm for 60 s followed by 3000 rpm for 5 s. Sequential solution doping with F4TCNQ was carried out by pipetting 100 μL of dopant solution out of DCM (1 mg mL^{-1}) onto pristine P3HT films and spin-coating at 4000 rpm for 10 s to remove the excess material. Sequential vapor doping with F4TCNQ was carried out using an Angstrom Engineering Nexdep Physical Vapor Deposition System. The F4TCNQ powder was placed in an alumina crucible and evaporated at 0.5 Å s^{-1} with a base pressure of $< 1 \times 10^{-6}$ Torr. Pristine P3HT films were placed on a rotating stage that was actively cooled to 15 °C during deposition. Doping levels for the vapor process were optimized to produce the highest conductivity and to show comparable doping levels to the solution-processed samples. A more detailed discussion can be found in our previous work[33] and its supporting information.

For our work comparing doped P3HT films with tunable crystallinity, we used solvent evaporation kinetics to control the rate of P3HT film formation, where higher-boiling point solvents yield higher-crystallinity polymer films. To obtain P3HT films with relatively low crystallinity, P3HT solutions (10 mg mL^{-1}) were spin-coated from chloroform (CF) (b.p. = 61.2 °C) at 1000 rpm for 60 s. For films of intermediate crystallinity, P3HT solutions (20 mg mL^{-1}) were spin-coated from o-dichlorobenzene (ODCB) (b.p. = 180 °C) at 1160 rpm for 20 s. These still wet films were then placed in a covered Petri dish to further extend the drying period. Finally, for films with the highest degree of crystallinity, an in-house batch of P3HT with a regioregularity of essentially unity was employed. The same spin-coating procedure was used for this material as for the commercial material cast from ODCB with the exception that solutions were spin-coated out

hot at 60 °C to prevent aggregation. Additional details on film preparation, synthesis, and characterization can be found in our earlier work[21] and its supporting information.

GIWAXS Measurements of Doped Polymer Films.

2D GIWAXS data were collected at the Stanford Synchrotron Radiation Lightsource using beamline 11-3. The beam wavelength was 0.9742 Å, and the incidence angle was 0.12°. The sample chamber was flowed with helium to reduce noise, and the sample holder was 250 mm away from the detector. All the samples were irradiated for 90 s. To reduce the 2D diffractograms, we used the WAXStools in Igor Pro. The diffractograms were radially integrated to reduce to 1D diffraction curves (0−10° for out-of-plane, 80−90° for in-plane, and 0−90° for full). All the samples at a given doping condition were made and measured in triplicate to ensure the reproducibility and absolute scattering intensity. All diffractograms were thickness-normalized (after background subtraction) to the polymer film thickness prior to doping with F4TCNQ since only the polymer contributes to the diffraction intensity. Additional details can be found in the Supporting Information.

2.3 Results and Discussion

One of the most common ways to produce chemically doped polymer films is by solution sequential processing, where the dopant is infiltrated into a pre-cast conjugated polymer film using a semi-orthogonal solvent that swells but does not dissolve the underlying morphology.[17,21] Sequential doping is generally preferred because simply mixing the polymer and dopant together results in solution-phase charge transfer, creating a salt with unfavorable solubility in the non-polar organic solvents typically used to dissolve conjugated polymers. The resulting blend solutions are usually highly aggregated, leading to poor quality when cast into films.[17] Sequential

processing avoids this difficulty because the doped films largely have the same morphology as the original pre-cast films, providing the added advantage that the pre-cast polymer films can be created with different degrees of crystallinity[17,21] or rubbed to produce alignment of the polymer chains.[7,22,34] Sequential doping can also involve thermally evaporating the dopant onto a pre-cast polymer film,[20,35–39] which allows for effective infiltration of the dopant, even into polymer films that are hundreds of nanometers thick.[33]

Optical Transitions of P3HT:F4TNCQ Charge-Transfer Complexes.

When using solution sequential processing to dope a conjugated polymer, the solvent selected to introduce the dopant is usually chosen to have poor solubility for the underlying polymer; however, in principle, any solvent with a reasonably high solubility for the dopant can be used. For the P3HT/F4TCNQ system, we have shown that DCM is a particularly good solvent for solution sequential processing due to its reasonably high solubility toward F4TCNQ and relatively low solubility (0.818 mg mL^{-1}) toward P3HT.[17,21,33,40,41]

Based on this idea, it would seem that a solvent like CF, which has one of the highest known solubilities toward P3HT (38 mg mL^{-1}),[40] would be a poor choice for doping via solution sequential processing. This is because, at first glance, CF would be expected to dissolve the underlying polymer and thus remove the entire P3HT film from the substrate during the doping process. What we will show below, however, is that, when sequentially doping P3HT, the high dissolving power of CF does put some of the underlying P3HT film into solution while the F4TCNQ is being introduced, effectively removing any kinetic barriers to placing the dopant in the polymer π-stacks. At the same time, the rapid decrease in polymer solubility that occurs upon doping still allows most of the polymer material to remain intact on the substrate through a dynamic dissolution and reprecipitation process.

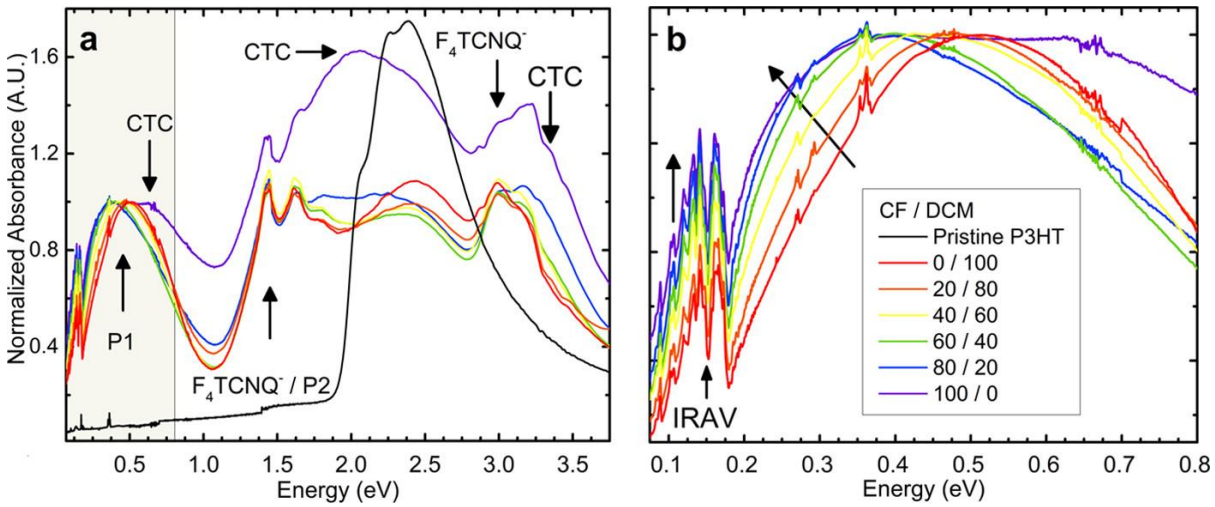

Figure 2.1: (a) UV–vis–NIR absorption spectrum of 1 mg mL^{-1} F4TCNQ sequentially doped P3HT films with the dopant deposited from solvent blends with different CF/DCM ratios, normalized to the peak absorption for the main P1 band near 0.4 eV. The electronic transitions from the CTC phase are labeled, along with the standard absorption features that appear with ICT. For comparison, the black curve shows the absorption of a P3HT film prior to doping, scaled to the correct relative absorption intensity of the film doped using 100% DCM (red curve). (b) The NIR P1 polaron absorption on an expanded energy scale of P3HT films sequentially doped with F4TCNQ from solvent blends with the indicated CF/DCM ratio by volume; this data corresponds to the section shaded in gray in panel (a). The black arrows highlight the increased intensity of the IRAV band and the monotonic redshift of the main P1 peak absorption with increasing CF content of the dopant casting solvent, indicative of increased polaron delocalization. The absorbance for pristine P3HT is essentially zero in this part of the spectrum and has thus been omitted for clarity.

Our first sign that using CF to sequentially dope P3HT with F4TCNQ produces a different electronic species comes from UV–Vis–NIR spectroscopy. Figure 2.1 shows the results when DCM, CF, and various blends of the two solvents (which are miscible) are used to expose pre-cast films of P3HT to 1 mg mL^{-1} solutions of F4TCNQ. The full spectra are plotted in Figure 2.1a, with the IR region focusing on the so-called P1 band (lowest-energy electronic transition) of the P3HT polaron shown on an expanded scale in Figure 2.1b. The spectra in both panels are normalized to the height of the absorption maximum near 0.4 eV, and further experimental details can be found in the Supporting Information.

The red curves in Figure 2.1 show the results when pure DCM is used as a dopant processing solvent. As is well known, doping P3HT this way leads to a reduced intensity of the neutral P3HT exciton absorption near 2.3 eV (black curve) as electrons are removed from the polymer valence band. Doping also leads to the appearance of a new band with two sharp vibronic features near 1.5 eV, which are representative of the F4TCNQ anion produced by ICT, along with the so-called P2 absorption band of the oxidized polymer that appears in the same energetic location. Finally, doping and ICT lead to a new absorption with peaks at 0.16 and ~0.4 eV, corresponding to the infrared active vibrations (IRAV) band and the P1 band of the hole (or polaron) on the polymer, respectively. The relative intensities of the P2/F4TCNQ$^-$ peak, the P1 band, and the remaining neutral P3HT absorption are all comparable in magnitude. In a previous work, we found that, with sequential doping, there is a maximal amount of F4TCNQ that can be intercalated into a pre-existing polymer film, no matter how high the doping solution concentration. The spectral signature for reaching this "saturation doping" is seen when the P1, P2/ F4TCNQ$^-$, and neutral P3HT bands are all comparable in absorbance, as is the case for these samples.[33]

With the exception of the film doped using pure CF, the other colored curves in Figure 2.1 show that using blends of DCM and CF to dope the P3HT film with F4TCNQ leads to the generally observed ICT doping behavior. However, for the solvent blend composed of 80% CF and 20% DCM (blue curves), there is a noticeable increase in absorption near 0.7, 2.0, and 3.3 eV, which further increase when casting F4TCNQ from pure CF (purple curves). The three new features all match well with what has been observed previously for CTC formation by Jacobs et al. for this system when hot solution mixtures of P3HT and F4TCNQ and hot substrates and pipette tips were used to create doped films.[26] These workers were able to isolate a structurally novel polymorph associated with these electronic features,[26] which we show below is also present in our films doped

sequentially from CF. Thus, Figure 2.1 shows that changing the solvent blend used for doping allows for control over the relative amount of CTC formation.

The results in Figure 2.1 can further be compared to work from Thomas et al., who showed that F4TCNQ doping can produce CTC states in a polythiophene derivative whose conjugated backbone is identical to that of P3HT, but with branched ethyl-hexyl side chains.[27] The bulkier side chains prevent F4TCNQ molecules from residing in their typically preferred location in the lamellar regions of the P3HT crystallites, leading to an absorption spectrum that resembles that seen with hot solvent casting by Jacobs et al.[26] and that of the purple curves in Figure 2.1. Thus, the UV−Vis−NIR spectrum in Figure 2.1a strongly suggests that the elevated solubilizing power of CF has a similar effect to high temperature-prolonged solvation of both species, allowing them to assemble into a polymorph with π-stacked charge transfer interactions that are separate from the typical ICT geometries seen for doped conjugated polymers. In addition, the relative intensity of the CTC absorption features to the P1 polaron peak seen for the pure CF processing condition further indicates that a substantial fraction of the F4TCNQ molecules in the film are no longer undergoing ICT and are instead doping via CTC formation. It is tempting to attempt to use the measured spectra to quantitatively extract information about the overall doping level and/or the ratio of ICT to CTC carriers for each set of processing conditions. However, because these films are doped via sequential deposition, we do not quantitatively know the overall doping level. We have established previously[17] that there is overlapping peak intensity of the F4TCNQ anion with other absorbing species, and unfortunately, we do not know the cross section for any of the absorbing species in doped P3HT films. This makes it problematic to use absorption spectroscopy

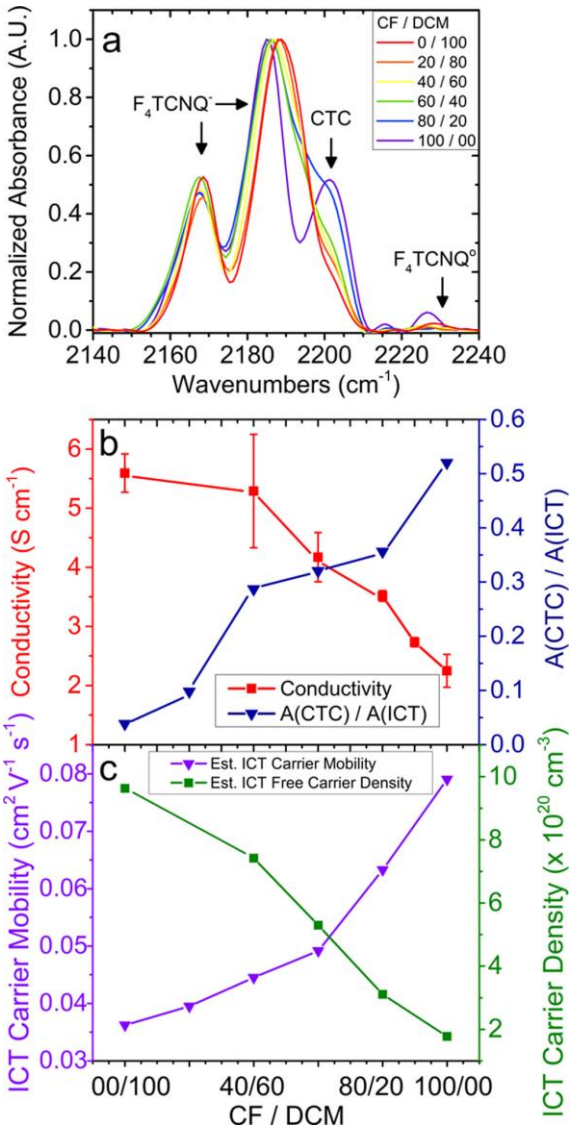

Figure 2.2: (a) Infrared absorbance of the C≡N stretching modes of F_4TCNQ-doped P3HT films as the dopant is introduced sequentially from solvent blends containing various CF/DCM ratios. The CTC peak at 2201 cm^{-1} shows a monotonic increase in relative amplitude as the fraction of CF is increased for the doping solvent. (b) Electrical conductivity (red squares) plotted against the fraction of CF in the doping solvent blend. A monotonic decrease in conductivity is observed as an increasing proportion of CF is used in the doping solvent despite the fact that the carriers produced by ICT are becoming more mobile. The ratio of the integrated infrared peak area for the CTC peak at 2201 cm^{-1} to that of the integrated peak area of the central ICT infrared band located near 2185 cm^{-1} (blue triangles), both taken from the data in panel (a). (c) Estimated ICT carrier mobility (purple triangles), calculated as described in the Supporting Information and ref 24 using the energy of the P1 polaron band peak absorbance. The estimated ICT carrier density (green squares) was calculated from the estimated mobility and the experimentally measured electrical conductivity. Clearly, the presence of CTC states is strongly anticorrelated with the doped film ICT carrier density.

in Section 3, below, that we can obtain good estimates of carrier concentrations from spectroscopy via a more indirect method.

Figure 2.1b also shows that increasing CF content produces a monotonic redshift of the main P1 absorbance peak near 0.4 eV that is concomitant with an increase in the relative intensity of the IRAV modes located near 0.16 eV, as highlighted by the black arrows. These two spectral features are hallmarks of greater polaron delocalization and increased carrier mobility.[21,42,43] We believe that this results from a solvent annealing effect. CF (b.p. = 61.2 °C) has a higher boiling point than DCM (b.p. = 39.6 °C), and the extra drying time and increased P3HT solubility during spin coating likely give P3HT crystallites more time to order, as we will demonstrate using GIWAXS data in the section below. It is also possible that the more soluble disordered polymer regions, corresponding to more blue-shifted P1 absorption, are the most likely to be dissolved away upon exposure to CF. Together, this means that increasing CF content when depositing F4TCNQ both increases the formation of CTCs but also makes those remaining carriers produced via ICT even more mobile.

Quantifying CTC Formation Using the F4TCNQ C≡N IR Stretching Modes.

Two features make the F4TCNQ C≡N vibrational modes particularly well suited for studying CTC formation: (1) the fact that the frequency of C≡N stretches are known to be highly sensitive to the local coulombic environment[44,45] and (2) the fact that the C≡N stretch frequencies occur near 2200 cm^{-1}, which places them in an IR spectral window that is largely absent of other vibrational modes. Although neutral F4TCNQ has a vibration that weakly absorbs near 2227 cm^{-1}, the fully anionic species produced by ICT undergoes a mode softening, bringing the vibrational frequency down to ~2190 cm^{-1}, as shown in Figure 2.2a. Because the energy of the C≡N stretching mode is highly dependent on the charge state of the dopant molecule, FTIR is better suited than

UV−Vis−NIR for quantifying the abundance of partial charge transfer states since the F4TCNQ stretching vibrational energy associated with CTCs appears at intermediate stretching frequencies just above 2200 cm^{-1}. [26,28,29] For the case when pure CF is used as the casting solvent, the purple curve in Figure 2.2a shows a well-defined peak at 2201 cm^{-1}, clearly revealing the presence of a large fraction of CTC states for this dopant casting condition.

Consistent with the electronic indications of CTC formation from the UV−Vis−NIR in Figure 2.1, Figure 2.2a shows that, as the fraction of CF is increased in the dopant casting solvent blend, the fraction of CTC states in the doped films also increases. Surprisingly, however, even when using pure DCM as the dopant casting solvent, the presence of the CTC peak near 2201 cm^{-1} never disappears. The ratio of CTC to ICT states, taken from the integrated peak areas in the IR spectrum and plotted as the blue curve in Figure 2.2b, reaches 0.04, but never zero. This suggests that, for sequential solution doping, there is always a small population of CTC states formed alongside the more predominant ICT phase when doping P3HT with F4TCNQ.

It is worth pointing out that the corresponding electronic transitions for the small fraction of CTC states produced at low CF fractions are not readily identifiable in the corresponding UV−Vis−NIR spectra. This is due to the already crowded nature of the electronic spectrum, the small population of CTCs generated for these doping conditions, and the fact that the CTC electronic absorption features likely have lower cross sections than the corresponding ICT features. However, using the integrated area peak fits from the FTIR spectra, we find that the CTC content can be controllably varied in these doped films by a factor of just over 10 as the fraction of CF in the dopant casting solvent is tuned from zero to 100%.

To better understand how the presence of CTCs affects the electronic properties of F4TCNQ-doped P3HT films, we also probed the in-plane conductivity of the various doped P3HT

films. Figure 2.2b (red squares) shows the electrical conductivity of the films as a function of CF composition in the doping solvent blend. A monotonic decrease in electrical conductivity is observed, going from 5.6 ± 0.3 S cm^{-1} when using pure DCM, down to 2.3 ± 0.3 S cm^{-1} when using pure CF as the casting solvent, a ~ 60% reduction in electrical conductivity. It is well known that the electrical conductivity is given by, $\sigma = pe\mu$, where μ is the free carrier mobility, p is the free carrier density, and e is the fundamental charge. Recently, we performed an analysis based on AC Hall effect measurements to show that, for P3HT, the energetic location of the P1 polaron band is strongly correlated with the free charge carrier mobility.[24] Thus, we can use this correlation, along with the measured electrical conductivity and P1 peak position, to estimate the free carrier density and mobility in our doped P3HT films as a function of CF fraction in the solvent used to infiltrate the F4TCNQ dopant. The precise way we accomplish this is described in both ref 24 and the Supporting Information, and the results are shown in Figure 2.2c.

The purple triangles in Figure 2.2c show that, as the fraction of CF in the dopant solution is increased, the estimated free carrier mobility actually increases from 0.036 cm2 V^{-1} s^{-1} for pure DCM up to 0.8 cm2 V^{-1} s^{-1} when using pure CF. These values are well within the range of Hall mobilities that have been measured previously for similarly doped P3HT films.[21,23,24] Given that the electrical conductivity decreases with increasing CF fraction, the increase in free carrier mobility reflects a strong decrease, over 80%, in the density of free carriers produced by ICT, shown as green squares/right axis in Figure 2.2c. We note that we spent a great deal of time attempting to quantify the CTC carrier concentration in these films from absorption, but this is challenging to do accurately because we do not know the cross sections of either the vibrational or electronic transitions of either the F4TCNQ anion or the CTCs. However, if we assume a similar total dopant loading density across this series of doped P3HT samples, then the drop in free carrier

concentration suggests a CTC dopant concentration of roughly 8×1020 cm^{-3}. Thus, free carriers created by ICT become more mobile with the use of CF as a doping solvent, but the overall electrical conductivity still drops due to the fact that free carriers produced by integer charge transfer are lost via conversion into CTCs.

Overall, IR spectroscopy and electrical conductivity show that the use of solvent blends in sequential doping affords a high degree of control over the relative population of CTCs compared to ICTs. Simply changing the amount of CF in the solvent used to infiltrate F4TCNQ into a P3HT film is enough to control the amount of CTCs present, allowing us to study their electronic, vibrational, and structural properties. The fact that we cannot entirely eliminate CTC formation, however, even using pure DCM as the dopant casting solvent, means that there is still significant room to improve the electrical properties of doped conjugated polymer films.

The Structure of P3HT:F4TCNQ CTCs via Grazing Incidence Wide-Angle X-ray Scattering.

To understand the local structures of the crystalline ICT and CTC states, we used 2D GIWAXS to probe films sequentially doped from different composition CF/DCM solvent blends. P3HT is well known to lie edge-on to the substrate, with its side chains oriented normal to the substrate and its π–π stacking oriented in the plane of the film (Figure 2.3a). Pristine P3HT has a monoclinic crystal structure where the angle of π–π stacking is tilted with respect to the unit cell b axis (Figure 2.3g).[46]

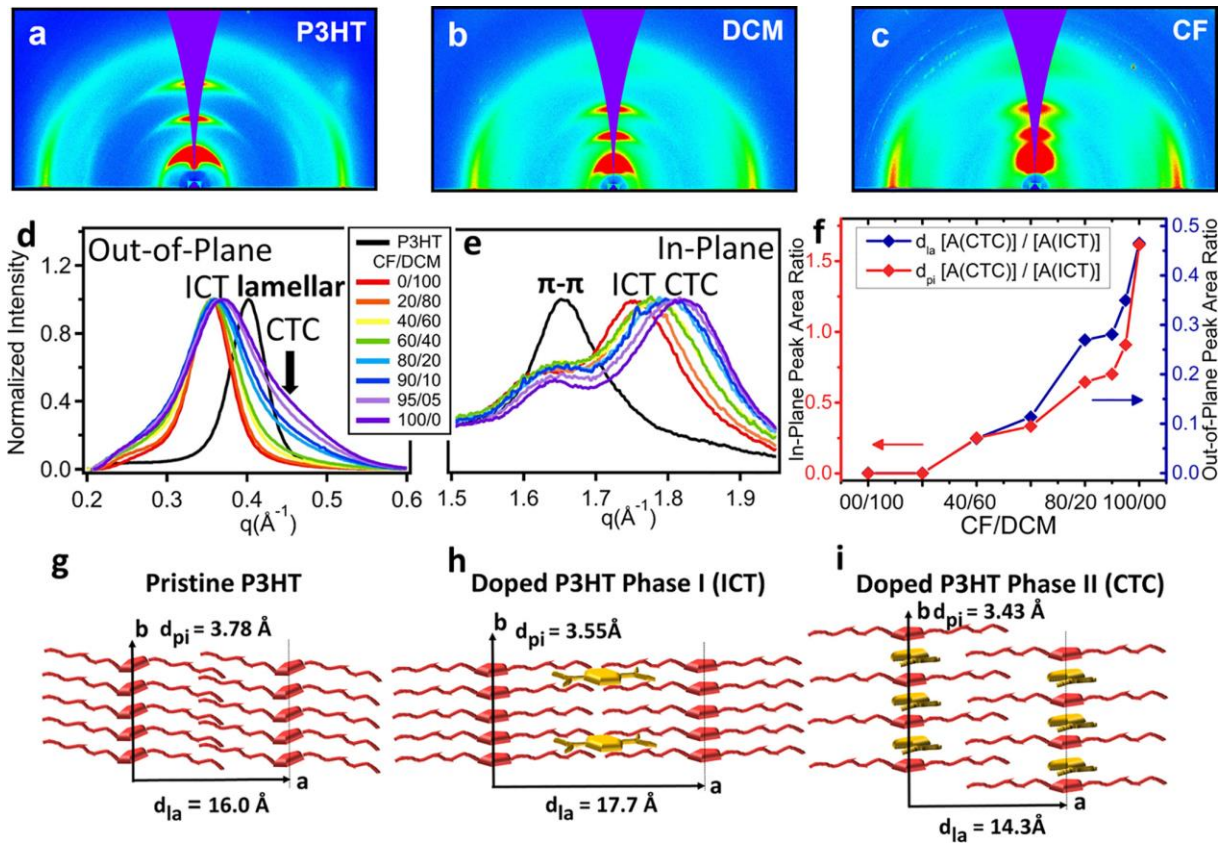

Figure 2.3: 2D GIWAXS diffractograms for films of (a) pristine P3HT, (b) P3HT sequentially doped with F_4TCNQ from 100% DCM, and (c) doped from 100% CF. The polymer chains in all samples maintain their edge-on orientation, but the peak positions, widths, and texture all change with doping and with the particular doping solvent composition. (d) Normalized out-of-plane and (e) in-plane integrations of thickness-normalized 2D GIWAXS diffractograms of P3HT sequentially doped with F_4TCNQ from blend solvents with different ratios of CF and DCM. The in-plane scattering from the π-stacking region in panel (e) shows a continuous shift to higher q and a broadening of the peak width as the CF fraction is increased. The out-of-plane scattering in the lamellar region in panel (d) shows that, with increasing CF ratio, a new peak appears at higher q. (f) Integrated GIWAXS peak area ratios for the CTC (phase II) relative to the ICT (phase I) structures, for both the out-of-plane lamellar (blue points) and in-plane π-stacking (red points) peaks. The structural trends match with what we deduced from the infrared C≡N stretch vibrations in Figure 2.2b. (g) Cartoon of the pristine P3HT crystal structure showing that the b direction is not precisely parallel to the π-stacking direction. (h) Cartoon of the ICT (phase I polymorph) structure of doped P3HT, showing how F_4TCNQ resides in the lamellar region of the crystallites and rearranges the unit cell, resulting in a decreased π distance (d_{pi}) and increased lamellar distance (d_{la}). (i) Cartoon of the CTC (phase II polymorph) structure of P3HT doped with F_4TCNQ. Because the incorporation kinetics are changed when CF is used as the dopant solvent, F_4TCNQ is capable of π-stacking with the P3HT backbone, forming an interdigitated lamellar structure with decreased lamellar and tighter π-stacking distances.

preserved, while Figure 2.3d (red curve labeled ICT) shows that the lamellar scattering peak shifts to a lower q. The red curve in Figure 2.3e shows that the π−π stacking peak splits into two, with one peak remaining near the original location and a new peak appearing at a higher q. [7,21−24,35] All of these shifts result from a rearrangement of the P3HT crystal structure upon doping, caused by the incorporation of F4TCNQ into the side-chain regions of the P3HT crystallites. The added F4TCNQ volume causes a reduction in the tilting of the π−π stacking direction with respect to the b axis and thus a reduction in the π spacing, as shown in Figure 2.3h.[22]

The fact that the dopants prefer to reside in the polymer lamellae (even for dopants that are physically larger than the lamellar spacing)[23,24] is important for helping to physically separate polarons from their counterions following ICT. This is because the low dielectric constant of organic semiconductors does a poor job of screening the interaction between the charge carriers on the polymer backbone and the dopant counteranion. When the dopant counterion in a crystallite is located among the polymer side chains, it is physically as far from the holes on the polymer backbone as possible, allowing the holes to move more freely.[21,23,42,43] Despite the preference for dopants to occupy the lamellae and thus be physically separated from the polaron, it has been estimated that only 5 to 10% of holes generated by doping P3HT with F4TCNQ become free charge carriers.[14,24]

In contrast to the ubiquitous formation of ICT states when paired with semiconducting polymers, F4TCNQ usually shows fractional charge transfer when combined with small organic donor molecules, forming CTCs as mentioned earlier.[47−49] Depending on the packing geometry and driving force for charge transfer, the degree of charge transfer can vary from 0 to 1.[13] Similarly, both experimental[32] and theoretical[50] work show that conjugated oligomers also have a tendency

to π-stack with F4TCNQ, which means that oligomers show a very different structural behavior when compared to their polymeric counterparts composed of the same monomer.[51]

This leads us again to the question of why CTCs form readily in charge-transfer salts, but much less so in doped conjugated polymers.[26–30] As discussed above, increasing the polymer solubility by casting at high temperatures[26] or forcing dopants out of the lamellae with branched side chains[27] can facilitate CTC formation. Moreover, Neelamraju et al. found that CTC formation can be the preferred doping mechanism in regiorandom P3HT, which is a highly amorphous material compared to the regioregular P3HT material studied in this work.[28]

The spectroscopic characterization presented above shows evidence for the co-existence of ICT and CTC states in P3HT films sequentially doped with F4TCNQ using CF/DCM solvent blends. Here, we draw similar conclusions based on structural evidence derived from GIWAXS. We find that changes in the diffraction patterns emerge as the CF ratio of the doping solvent increases, as seen in Figure 2.3a−c (intermediate CF/DCM ratios are shown in Figure S6 in the Supporting Information). As the fraction of CF in the doping solvent is increased, both the peak positions and widths evolve. In particular, when P3HT is doped using CF (Figure 2.3c), the scattering shows unusual broadening of both the lamellar and π-stacking peaks. In addition, thickness-normalized data in Figure S8 shows that the P3HT crystallite orientation becomes less edge-on with higher CF ratios in the doping solvent.

To better display the structural changes that take place upon doping, Figure 2.3d, e shows radially integrated 1D curves from the corresponding 2D scattering patterns. Panel (d) shows normalized out-of-plane integrations for the lamellar peak for different doping solvent blends. When P3HT is doped with F4TCNQ using DCM as the casting solvent (red curve), the peak from the pristine material (black curve) shifts to a lower q (higher d spacing), as expected for

intercalation of F4TCNQ into the crystalline lamellae.[21,22] As the fraction of CF in the doping solvent increases, the ICT lamellar peak remains in the same shifted position, but a shoulder grows in at a higher q, which fits best to a single new peak appearing around 0.44 $Å^{-1}$ (see Figure S7a in the Supporting Information for more details on fitting). This new peak can be assigned to the fundamental lamellar spacing of the CTC phase.[26]

Figure 2.3e shows the normalized in-plane integration in the π-stacking region for the same series of doped P3HT films. Here, we see that when pure DCM is used as the doping solvent (red curve), the original undoped π peak (black curve) decreases in intensity while a new π peak appears at 1.66 $Å^{-1}$, as expected when F4TCNQ occupies the lamellar region of the crystallites.[21,22] As the fraction of CF in the doping solvent increases, the doped-phase π-stacking peak appears to shift to a higher q and slightly broadens. A detailed analysis shows that this results from changes in intensity of two underlying peaks: the original doped lower q peak at 1.66 $Å^{-1}$ (ICT peak) decreases in intensity, while a second peak from the CTC phase appears at 1.84 $Å^{-1}$ when high fractions of CF are used (see Figure S7b for fits).

Both the out-of-plane lamellar peak at 0.44 $Å^{-1}$ and the in-plane π-stacking peak at 1.84 $Å^{-1}$ closely resemble those of the CTC polymorph described by Jacobs et al.[26] This provides structural confirmation that tuning the fraction of CF in the doping solvent controllably introduces a second polymorph of doped P3HT (labeled phase II in Figure 2.3i), which co-exists with the more familiar ICT phase I structure (Figure 2.3h). Since the new phase II shows a decrease in lamellar packing distance as well as a further decrease in π–π distance, we assign it to a CTC structure where F4TCNQ π-stacks with thiophene rings on the P3HT backbone and the side chains become further interlocked.[26]

We note that, in previous works, ICT was incorrectly postulated to take place via a π-stacking arrangement.[15,52] This makes the structural data presented here and in ref 26 interesting in that we can definitively correlate P3HT polymorphs with the F4TCNQ dopant occupying either the lamellar or the π-stacks to two unique charge transfer interactions with distinct spectroscopic and electronic properties.

With the caveat that GIWAXS only reports on the crystalline regions of a sample (and we know there can be significant amounts of F4TCNQ in the amorphous regions at high doping concentrations[23,53]), we can use the ratio of the integrated peak areas for each of the two phases to estimate their relative abundance. Figure 2.3f shows the ratio of the CTC and corresponding ICT peaks for both the lamellar (blue data points) and π-stacking (red data points) regions. The ratios of the two different peaks change in a similar fashion with increasing CF fraction, verifying that they are indeed reporting on the same new phase.

We believe that this results from the fact that CF's high dissolving power is capable of swelling and disrupting the P3HT crystallite structure to a much greater extent than DCM during the sequential doping process. This disruption allows F4TCNQ to intercalate between the P3HT π-stacks, producing the phase II polymorph associated with CTC doping. The appearance of the new phase monitored by GIWAXS also closely matches that monitored by the infrared absorbance of the C≡N stretch of the F4TCNQ, as shown in Figure 2.2b. Interestingly, the diffraction peak area ratio in Figure 2.3f increases somewhat more gradually than the IR peak area ratio, suggesting that CTC states formed at lower CF fractions occur with higher probability in disordered regions of the polymer, and thus affect the GIWAXS data less strongly than the IR absorption.

One additional question is whether the redshift in the P1 band observed in Figure 2.1b can be correlated with structural changes observed in GIWAXS. Figures S6 and S7 in the Supporting

Information show a systematic decrease in ICT scattering intensity with increasing CF fraction at all compositions below 100% CF. This decrease is likely due to the conversion of ICT states to CTC states. At 100% CF, the intensity jumps up, indicating that, despite significant CTC formation, the total crystallinity is also increasing. The fact that high CF fractions can dramatically crystallize formerly amorphous regions of the polymer is compatible with the idea that smaller amounts of CF can more subtly increase order in the already crystalline regions, helping to explain the redshift of the P1 peak observed in Figure 2.1b.

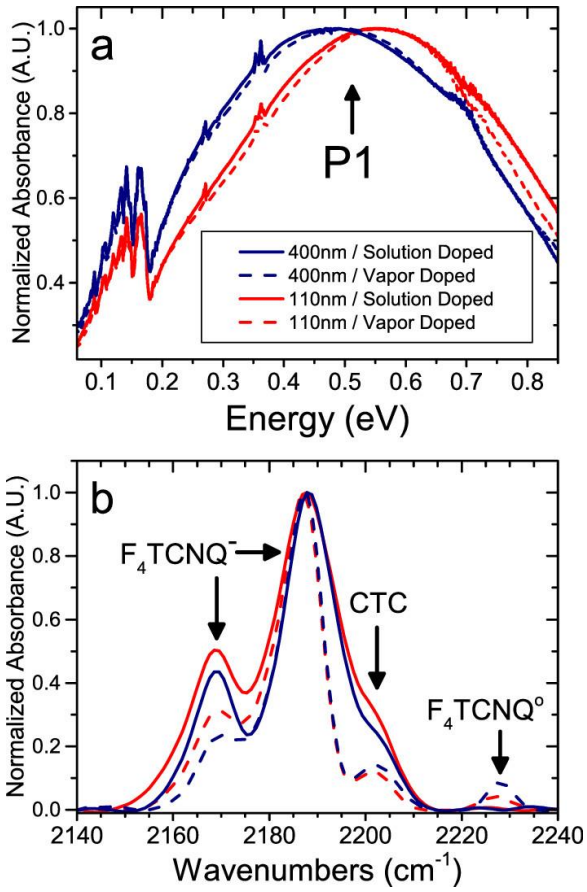

Figure 2.4: (a) FTIR absorption spectra normalized against max P1 intensity for a set of 400 nm-thick (blue curves) and 110 nm-thick (red curves) doped P3HT samples. Solid curves designate films treated by sequential solution doping with F_4TCNQ at 1 mg/mL from DCM. Dashed curves designate films doped with F_4TCNQ by vapor transport. (b) Inset view of the same set of spectra shown in (a) replotted in the wavenumber range for the C≡N stretching modes. In panel (a), the small set of peaks centered near ~0.27 eV on the P1 spectrum correspond to absorption of the F_4TCNQ vibrational modes.

Dopant Infiltration Method and CTC Formation.

Now that we have established that CF content can be used to tune the relative amounts of ICT and CTC formation in F4TCNQ-doped P3HT films, we next explore the effects of different dopant infiltration methods. In a previous work, our group performed a head-to-head comparison of sequential doping using solution vs evaporation deposition.[33] Evaporation, or vapor doping, involves exposing a pre-cast polymer film to a flux of dopant vapor created by sublimation. We found that vapor doping is every bit as effective as solution doping, even for very thick polymer films, and that vapor doping does a slightly better job of preserving the underlying crystallinity of the polymer film than solution doping.[33]

Figure 2.4 shows the IR absorption of two sets of sequentially doped P3HT films; one set based on underlying films of 110 nm thickness (red curves) and a second set based on underlying films of 400 nm thickness (blue curves). We have shown previously that, due to the spin-coating conditions for the pure material, the 400 nm-thick films have a higher total crystallinity compared to the 110 nm-thick films.[33] We then doped each set of films with F4TCNQ both by solution processing (solid curves), using 100% DCM as a casting solvent (1 mg mL^{-1}) as well as by vapor deposition (dashed curves) in an evaporator equipped with a QCM thickness monitor to achieve comparable doping levels. The increased IRAV absorption and redshift of the P1 band of the 400 nm thick films seen in Figure 2.4a make it clear that the thicker films have a greater degree of polaron delocalization and thus increased degree of order.[42,43] Figure 2.4a also shows that choice of sequential doping method has almost no effect on the degree of delocalization.

Figure 2.4b shows the FTIR spectra of these same films in the F4TCNQ C≡N stretching region. Unlike the electronic absorption, the FTIR data shows pronounced differences depending on the sequential processing method employed. The biggest difference is in the relative amplitude

of the CTC band at 2201 cm^{-1}, which is significantly higher for solution doping with DCM compared to evaporation doping. This suggests that evaporation doping goes further toward eliminating undesirable CTC formation than solution doping, independent of the initial degree of film crystallinity. From the perspective of kinetics, solution doping is much more effective at

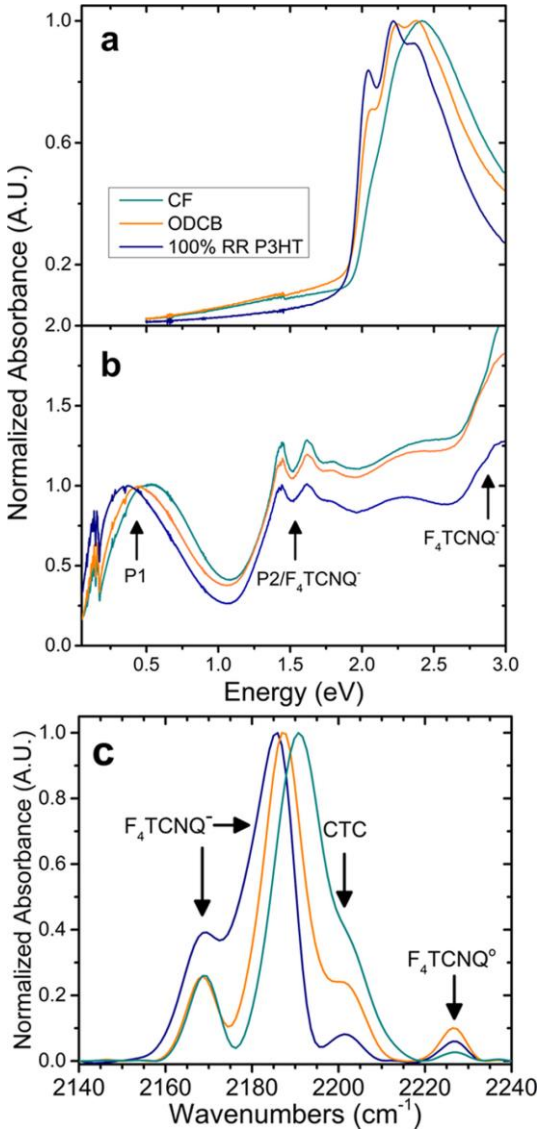

Figure 2.5: (a) UV–vis absorption spectrum of three different P3HT films with increasing crystallinity controlled by the evaporation kinetics of the solvent used to cast the film or the degree of polymer regioregularity. (b) UV–vis–NIR/FTIR combined spectrum for the same set of films after sequential solution doping with F_4TCNQ from DCM (1 mg mL^{-1}), normalized at the P1 band. (c) Vibrational spectra for the F_4TCNQ C≡N stretching mode for the same three films. The CTC peak near 2201 cm^{-1} clearly shows that lower polymer crystallinity is associated with forming more CTC states.

disrupting the existing P3HT π-stacks and thus at facilitating insertion of dopants in π-stacks and CTC formation. On the other hand, vapor transport is a minimally invasive processing technique during which P3HT π-stacks are less likely to be disrupted, causing CTC doping to be largely relegated to the amorphous polymer regions. In addition, the vapor-doped films show remarkably narrow ICT C≡N stretching modes, suggesting a more homogeneous population of ICT states. Overall, the data show that the choice of doping method can also control the extent of CTC formation, which may be important for many applications.

The Role of P3HT Crystallinity in CTC Formation.

One of the strongest advantages of sequential doping is that it allows for a degree of control over the total crystallinity of a doped polymer film.[21,23] Since the polymer layer is deposited first in sequential doping, the processing conditions (choice of solvent, spin speed, thermal annealing, etc.) can be chosen to enhance or reduce crystallinity as desired. In a previous work, we examined how controlling the crystallinity of pre-cast P3HT films affected the electrical and optical properties after sequentially doping with F4TCNQ.[21]

Here, we follow those same methods to prepare P3HT films of identical thickness with three different degrees of crystallinity, whose (undoped) UV−Visible absorption spectra are shown in Figure 2.5a. First, we cast the initial P3HT film from CF (prior to doping), which is a rapidly evaporating solvent that produces substantially more disordered, lower crystallinity films than traditional aromatic solvents used for polymer deposition (teal curve). The relatively low crystallinity is easily verified by the lack of vibronic structure in the UV− Vis[54,55] as well as by GIWAXS.[21] Second, we cast the P3HT films using our standard high boiling point solvent odichlorobenzene (ODCB) (orange curve), producing higher crystallinity films, as evident by both GIWAXS[21] and by the presence of vibronic structure in the UV−Visible absorption spectrum.

Finally, very high crystallinity films were obtained using a specially synthesized batch of P3HT with nearly 100% regioregularity,[56] also cast from ODCB (blue curve).

Figure 2.5b shows the UV−Vis−NIR absorption spectra of the same three films as panel (a) after solution sequential doping with F4TCNQ using pure DCM (1 mg mL^{-1}) as a casting solvent. As expected, the films with higher crystallinity show a red-shifted main P1 band near 0.4 eV and an increased relative IRAV band intensity near 0.16 eV.[21,23,24,42,43] The electrical conductivity, carrier mobility, free carrier concentration, and GIWAXS of films produced this way all have been discussed in our previous work; the electrical conductivity of the most crystalline film conditions is roughly seven times higher than that of the least crystalline, as a direct result of improved carrier mobility with increased crystallinity.[21]

Figure 2.5c shows the corresponding FTIR absorption spectrum of the F4TCNQ C≡N stretching modes in these same three doped P3HT films. Interestingly, the main (ICT) anion

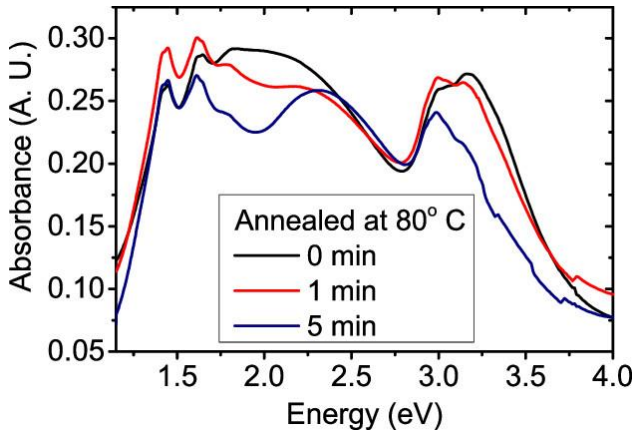

Figure 2.6: UV–Visible absorption spectra of P3HT films sequentially solution doped with F_4TCNQ (1 mg mL^{-1}) using 100% CF as the dopant casting solvent. The red curve represents a short annealing time of 1 min, while the blue curve represents annealing for 5 min. Thermal annealing at 80 °C was carried out in a nitrogen glovebox. Brief annealing for 1 min shows increased absorbance of the F_4TCNQ anion peaks near 1.5 and 3.0 eV and decreased CTC absorption near 2.0 eV, indicating a conversion of the CTC phase to the ICT phase without a significant loss of total doping. More extended annealing times lead to overall dedoping as well as a complete loss of the CTC phase.

absorption band shifts position from 2191 cm^{-1} in the least crystalline film (P3HT cast from CF) to 2185 cm^{-1} in the most crystalline film (100% RR P3HT). This suggests that the position of the ICT vibronic absorption band depends directly on the degree of overall crystallinity, with the more ordered environments producing a red-shifted vibronic band; we will explore this observation in more detail in future work.

In addition to the shift of the anion absorption associated with ICT, the data in Figure 2.5c show the distinct presence of the CTC peak in all three films, as evidenced by its vibronic absorption near 2201 cm^{-1}. The correlation is clear: the film with the lowest overall crystallinity has the largest fraction of CTCs, and vice versa for the most crystalline film. Given that the CTC requires π-stacking of the dopant and polymer, which is kinetically difficult to achieve in crystallites, it makes sense that CTC formation is favored in more disordered, amorphous films, where the requisite π-stacking geometry is easier to achieve.

Thermal Annealing and the Stability of CTC States.

The question of the relative thermodynamic stability of CTC and ICT phases in doped conjugated polymer films has also been a topic of considerable interest. Watts et al. recently argued that CTC states in P3HT films are thermodynamically preferred,[29] while Jacobs et al. showed that the CTC polymorph in their samples rapidly degraded when exposed to light or air, suggesting that the CTC states are kinetically unstable.[26] More recently, Zapata-Arteaga et al. investigated CTC formation following extended thermal annealing of vapor-doped conjugated polymer films and ultimately concluded that samples rich in the CTC phase are more thermally stable.[30]

Because of the control over CTC production afforded by our solvent blend method, we have also addressed this question here by exploring the effects of thermal annealing. Our goal is

to understand if the CTC phase, once formed, is only kinetically stable or is in fact the thermodynamically preferred phase. It is known that F4TCNQ can thermally desorb from doped P3HT films upon exposure to higher temperatures, leading to chemical dedoping of these films.[57] Thus, to test the stability of the CTC phase, we employed only modest heating for a short duration. Utilizing the full span of CF/DCM solvent blend ratios, doped P3HT films were placed on a hot plate at 80 °C for 1 to 5 min in a nitrogen atmosphere. The samples were removed promptly after the indicated time and allowed to cool to room temperature prior to analysis.

Figure 2.6 shows the results of thermally annealing our pure CF-doped films, which contain the highest fraction of CTC states, for different durations of time. Upon heating at 80 °C for 1 min, the two vibronic absorption peaks near 1.5 eV and an additional peak near 3.0 eV all from the F4TCNQ anion actually increase in intensity. This result is contrary to what is usually seen when annealing doped polymer films since heating typically leads to dedoping, resulting in a loss of all absorption features associated with the doped species.[57] The fact that we see increased absorption upon heating indicates that heating reverts the metastable CTC phase back to ICT. It is worth pointing out that if CTC states were simply being converted to ICT, we might expect to see isosbestic points in the spectra following different degrees of thermal annealing. However, because the thermal annealing process also causes a net dedoping of the P3HT film, the overall absorption of $F4TCNQ^{-}$ and neutral P3HT are also changing. As such, if we continue thermal annealing at this temperature for 5 min, the resulting UV−Vis spectrum loses overall intensity. More importantly, however, the spectrum obtained after 5 min of annealing looks quite similar to that obtained when using pure DCM as the doping solution, indicating that, at least at the level of sensitivity provided by electronic absorption, we can remove the CTC states while still leaving the majority of the ICT states intact.

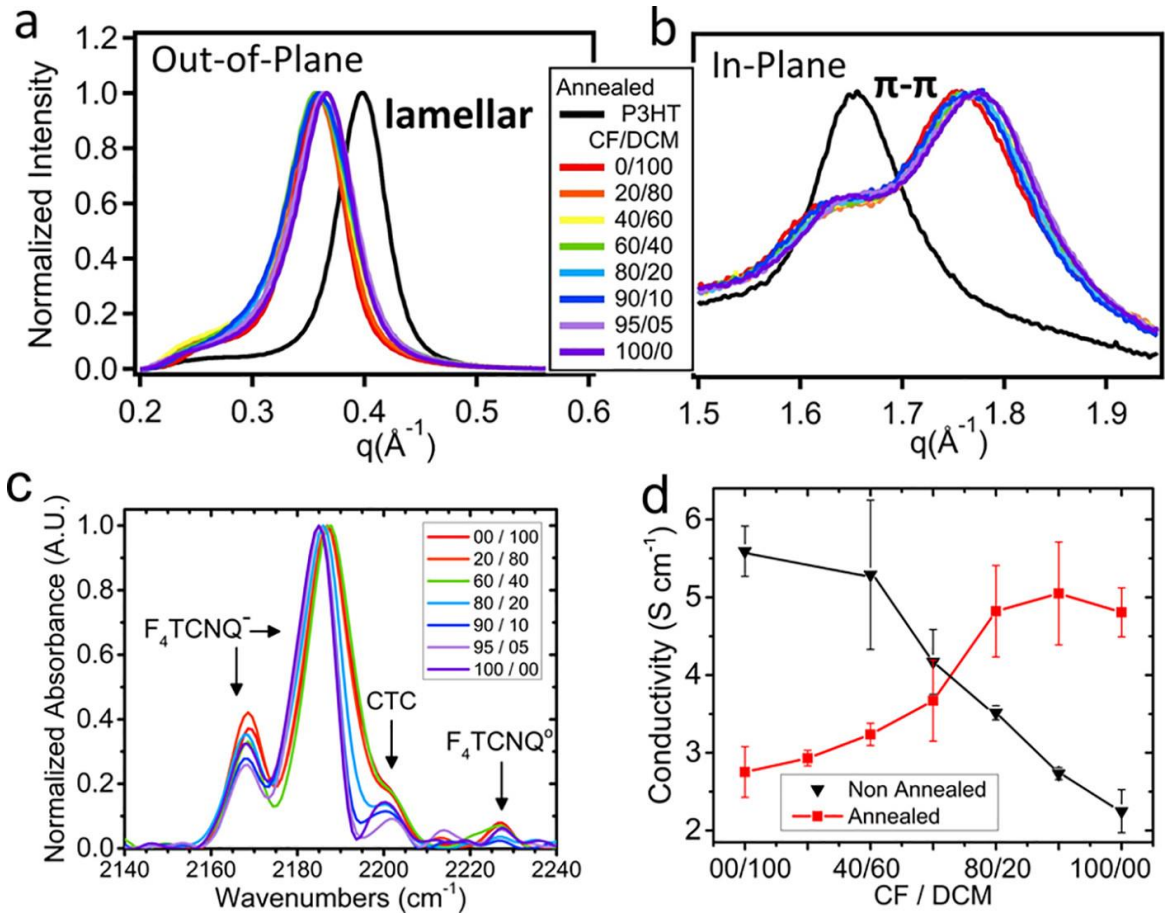

Figure 2.7: (a) Normalized out-of-plane and (b) in-plane integrations of thickness-normalized 2D GIWAXS diffractograms of P3HT films sequentially doped with F_4TCNQ from different ratio solvent mixtures of DCM and CF, subsequently annealed for 5 min at 80 °C. (c) Vibrational spectrum for the C≡N stretching mode after annealing. (d) In-plane conductivity of blend doped P3HT films prior to (black) and after annealing (red).

Remarkably, GIWAXS patterns of the doped P3HT films (Figure 2.7a, b) show that the new CTC phase II polymorph reverts entirely back to the phase I P3HT ICT crystal structure upon thermal annealing. Both the lamellar peak (Figure 2.7a) and the π-stacking peak (Figure 2.7b) lose all signatures of the CTC structure. These data provide direct structural evidence that the phase II CTC polymorph is a kinetically trapped phase. Upon thermal annealing, the dopants responsible for CTC formation physically relocate in the P3HT film and revert to the more preferred integer charge transfer doping mechanism. Moreover, the thickness-normalized GIWAXS data (Figures S8c, d and S9b in the Supporting Information) show that, after low-temperature thermal annealing,

both the lamellar and π-stacking peak intensities for samples doped using CF are higher than those for films processed from DCM. Even more surprising, the GIWAXS intensities for these annealed conditions are also higher than for the pristine P3HT intensity. Doped P3HT films usually show decreased lamellar peak intensities because doping usually induces some disordering.[21,23] The increased peak intensity we see after removing the CTC state (Figures 8a, b and 9a in the Supporting Information) by thermal annealing indicates that the original loss of peak intensity after doping from solvents with increasing CF fraction is due to conversion of ICT states to CTC states and not to induced disorder upon doping. Indeed, it appears that, fundamentally, CF serves as an annealing solvent during the doping process, which favorably rearranges the polymer microstructure. In the ICT state, this increased order can be observed in the P1 band (Figure 2.1b), and upon thermal conversion of the CTC states to ICT states, the increased order also can be clearly observed in the diffraction intensity.

Figures S8c, d in the Supporting Information also show that, after thermal annealing, the polymer crystallites in the P3HT films doped from CF become more edge-on than in unannealed films. Since the edge-on geometry is beneficial for in-plane conductivity, this could also help to explain the conductivity change after thermal annealing in Figure 2.7d.

The changes in structure seen by GIWAXS are directly reflected in the optical and electrical properties of the thermally annealed doped films. In the FTIR C≡N stretching region, shown in Figure 2.7c, the thermally annealed samples produced with DCM-rich doping solvent mixtures show little change relative to their unannealed counterparts (shown above in Figure 2.2a). This suggests that CTC states formed from CF poor solvents may be isolated doping sites in amorphous regions that can more favorably form the CTC π-stacked structure. In contrast, samples fabricated with CF-rich doping solvents almost entirely lose their CTC vibrational signature at

2201 cm^{-1} after thermal annealing. In fact, the vibrational spectra for these CF-rich, thermally annealed samples most closely resemble what was seen for our highest crystallinity predominantly ICT-doped films; in other words, annealing the samples doped from CF ultimately produces a film whose properties match the solution-doped 100% RR P3HT (Figure 2.5c) or the commercially available P3HT that was doped from the vapor phase (Figure 2.4b). The characteristic narrowing of the principal absorption peak and relatively small intensity for the CTC peak is a common feature shared across each of these processing methods and confirms that using CF as a doping solvent actually improves the overall crystallinity for the remaining P3HT. This also provides additional evidence that ICT is thermodynamically preferred: modest heating causes a marked reduction in the CTC peak at 2201 cm^{-1} where dopant molecules that π-stack with the P3HT backbone become free to diffuse until they can find a more stable configuration in the lamellae to undergo ICT.

Finally, Figure 2.7d shows the electrical conductivity of two series of identical samples doped from different solvent blends with one series subsequently being thermally annealed. As is typical for samples that use pure DCM as the doping solvent, thermal annealing decreases the electrical conductivity from 5.6 ± 0.3 to 2.8 ± 0.3 S cm^{-1} because thermally driven desorption of the F4TCNQ species leads to de-doping.[18,58] In contrast, for the samples sequentially doped from pure CF, annealing actually causes an increase in electrical conductivity from 2.3 ± 0.3 to 4.8 ± 0.3 S cm^{-1} , nearly the same value measured for unannealed DCM solvent-doped films. This behavior is also consistent with the idea that brief annealing causes F4TCNQ molecules that were kinetically locked in the metastable CTC π-stacking phase to revert back to the ICT doping mechanism, as corroborated by the C≡N stretching spectrum and the structural changes seen with GIWAXS. The drop in conductivity from any F4TCNQ lost to desorption appears to be more than

compensated for by the increased ICT carrier density and mobility due to enhanced crystallinity. Further annealing leads to additional dedoping, lowering the conductivity of all the films. An interesting crossover point exists near the 60/40 (CF/DCM) samples, which can be interpreted as a steady-state regime where the annealing induced desorption of F4TCNQ, the thermal conversion of CTC states into the ICT phase, and any annealing-induced changes in carrier mobility all compensate to cancel each other out. In combination, the X-ray, FTIR, and electrical conductivity data make clear that the application of modest heating can convert the CTC phase to the more desirable ICT phase. This shows that the CTC phase is kinetically accessible only under special processing conditions but is not thermodynamically preferred, which means that the application of small amounts of heat for short treatment times may greatly improve the performance of devices based on chemically doped conjugated polymers.

2.4 Summary

Overall, our work shows that even though ICT is the preferred mechanism of charge transfer in doped conjugated polymers, fractional charge transfer, i.e., CTC formation, also plays a significant, though sometimes hidden, role. Methods like UV− Vis−NIR and X-ray diffraction are incapable of detecting the presence of CTC species when they exist in small quantities: the electronic absorption of CTCs is likely weaker than those of the ICT states, and CTCs may also be associated with primarily amorphous regions in the polymer film, making them hard to detect via X-ray diffraction. Here, we show clearly that, even in the most crystalline P3HT films, produced either using vapor doping or with 100% regioregular material, we consistently see the presence of at least some charge transfer complexes after doping with F4TCNQ.

Why are CTCs generally harder to make and study in doped conjugated polymers than in small-molecule/oligomeric charge-transfer salts? The donor species in these charge transfer salts

do not have the large aliphatic side chains needed to confer solubility on most conjugated polymers. Thus, small molecules and oligomers tend to form co-crystals with electron acceptors that allow for the close spatial contact needed for wave function overlap and CTC formation. For conjugated polymers, there is not only much more space to place acceptors in the lamellae, but lamellar placement leads to much less disruption of the polymer crystal structure and polymer−polymer π-stacking than insertion into the π-stacks, as outlined in Figure 2.3g–i.

The propensity for CTCs to form in doped conjugated polymers is directly related to the degree of polymer swelling that takes place during the doping process, which in turn is linked to the fraction of amorphous regions. Indeed, we see that the relative abundance of CTCs in doped polymers increases with film swellability (and is minimized with evaporation doping), strongly suggesting that CTCs primarily reside in the disordered regions of the polymer film. This explains why CTC phases are rarely seen via GIWAXS since it is difficult to form them in large crystallites without specially controlling the processing, such as our use of CF, or via high temperature processing as demonstrated by Jacobs et al.,[26] or by specifically preventing lamellar intercalation through the use of branched side chains.[27]

The key observation in this work is that simple adjustment of the composition of the sequential processing solvent used to introduce the dopant can greatly influence the observed doping mechanism. The use of CF as a doping solvent likely redissolves the underlying polymer film and thus provides a route for the thermodynamically disfavored CTC state to form by initiating π-stacking between the dopant and the polymer in the disordered, partly dissolved state, and then preserving the kinetically trapped π-stacked structure into the solid state. This is likely the same mechanism that occurs in the hightemperature processing employed by Jacobs et al.[26] but should prove much easier to control for others to reproduce and further study. Moreover, we also

presented a recipe–modest thermal annealing for a brief period of time–to remove CTC states and convert them to the ICT phase without significant dedoping, providing a simple way to improve the electrical performance of doped conjugated polymer films.

Moreover, our results are reassuring in that they confirm that, for conjugated polymers, doping overwhelmingly takes place by integer charge transfer. This is because, under normal sequential doping conditions, the dopants prefer the lamellae, where they remain far from the extended π-system of the polymer. Thus, the addition of side chains to conjugated polymers meant to confer favorable solubility also happens to control the preferred type of charge transfer interaction. This is consistent with conclusions we drew when exploring the doping of P3HT films with dodecaborane acceptors that are larger in size (~2 nm) than the polymer lamellar spacing (~1.6 nm) but still prefer to reside in the lamellar region.[24]

Finally, when comparing dopant infiltration methods, vapor doping showed the smallest fraction of CTC states generated, independent of the degree of pre-formed polymer crystallinity. In a certain sense, vapor doping provides the absolute minimum kinetic facilitation for CTC doping, helping to explain why this method produces a notably smaller quantity of CTC states. Additionally, it seems clear that, under normal solution sequential doping conditions, the majority of CTC states are located in the amorphous polymer regions, and that the fraction of amorphous polymer will, in fact, also dictates the overall fraction of doping that takes place via the CTC mechanism. This work suggests that, to minimize the occurrence of CTC states when sequentially doping with F4TCNQ, one should strive for the highest crystallinity polymer possible and carry out the sequential doping process by thermal evaporation followed by brief low-temperature thermal annealing. These processing guidelines create the most conducive environment for

maximizing both the equilibrium free carrier concentration as well as charge carrier mobility in these materials.

2.5 Supporting Information

Experimental Methods

Optical & Electrical Measurements

UV-vis-NIR absorbance spectra were acquired between 300-2000 nm with a Shimadzu UV3101PC Scanning Spectrophotometer using polymer films prepared on glass substrates. FTIR absorbance of the P1 polaron band and F4TCNQ C≡N stretching mode were acquired between 480-5000 cm^{-1} using a Jasco FT/IR-420 spectrometer. The corresponding polymer films were prepared on KBr plates.

Figure S1 shows UV-vis spectra of P3HT films sequentially solution doped with F4TCNQ (1 mg mL^{-1}) from solvents with a wide range of solubilities towards P3HT: Acetonitrile (3×10^{-5} mg mL^{-1}), dichloromethane (0.818 mg mL^{-1}), and chloroform (38 mg mL^{-1}).[59] For dopant solvents with increased solubility towards P3HT, the neutral absorption of P3HT near 2.5 eV diminishes in the doped films. Once the solubility increases to a level like that of chloroform, the two peaks near 1.5 eV and third near 3.0 eV (dashed red lines) which are all indicative of ICT, become reduced in magnitude, while peaks near 2.0 eV and 3.3 eV (dashed green lines), which indicate new CTC transitions, increase in magnitude.

Figure S2 shows an unrefined set of spectra for the (20/80) CF/DCM solvent blend conditions, to illustrate the method used for constructing the combined UV-vis-NIR / FTIR spectra, for example, in Figure 2.1 of the main text. UV-vis-NIR spectra were acquired on films using glass

substrates and FTIR was acquired for the same film conditions cast on KBr plates. The two spectra were connected at 5000 cm^{-1} = 2000 nm = 0.619 eV in what is shown in the main text.

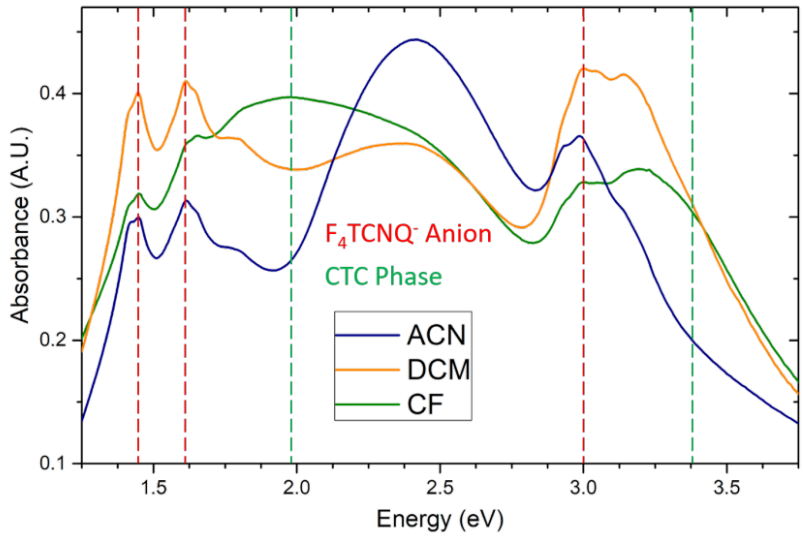

Figure S1: Films sequentially solution doped with F4TCNQ (1 mg mL^{-1}) from solvents with increasing solubility towards the underlying P3HT layer.

Doped polymer film samples used for measuring electrical conductivity were prepared on 1.5 × 1.5 cm^2 glass substrates. Resistivity was measured via a home-built four-point probe setup using the Van der Pauw method with electrodes placed at the corners of the substrate. In order to convert resistivity to conductivity, the corresponding film thicknesses were also measured for each sample using a Dektak 150 surface profilometer. At least three samples were measured for each doping condition. We note that our use of a macroscopic, cm-scale conductivity measurement generally produces lower values of conductivity than measurements from other groups that use electrodes spaced in the mm or even μm length range. Thus, our values are likely underestimates compared to those from other groups.

In previous work, we have shown using AC Hall effect measurements that there is a roughly linear relationship between the peak energy of the P1 polaron band absorption and the corresponding free carrier mobility for chemically-doped P3HT (Figure S3[24]) $\mu = -0.338\lambda_{max} + 0.206$, where λ_{max} is the P1 band peak position in eV and μ is given in $cm2V^{-1}\ s^{-1}$. Thus, the IR spectrum of doped P3HT films also includes implicit information about the free carrier mobility for each set of preparation conditions. Figure S4 shows an example of fitting the P1 band to a gaussian peak in the range of 0.25-0.6 eV to obtain a value for peak absorbance. We used this value to estimate the free carrier mobility. Then, using the known relationship between the electrical conductivity, σ, and carrier mobility, μ, shown in equation 1 (which is also mentioned in section 2 of the main text), we were able to estimate the free carrier concentration, p; these values are what are shown in Fig. 2c of the main text.

$$\sigma = pe\mu \tag{1}$$

Because accurate determination of the in-plane conductivity also requires knowledge of the film thickness, we measured the film thickness of our P3HT films as the doping solvent was tuned from

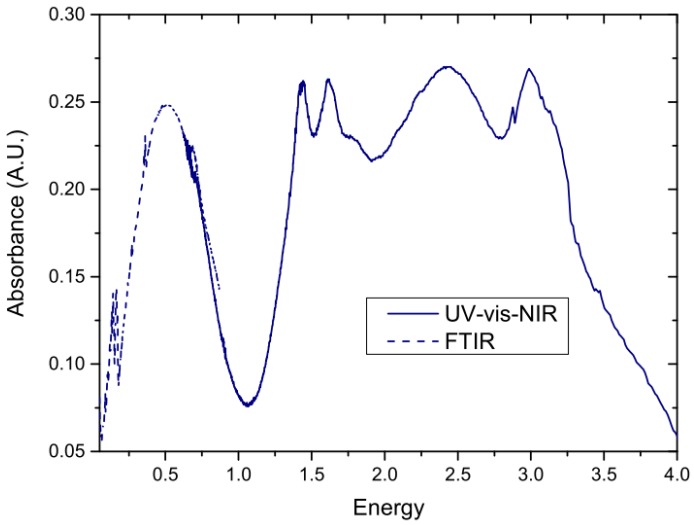

Figure S2: (Dashed blue) raw absorption profile captured from FTIR spectrometer. (Solid blue) raw absorption profile captured from UV-vis-NIR spectrophotometer.

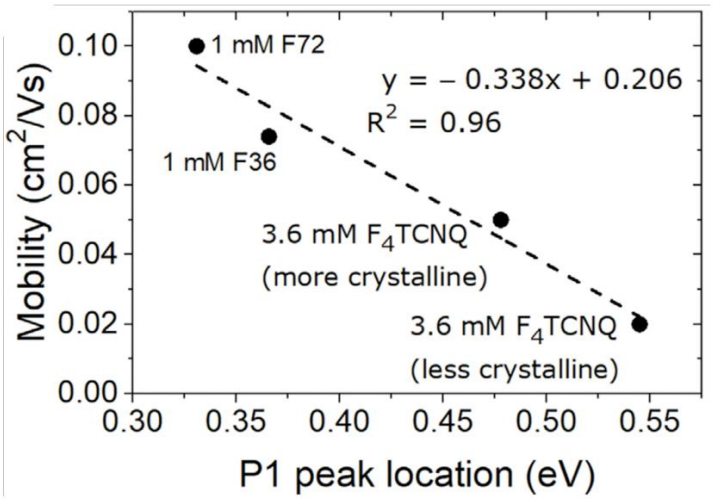

Figure S3: (Borrowed from ref 24) AC Hall determined mobility vs fitted P1 peak absorption. A roughly linear relationship exists between the two in this regime.

DCM to CF (Table S1). A consistent loss in P3HT film thickness is observed as the fraction of CF is increased, due to the fact CF has a higher dissolving power for P3HT than does DCM. We see that the overall thickness when using pure CF as the doping solvent results in a doped film that is 44% smaller in thickness compared to using pure DCM as the doping solvent.

F4TCNQ C≡N Vibrational Spectrum & Peak Fitting Details

F4TCNQ contains only a limited number of vibrational modes with significant absorptivity above 2000 cm^{-1}. For neutral F4TCNQ, there is a relatively weakly absorbing b_{1u} mode at 2227 cm^{-1} and a b_{2u} mode at 2214 cm^{-1}. Upon formation of the anionically charged species, these two modes gain significant oscillator strength, as well as soften to lower energy. We label these peaks of the F4TCNQ anion as $b_{1u}\nu_{2185}$ and $b_{2u}\nu_{2168}$. We assign the peak corresponding to the fractional charge transfer species as belonging to the b1u stretching mode, denoted here as $b_{1u}CTC$.

Peak fitting for all vibrational spectra was carried out by assigning three gaussian peaks and allowing the parameters (peak center of gravity, amplitude, and FWHM) to independently

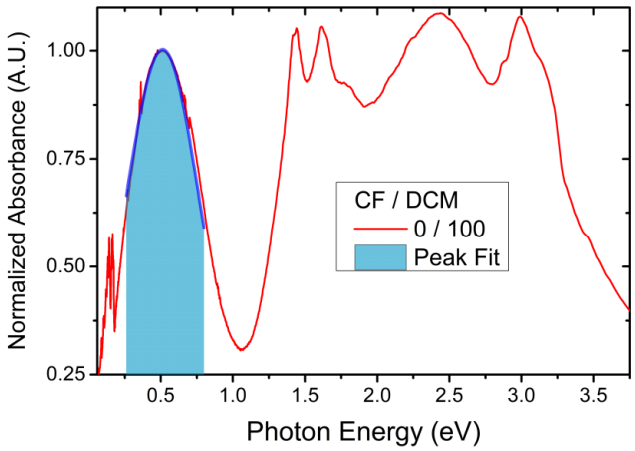

Figure S4: Example UV-Vis-NIR / FTIR spectrum showing overlayed gaussian fit for the P1 peak absorption (blue). The energy for the best fit P1 peak intensity is then used to estimate the free carrier mobility.

vary. Fitting was carried out by a non-linear least squares minimization following the Levenberg-Marquardt algorithm and allowed to iterate until converging with a χ^2 tolerance of at least 1×10^{-6}.

Table 2 shows that the relative amplitude for the b_{1u}*CTC* peak, which corresponds to partial charge transfer, monotonically increases as the fraction of CF is increased in the casting solvent. It's also interesting to point out that when only considering the ICT phase, peak $b_{1u}\nu_{2185}$ systematically redshifts from 2189 cm^{-1} from when pure DCM is used as the dopant casting solvent down to 2185 cm^{-1} when pure CF is used; this is nearly 10 cm^{-1} redshifted from the typically reported anion peak location at 2194 cm^{-1}. We believe this to be a consequence of the highly ordered, lamellar environment found for these sequential doping conditions, an idea further supported by the fact that the FWHM for this peak also decreases by ~30% as the solvent is changed from DCM to CF, indicating a more homogeneous environment for the remaining ICT phase.

Table S1: P3HT film thicknesses after sequential doping from CF/DCM solvent blends.

CF / DCM	Thickness (nm)
00/100	148 ± 6 nm
40/60	143 ± 12 nm
60/40	107 ± 9 nm
80/20	91 ± 6 nm
100/00	83 ± 8 nm

Table S2: Fitting parameters for the F4TCNQ vibrational spectra, sequentially doped from CF/DCM solvent blends.

	CF/DCM	**00/100**	**20/80**	**40/60**	**60/40**	**80/20**	**100/00**
	Adj. R-Square	0.9983	0.9991	0.9980	0.9970	0.9974	0.9948
$b_{2u}\nu_{2168}$	A	5.26	5.18	5.25	6.44	5.72	6.15
	c	2168.00	2167.84	2167.12	2166.75	2166.76	2167.38
	ω	9.65	11.09	10.42	12.10	12.07	12.53
$b_{1u}\nu_{2185}$	A	15.49	15.02	13.65	13.60	15.09	11.68
	c	2188.92	2188.39	2186.68	2185.86	2186.07	2184.79
	ω	15.49	14.17	13.33	13.10	14.44	11.04
$b_{1u}CTC$	A	0.60	1.47	3.92	4.36	5.38	6.08
	c	2203.08	2202.22	2197.91	2198.41	2200.16	2201.14
	ω	6.14	8.54	12.60	11.92	11.03	10.62

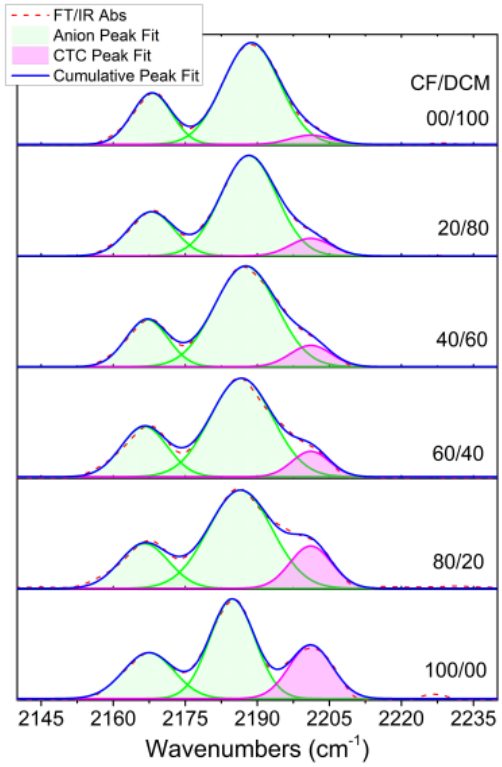

Figure S5: Peak fits overlayed on raw FTIR spectra for each solvent blend ratio. Peak fits for $b_{2u}\nu_{2168}$ and $b_{1u}\nu_{2185}$, shown in green. Peak fits for the intermediate CTC phase b_{1u}*CTC* shown in magenta.

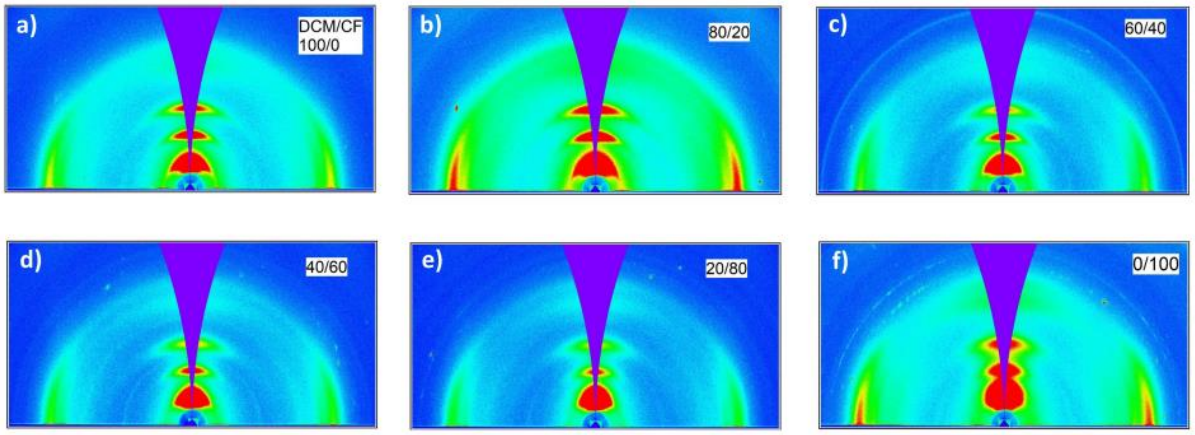

Figure S6: 2D diffractograms of P3HT SqP doped with F4TCNQ from solvent mixture of DCM/CF with ratio of (a)100/0, (b) 80/20, (c) 60/40, (d) 40/60, (e) 20/80 and (f) 0/100. With increasing CF ratio, the lamellar diffraction peaks broaden. The π diffraction peak moves to higher q as well as broadens. The doped P3HT transits from Phase I(ICT) to Phase II(CTC).

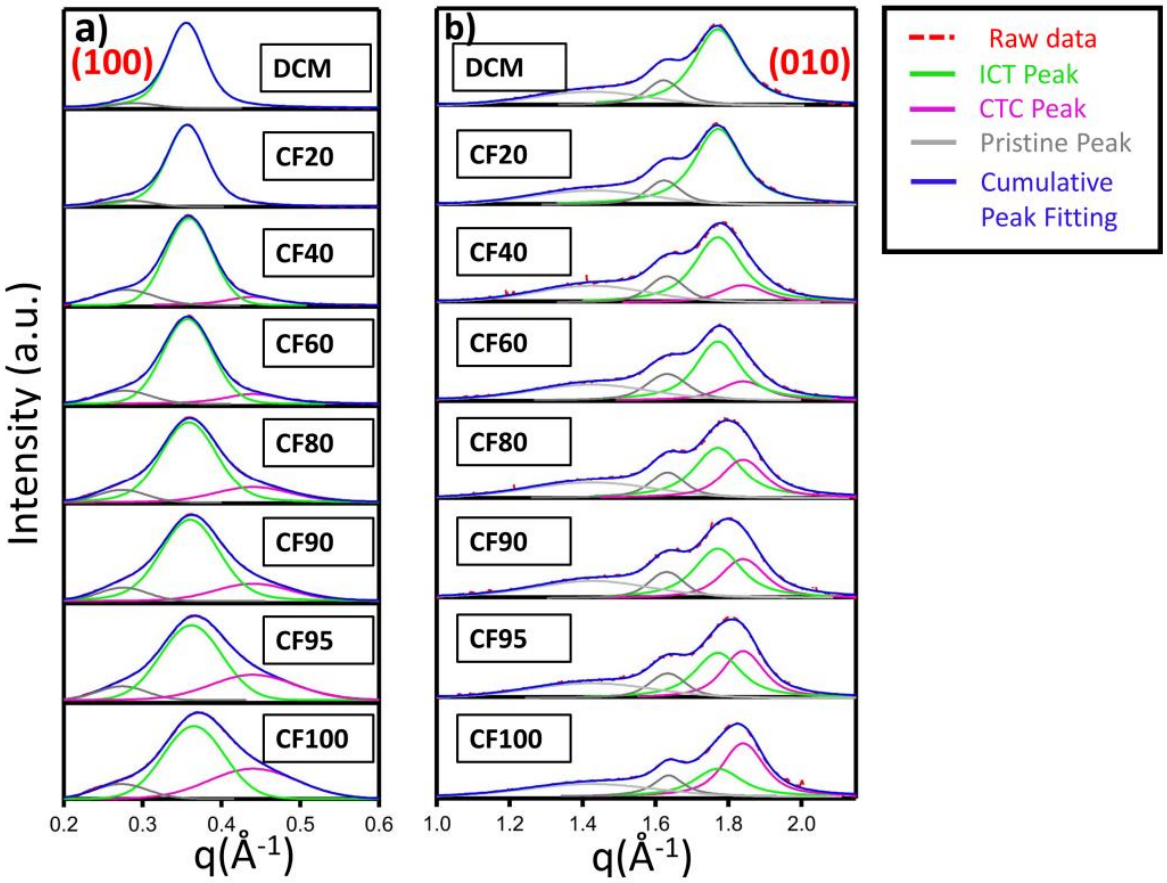

Figure S7: Peak fitting of lamellar (a) and π-π(b) peaks of doped P3HT with F4TCNQ SqP from mixture of DCM and CF with different ratio. With increasing CF ratio, there is a new lamellar peak coming up at 0.44 $^{\circ}A^{-1}$(pink curve, CTC peak) along with the commonly seen ICT peak (green curve). At the same time, the broadened π peak can be fitted to two peaks: an ICT peak (green curve) and a new peak located at 1.84 $^{\circ}A^{-1}$ (pink peak) that assigned to CTC peak. The new peaks in both lamellar and π direction correspond to a new doped P3HT phase (Phase II, CTC phase).

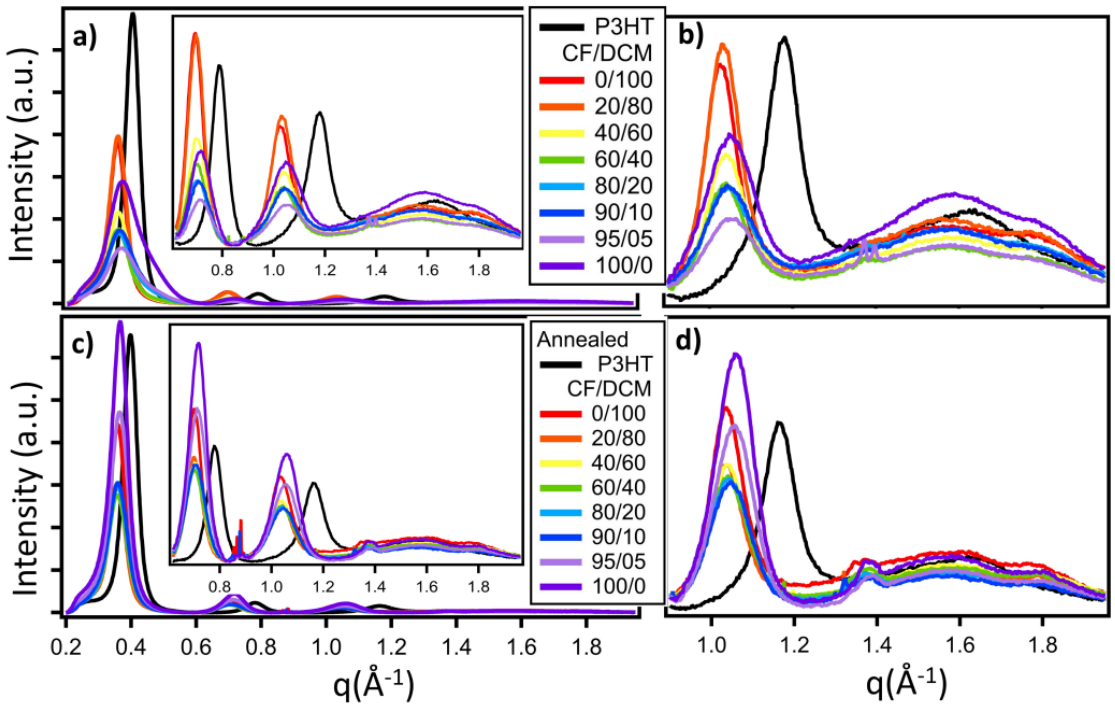

Figure S8: Out-of-plane integrated thickness-normalized 2-D GIWAXS diffractograms for P3HT doped with F4TCNQ SqP from different CF/DCM ratio before (a)(b) and after (c)(d) thermal annealing. The inset in (a) and (c) show the higher q region expanded in vertical direction. Similarly, (b) and (d) show more expanded π stacking region in (a) and (c).

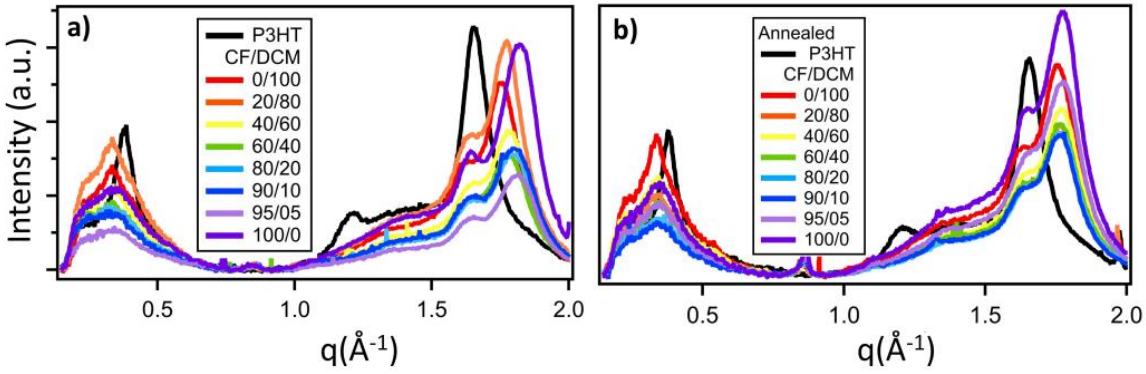

Figure S9: In-plane integrated thickness-normalized 2-D GIWAXS diffractograms for P3HT doped with F4TCNQ SqP from different CF/DCM ratio before (a) and after (b) thermal annealing.

2.6 References

(1) Kuik, M.; Wetzelaer, G. J. A. H.; Nicolai, H. T.; Craciun, N. I.; De Leeuw, D. M.; Blom, P. W. M. 25th anniversary article: Charge transport and recombination in polymer light-emitting diodes. Adv. Mater. 2014, 26, 512−531.

(2) Dou, L.; You, J.; Hong, Z.; Xu, Z.; Li, G.; Street, R. A.; Yang, Y. 25th anniversary article: A decade of organic/polymeric photovoltaic research. Adv. Mater. 2013, 25, 6642−6671.

(3) Russ, B.; Glaudell, A.; Urban, J. J.; Chabinyc, M. L.; Segalman, R. A. Organic thermoelectric materials for energy harvesting and temperature control. Nat. Rev. Mater. 2016, 1, 1−14.

(4) Cowart, J. S., Jr.; Liman, C.; Garnica, A.; Page, Z. A.; Lim, E.; Zope, R. R.; Baruah, T.; Hawker, C. J.; Chabinyc, M. L. Donorfullerene dyads for energy cascade organic solar cells. Inorg. Chim. Acta 2017, 468, 192−202.

(5) Hou, L.; Zhang, X.; Cotella, G. F.; Carnicella, G.; Herder, M.; Schmidt, B. M.; Patzel, M.; Hecht, S.; Cacialli, F.; Samorì, P. Optically ¨ switchable organic light-emitting transistors. Nat. Nanotechnol. 2019, 14, 347−353.

(6) Liang, Z.; Zhang, Y.; Souri, M.; Luo, X.; Boehm, A. M.; Li, R.; Zhang, Y.; Wang, T.; Kim, D. Y.; Mei, J.; et al. Influence of dopant size and electron affinity on the electrical conductivity and thermoelectric properties of a series of conjugated polymers. J. Mater. Chem. A 2018, 6, 16495−16505.

(7) Untilova, V.; Biskup, T.; Biniek, L.; Vijayakumar, V.; Brinkmann, M. Control of Chain Alignment and Crystallization Helps Enhance Charge Conductivities and Thermoelectric Power Factors in Sequentially Doped P3HT:F4TCNQ Films. Macromolecules 2020, 53, 2441−2453.

(8) Torrance, J. B.; Silverman, B. D. Charge transfer and ionic bonding in organic solids with segregated stacks. Phys. Rev. B 1977, 15, 788−801.

(9) Torrance, J. B.; Scott, B. A.; Kaufman, F. B. Optical properties of charge transfer salts of tetracyanoquinodimethane (TCNQ). Solid State Commun. 1993, 88, 971−975.

(10) Bryan, C. D.; Cordes, A. W.; Fleming, R. M.; George, N. A.; Glarum, S. H.; Haddon, R. C.; Oakley, R. T.; Palstra, T. T. M.; Perel, A. S.; Schneemeyer, L. F.; Waszczak, J. V. Conducting charge-transfer salts based on neutral π-radicals. Nature 1993, 365, 821−823.

(11) Ferraris, J.; Cowan, D. O.; Walatka, V.; Perlstein, J. H. Electron Transfer in a New Highly Conducting Donor-Acceptor Complex. J. Am. Chem. Soc. 1973, 95, 948−949.

(12) Shokaryev, I.; Buurma, A. J. C.; Jurchescu, O. D.; Uijttewaal, M. A.; De Wijs, G. A.; Palstra, T. T. M.; De Groot, R. A. Electronic band structure of tetracene-TCNQ and perylene-TCNQ compounds. J. Phys. Chem. A 2008, 112, 2497−2502.

(13) Goetz, K. P.; Vermeulen, D.; Payne, M. E.; Kloc, C.; McNeil, L. E.; Jurchescu, O. D. Charge-transfer complexes: New perspectives on an old class of compounds. J. Mater. Chem. C 2014, 2, 3065−3076.

(14) Pingel, P.; Neher, D. Comprehensive picture of p-type doping of P3HT with the molecular acceptor F4TCNQ. Phys. Rev. B 2013, 87, 115209.

(15) Cochran, J. E.; Junk, M. J. N.; Glaudell, A. M.; Miller, P. L.; Cowart, J. S.; Toney, M. F.; Hawker, C. J.; Chmelka, B. F.; Chabinyc, M. L. Molecular Interactions and Ordering in Electrically Doped Polymers: Blends of PBTTT and F4TCNQ. Macromolecules 2014, 47, 6836−6846.

(16) Salzmann, I.; Heimel, G. Toward a Comprehensive Understanding of Molecular Doping Organic Semiconductors (Review). J. Electron Spectrosc. Relat. Phenom. 2015, 204, 208−222.

(17) Scholes, D. T.; Hawks, S. A.; Yee, P. Y.; Wu, H.; Lindemuth, J. R.; Tolbert, S. H.; Schwartz, B. J. Overcoming Film Quality Issues for Conjugated Polymers Doped with F4TCNQ by Solution Sequential Processing: Hall Effect, Structural, and Optical Measurements. J. Phys. Chem. Lett. 2015, 6, 4786−4793. (18) Fuzell, J.; Jacobs, I. E.; Ackling, S.; Harrelson, T. F.; Huang, D. M.; Larsen, D.; Moulé, A. J. Optical Dedoping Mechanism for P3HT:F4TCNQ Mixtures. J. Phys. Chem. Lett. 2016, 7, 4297−4303.

(19) Jacobs, I. E.; Aasen, E. W.; Oliveira, J. L.; Fonseca, T. N.; Roehling, J. D.; Li, J.; Zhang, G.; Augustine, M. P.; Mascal, M.; Moule, A. J. Comparison of Solution-Mixed and Sequentially Processed P3HT:F4TCNQ Films: Effect of Doping-Induced Aggregation on Film Morphology. J. Mater. Chem. C 2016, 4, 3454−3466.

(20) Kang, K.; Watanabe, S.; Broch, K.; Sepe, A.; Brown, A.; Nasrallah, I.; Nikolka, M.; Fei, Z.; Heeney, M.; Matsumoto, D.; et al. 2D Coherent Charge Transport in Highly Ordered Conducting Polymers Doped by Solid State Diffusion. Nat. Mater. 2016, 15, 896− 902.

(21) Scholes, D. T.; Yee, P. Y.; Lindemuth, J. R.; Kang, H.; Onorato, J.; Ghosh, R.; Luscombe, C. K.; Spano, F. C.; Tolbert, S. H.; Schwartz, B. J. The Effects of Crystallinity on Charge Transport and the Structure of Sequentially Processed F4TCNQ-Doped Conjugated Polymer Films. Adv. Funct. Mater. 2017, 27, 1702654.

(22) Hamidi-Sakr, A.; Biniek, L.; Bantignies, J.-L.; Maurin, D.; Herrmann, L.; Leclerc, N.; Lévêque, P.; Vijayakumar, V.; Zimmermann, N.; Brinkmann, M. A Versatile Method to Fabricate Highly In-Plane Aligned Conducting Polymer Films with Anisotropic Charge Transport and Thermoelectric Properties: The Key Role of Alkyl Side Chain Layers on the Doping Mechanism. Adv. Funct. Mater. 2017, 27, 1700173.

(23) Aubry, T. J.; Axtell, J. C.; Basile, V. M.; Winchell, K. J.; Lindemuth, J. R.; Porter, T. M.; Liu, J. Y.; Alexandrova, A. N.; Kubiak, C. P.; Tolbert, S. H.; Spokoyny, A. M.; Schwartz, B. J. DodecaboraneBased Dopants Designed to Shield Anion Electrostatics Lead to Increased Carrier Mobility in a Doped Conjugated Polymer. Adv. Mater. 2019, 31, 1805647.

(24) Aubry, T. J.; Winchell, K. J.; Salamat, C. Z.; Basile, V. M.; Lindemuth, J. R.; Stauber, J. M.; Axtell, J. C.; Kubena, R. M.; Phan, M. D.; Bird, M. J.; et al. Tunable Dopants with Intrinsic Counterion Separation Reveal the Effects of Electron Affinity on Dopant Intercalation and Free Carrier Production in Sequentially Doped Conjugated Polymer Films. Adv. Funct. Mater. 2020, 30, 2001800.

(25) Ghani, F.; Opitz, A.; Pingel, P.; Heimel, G.; Salzmann, I.; Frisch, J.; Neher, D.; Tsami, A.; Scherf, U.; Koch, N. Charge transfer in and conductivity of molecularly doped thiophene-based copolymers. J. Polym. Sci., Part B: Polym. Phys. 2015, 53, 58−63.

(26) Jacobs, I. E.; Cendra, C.; Harrelson, T. F.; Bedolla Valdez, Z. I.; Faller, R.; Salleo, A.; Moulé, A. J. Polymorphism controls the degree of charge transfer in a molecularly doped semiconducting polymer. Mater. Horiz. 2018, 5, 655−660.

(27) Thomas, E. M.; Davidson, E. C.; Katsumata, R.; Segalman, R. A.; Chabinyc, M. L. Branched Side Chains Govern Counterion Position and Doping Mechanism in Conjugated Polythiophenes. ACS Macro Lett. 2018, 7, 1492−1497.

(28) Neelamraju, B.; Watts, K. E.; Pemberton, J. E.; Ratcliff, E. L. Correlation of Coexistent Charge Transfer States in F 4 TCNQDoped P3HT with Microstructure. J. Phys. Chem. Lett. 2018, 9, 6871−6877. (29) Watts, K. E.; Neelamraju, B.; Ratcliff, E. L.; Pemberton, J. E. Stability of Charge Transfer States in F 4 TCNQ-Doped P3HT. Chem. Mater. 2019, 31, 6986−6994.

(30) Zapata-Arteaga, O.; Dorling, B.; Perevedentsev, A.; Martin, J.; Reparaz, J. S.; Campoy-Quiles, M. Closing the Stability-Performance Gap in Organic Thermoelectrics by Adjusting the Partial to Integer Charge Transfer Ratio. Macromolecules 2020, 53, 609−620.

(31) Salzmann, I.; Heimel, G.; Oehzelt, M.; Winkler, S.; Koch, N. Molecular Electrical Doping of Organic Semiconductors: Fundamental Mechanisms and Emerging Dopant Design Rules. Acc. Chem. Res. 2016, 49, 370−378.

(32) Méndez, H.; Heimel, G.; Winkler, S.; Frisch, J.; Opitz, A.; Sauer, K.; Wegner, B.; Oehzelt, M.; Röthel, C.; Duhm, S.; et al. Charge-transfer crystallites as molecular electrical dopants. Nat. Commun. 2015, 6, 8560.

(33) Fontana, M. T.; Stanfield, D. A.; Scholes, D. T.; Winchell, K. J.; Tolbert, S. H.; Schwartz, B. J. Evaporation vs Solution Sequential Doping of Conjugated Polymers: F4TCNQ Doping of MicrometerThick P3HT Films for Thermoelectrics. J. Phys. Chem. C 2019, 123, 22711−22724.

(34) Vijayakumar, V.; Zhong, Y.; Untilova, V.; Bahri, M.; Herrmann, L.; Biniek, L.; Leclerc, N.; Brinkmann, M. Bringing Conducting Polymers to High Order: Toward Conductivities beyond 10 5 S cm 1 and Thermoelectric Power Factors of 2 mW m 1 K 2. Adv. Energy Mater. 2019, 9, 1900266.

(35) Patel, S. N.; Glaudell, A. M.; Peterson, K. A.; Thomas, E. M.; O'Hara, K. A.; Lim, E.; Chabinyc, M. L. Morphology Controls the Thermoelectric Power Factor of a Doped Semiconducting Polymer. Sci. Adv. 2017, 3, 24−26.

(36) Hynynen, J.; Kiefer, D.; Yu, L.; Kroon, R.; Munir, R.; Amassian, A.; Kemerink, M.; Müller, C. Enhanced Electrical Conductivity of Molecularly p-Doped Poly(3-hexylthiophene) Through Understanding the Correlation with Solid-State Order. Macromolecules 2017, 50, 8140−8148.

(37) Lim, E.; Peterson, K. A.; Su, G. M.; Chabinyc, M. L. Thermoelectric Properties of Poly(3-hexylthiophene) (P3HT) Doped with 2,3,5,6-Tetrafluoro-7,7,8,8- tetracyanoquinodimethane (F4TCNQ) by Vapor-Phase Infiltration. Chem. Mater. 2018, 30, 998−1010.

(38) Hynynen, J.; Kiefer, D.; Müller, C. Influence of crystallinity on the thermoelectric power factor of P3HT vapour-doped with F4TCNQ. RSC Adv. 2018, 8, 1593−1599.

(39) Mazaheripour, A.; Thomas, E. M.; Segalman, R. A.; Chabinyc, M. L. Nonaggregating Doped Polymers Based on Poly(3,4- Propylenedioxythiophene). Macromolecules 2019, 52, 2203−2213.

(40) Roesing, M.; Howell, J.; Boucher, D. Solubility characteristics of poly(3- hexylthiophene). J. Polym. Sci., Part B: Polym. Phys. 2017, 55, 1075−1087.

(41) Scholes, D. T.; Yee, P. Y.; Mckeown, G. R.; Li, S.; Kang, H.; Lindemuth, J. R.; Xia, X.; King, S. C.; Seferos, D. S.; Tolbert, S. H.; Schwartz, B. J. Designing Conjugated Polymers for Molecular Doping : The Roles of Crystallinity , Swelling , and Conductivity in Sequentially-Doped Selenophene-Based Copolymers. Chem. Mater. 2019, 31, 73−82.

(42) Ghosh, R.; Pochas, C. M.; Spano, F. C. Polaron Delocalization in Conjugated Polymer Films. J. Phys. Chem. C 2016, 120, 11394− 11406.

(43) Ghosh, R.; Chew, A. R.; Onorato, J.; Pakhnyuk, V.; Luscombe, C. K.; Salleo, A.; Spano, F. C. Spectral Signatures and Spatial Coherence of Bound and Unbound Po larons in P3HT Films: Theory Versus Experiment. J. Phys. Chem. C 2018, 122, 18048−18060.

(44) Meneghetti, M.; Pecile, C. Charge−transfer organic crystals: Molecular vibrations and spectroscopic effects of electron−molecular vibration coupling of the strong electron acceptor TCNQF 4. J. Chem. Phys. 1986, 84, 4149−4162.

(45) Haworth, N. L.; Lu, J.; Vo, N.; Le, T. H.; Thompson, C. D.; Bond, A. M.; Martin, L. L. Diagnosis of the Redox Levels of TCNQF 4 Compounds Using Vibrational Spectroscopy. ChemPlusChem 2014, 79, 962−972.

(46) Kayunkid, N.; Uttiya, S.; Brinkmann, M. Structural model of regioregular poly(3-hexylthiophene) obtained by electron diffraction analysis. Macromolecules 2010, 43, 4961−4967.

(47) Sutton, A. L.; Abrahams, B. F.; D'Alessandro, D. M.; Hudson, T. A.; Robson, R.; Usov, P. M. Structural and optical investigations of charge transfer complexes involving the radical anions of TCNQ and F4TCNQ. CrystEngComm 2016, 18, 8906−8914.

(48) Qin, Q.; Mague, J. T.; Moses, K. Z.; Carnicom, E. M.; Cava, R. J. Structure and characterization of charge transfer complexes of benzo[1,2-: B:3,4- b :5,6- b]trithiophene [C 3h-BTT]. CrystEngComm 2017, 19, 6355−6364.

(49) Sato, R.; Dogishi, M.; Higashino, T.; Kadoya, T.; Kawamoto, T.; Mori, T. ChargeTransfer Complexes of Benzothienobenzothiophene with Tetracyanoquinodimethane and the n-Channel Organic Field-Effect Transistors. J. Phys. Chem. C 2017, 121, 6561−6568.

(50) Valencia, A. M.; Cocchi, C. Electronic and Optical Properties of OligothiopheneF4TCNQ Charge-Transfer Complexes: The Role of the Donor Conjugation Length. J. Phys. Chem. C 2019, 123, 9617− 9623. (51) Aziz, E. F.; Vollmer, A.; Eisebitt, S.; Eberhardt, W.; Pingel, P.; Neher, D.; Koch, N. Localized Charge Transfer in a Molecularly Doped Conducting Polymer. Adv. Mater. 2007, 19, 3257−3260.

(52) Harrelson, T. F.; Cheng, Y. Q.; Li, J.; Jacobs, I. E.; RamirezCuesta, A. J.; Faller, R.; Moulé, A. J. Identifying Atomic Scale Structure in Undoped/Doped Semicrystalline P3HT Using Inelastic Neutron Scattering. Macromolecules 2017, 50, 2424−2435.

(53) Voss, M. G.; Scholes, D. T.; Challa, J. R.; Schwartz, B. J. Ultrafast transient absorption spectroscopy of doped P3HT films: distinguishing free and trapped polarons. Faraday Discuss. 2019, 216, 339–362.

(54) Spano, F. C. Modeling disorder in polymer aggregates: The optical spectroscopy of regioregular poly(3-hexylthiophene) thin films. J. Chem. Phys. 2005, 122, 234701–234715.

(55) Spano, F. C.; Clark, J.; Silva, C.; Friend, R. H. Determining Exciton Coherence from the Photoluminescence Spectral Line Shape in poly(3-hexylthiophene) Thin Films. J. Chem. Phys. 2009, 130, No. 074904.

(56) Bronstein, H. A.; Luscombe, C. K. Externally initiated regioregular P3HT with controlled molecular weight and narrow polydispersity. J. Am. Chem. Soc. 2009, 131, 12894–12895.

(57) Jacobs, I. E.; Moulé, A. J. Controlling Molecular Doping in Organic Semiconductors. Adv. Mater. 2017, 29, 1703063.

(58) Hase, H.; O'Neill, K.; Frisch, J.; Opitz, A.; Koch, N.; Salzmann, I. Unraveling the Microstructure of Molecularly Doped Poly(3-hexylthiophene) by Thermally Induced Dedoping. J. Phys. Chem. C 2018, 122, 25893–25899.

(59) Roesing, M.; Howell, J.; Boucher, D. Solubility characteristics of poly(3-hexylthiophene). Journal of Polymer Science, Part B: Polymer Physics 2017, 55, 1075–1087.

Chapter 3. Bulky Charge-Shielding Dodecaborane-Based Dopants: An Effective Strategy Towards the Production of Mobile Charge Carriers in the Amorphous Regions of Semiconducting Polymers

3.1 Introduction

Semiconducting conjugated polymers have many emerging applications including thin-film solar cells, flexible thermoelectrics, and wearable electronics.[1–3] A wide range of semiconducting polymers have been designed for specific applications that feature different backbone structures with different bandgap energies accompanied by tunable side chains to aid in polymer solubility. As synthesized, semiconducting polymers lack intrinsic charge carriers, so doping is necessary to add the charge carriers that permit electronic conduction.[4] Semiconducting polymers can undergo both *n*- and *p*-type doping, with the latter being more common. In *p*-type doping, electrons transfer from the polymer's valence band (HOMO level) to a dopant's LUMO level, forming a positively charged hole on the polymer backbone and a negatively charged counterion from the dopant. The hole charge carriers, along with their associated backbone deformation, are referred to as polarons. The density of charge carriers generated is related to both the oxidizing potential and concentration of the dopant, while the carrier mobility depends on the nanoscale structure of the polymer and on Coulombic charge-based interactions with the counterions.[5–9]

The electrical conductivity of a doped polymer is determined by both the density and mobility of charge carriers, so it is important to understand how doping influences these two quantities. Strong Coulombic binding between polarons and counterions can result in localized or trapped carriers that do not contribute to conductivity.[5–7] In crystalline polymer regions, dopant

molecules usually reside among the alkyl side chains, away from the polymer backbone.[8] This positioning is generally desirable, as it reduces the Coulombic binding between polarons and their counterions.[9] In disordered polymer regions, large void spaces between chains allow counterions to remain near polarons, which is largely responsible for the low conductivities observed in doped amorphous semiconducting polymers.[10] The ability of polymer crystallites to force charge separation by segregating polarons and counterions is therefore important for sample conductivity.

Many studies on regioregular (RR) and regiorandom (RRa) samples of the workhorse semiconducting polymer poly(3-hexylthiophene-2,5-diyl) (P3HT) have demonstrated that RRa P3HT is largely unable to form crystalline packing regions.[11,12] Relative to RR-P3HT, RRa-P3HT has an increased bandgap energy due to breaks in conjugation at sites of polymer rotation, so RRa-P3HT is harder to dope. Poor crystallinity also causes RRa-P3HT to have a low density of charge carrier percolation pathways and high Coulombic binding interactions with dopant counterions. All of these factors explain why doped RRa-P3HT shows much lower conductivities than its doped RR-P3HT counterpart.

In addition to polymer crystallinity, the choice of dopant is also critical to improving the electrical conductivity of doped conjugated polymers. Many dopants are small molecules that in amorphous polymer regions can closely associate with the polymer backbone. For example, the commonly used dopant 2,3,5,6-tetrafluoro-7,7,8,8-tetracyanoquinodimethane (F_4TCNQ) has a flat molecular geometry that allows for π-stacking with the polymer backbone in amorphous polymer regions, producing Coulombically bound charge-transfer complexes that do not contribute to electrical conductivity.[13] Even when not complexed, dopants like F_4TCNQ still provide enough Coulomb attraction to localize nearby polarons and thus reduce carrier mobility.

Dodecaborane (DDB) cluster-based dopants, by contrast, are a family of oxidizing agents that have been shown to successfully shield the Coulombic interaction between polaron-counterions pairs in RR-P3HT due to their large size (~2 nm in diameter).[14] These dopants are composed of a pseudo-icosahedral dodecaborane core on which each vertex is functionalized with a range of substituents that can be used to tune the redox potential of the molecule. A DDB-cluster with 3,5-bis(trifluoromethyl)benzyloxy substituents, referred to as DDB-F_{72} (see Figure 3.1a for chemical structure), was previously found to be an outstanding dopant for RR-P3HT. DDB-F_{72} has a redox potential that is nearly 0.5 V larger than F_4TCNQ, and it has been shown to achieve nearly 100% doping efficiency (i.e., one mobile carrier is produced for every dopant molecule) with film conductivities routinely exceeding 10 S/cm.[15]

In this work, we take advantage of the fact that DDB-F_{72} can inhibit the formation of Coulombically bound polaron-counterion pairs to improve the properties of doped RRa-P3HT. Using spectroscopic, electronic, and structural characterization methods, structure-conductivity relationships in amorphous RRa-P3HT were probed to better understand the doping of amorphous regions in semicrystalline conducting polymers.

3.2 Experimental and Methods

Materials

Regiorandom (RRa) poly(3-hexylthiophene-2,5-diyl) (P3HT) (Rieke metals inc., M_w = 30-90 K), and regioregular (RR) P3HT (4002-EE, Rieke metals inc., M_n = 50-70 K, regioregularity 91-94%, polydispersity 2.0-2.5) were used as purchased. The dopant molecule DDB-F_{72} was synthesized in-house following established procedures.[14–16]

Film Fabrication

Glass and silicon substrates were cleaned by sonicating in Alconox detergent aqueous solution, acetone, and isopropanol sequentially for 15 minutes each, followed by plasma cleaning using a Harrick plasma cleaner PDC-32G for 15 minutes. Film fabrication was carried out in a glove box under nitrogen. RR-P3HT and RRa-P3HT films were spin-coated at 1000 rpm for 60 seconds from 20 mg/mL polymer solutions in 1,2-dichlorobenzene (ODCB, Sigma Aldrich, anhydrous, 99%). Film thickness measurements were taken on a Dektak profilometer. The DDB-F_{72} dopant was applied to the pre-cast P3HT films by solution sequential processing (SqP) from *n*-butyl acetate (*n*-BA, Fisher Scientific, reagent grade, dried by stirring with magnesium sulfate and subsequent distillation) at the stated concentrations.[17] Once applied, the dopant solution soaked the polymer films for 20 seconds before spin-coating at 4000 rpm for 10 seconds. Previous work has demonstrated that the SqP method effectively delivers the DDB-based dopants throughout the polymer films.[15]

Absorption Spectroscopy

UV-vis-NIR absorption spectra were acquired from 300-3000 nm using a Shimadzu UV3101PC Scanning Spectrophotometer for films prepared on glass substrates. FT-IR data was acquired from 220-7000 cm^{-1} for matched samples prepared on KBr plates using a Jasco FT/IR-420 spectrometer.

Conductivity Measurements

Conductivity measurements were taken on 1.5 × 1.5 cm glass substrates with thermally evaporated silver contacts placed at the corners of the subtrates. Sheet resistance measurements were taken using the van der Pauw technique with a Keithley 2400 SourceMeter controlled by

Labview software. The max current sourced was held to 1 mW. Reported conductivity values are the average of at least three distinct samples.

Neutron Reflectometry (NR) Measurements

Reflectivity measurements were performed on the Liquids Reflectometer (LIQREF), BL-4B, at the Spallation Neutron Source (SNS) of the Oak Ridge National Laboratory (ORNL) with a 2D position-sensitive ^{3}He detector. A 3.4 Å bandwidth, extracted from a wavelength range of 2.55-16.70 Å, was used at measurement angles of 0.60˚ and 1.19˚ to attain a *q*-range of 0.008 to 0.102 Å^{-1}. The measured films were fabricated on 1.5 × 1.5 cm silicon substrates (B-doped, *p*-type, <100> oriented) using 0.85 mM dopant solutions by SqP. The beam footprint was kept constant through adjustments in the slit opening commensurate with the angle of incidence. Data reduction was done using RefRed, and subsequent analysis was performed on ORNL's Web Interface (Webi) using NIST's Refl1D python package.[18]

To fit the NR data, the free parameters of layer thickness, scattering length density (SLD), and layer roughness were given estimated ranges that were optimized by an in-built machine-learning algorithm. Extra layers were added or removed based on the resulting fit parameters.[18] To remove any potential bias in the fits, numerical fittings were performed independently by two people before comparing the results. The SLD contributions of the DDB-F_{72} dopant and the RRa-P3HT matrix to the active layer SLD were taken from a calculated SLD for the DDB-F_{72} molecule and a measured SLD for pure RRa-P3HT. SLD contributions for both the DDB-F_{72} molecule and for RRa-P3HT monomer were normalized by the number of atomic nuclei per monomer.

Grazing Incidence Wide Angle X-ray Scattering (GIWAXS)

Films for GIWAXS measurements were prepared on 1 cm × 1 cm single-crystal silicon substrates (B-doped, *p*-type, <100> oriented). Measurements were performed at the Advanced Photon Source (APS) on beamline 8ID-E with a 10.92 KeV X-ray beam incident at 0.133° and a detector distance of 217 mm. Calibration and gap-filling of the obtained 2D diffractograms was performed using the MATLAB toolbox GIXSGUI. Radial integration between 0-10˚ (out-of-plane) and 80-90˚ (in-plane) relative to the positive sample z-axis as well as baseline corrections and peak fitting were performed in IgorPro 8 using the WAXSTools package.[19]

Grazing Incidence Small Angle X-ray Scattering (GISAXS)

Films for 2D GISAXS measurements were prepared on 1.5 cm × 1.5 cm single-crystal silicon substrates (B-doped, *p*-type, <100> oriented). Measurements were performed at the Stanford Synchrotron Radiation Lightsource (SSRL) on beamline 1-5 using a wavelength of 1.0332 Å at an incident angle of 0.14°. 2D GISAXS patterns were calibrated and analyzed using the Nika package on Igor Pro 8.[20] 1D GISAXS patterns were calculated by vertically integrating the Yoneda peak, or the high intensity scattering near the critical angle of the polymer film due to the Vineyard effect.[21]

Alternating Current (AC)-Field Hall Effect Measurements

Doped P3HT films for AC-Field Hall Effect measurements were made on 1 cm × 1 cm glass substrates. Following film fabrication, silver electrodes were thermally evaporated on the corners of the samples with an Angstrom Engineering, Inc. evaporator at a pressure < 1 μTorr and a deposition rate of 0.5 Å/s up to 10 nm, followed by 1 Å/s to a final thickness of 60 nm. Samples were packaged in scintillation vials under argon atmosphere before being sent for testing. AC-field

Hall measurements were performed with a Lake Shore model 8400 series AC-field Hall probe system at a field strength of 0.6484 T and a current of 10.0 µA under flowing nitrogen. The AC-field instrument allows the Hall voltage to be readily distinguished from the static misalignment offset voltage, which can be quite large in low mobility materials.

3.3 Results and Discussions

To characterize the doping of RR- and RRa-P3HT with DDB-F_{72}, we must first understand the relative polymer and dopant energies involved. Figure 3.1a shows the relative valence and conduction band energy levels for RR-P3HT and RRa-P3HT as well as the LUMO level of DDB-F_{72}. The bandgap energy of ~2.8 eV appears as a strong absorbance peak in undoped RRa-P3HT, as seen by the black curve in Figure 3.2a. As RRa-P3HT is doped with DDB-F_{72}, the removal of

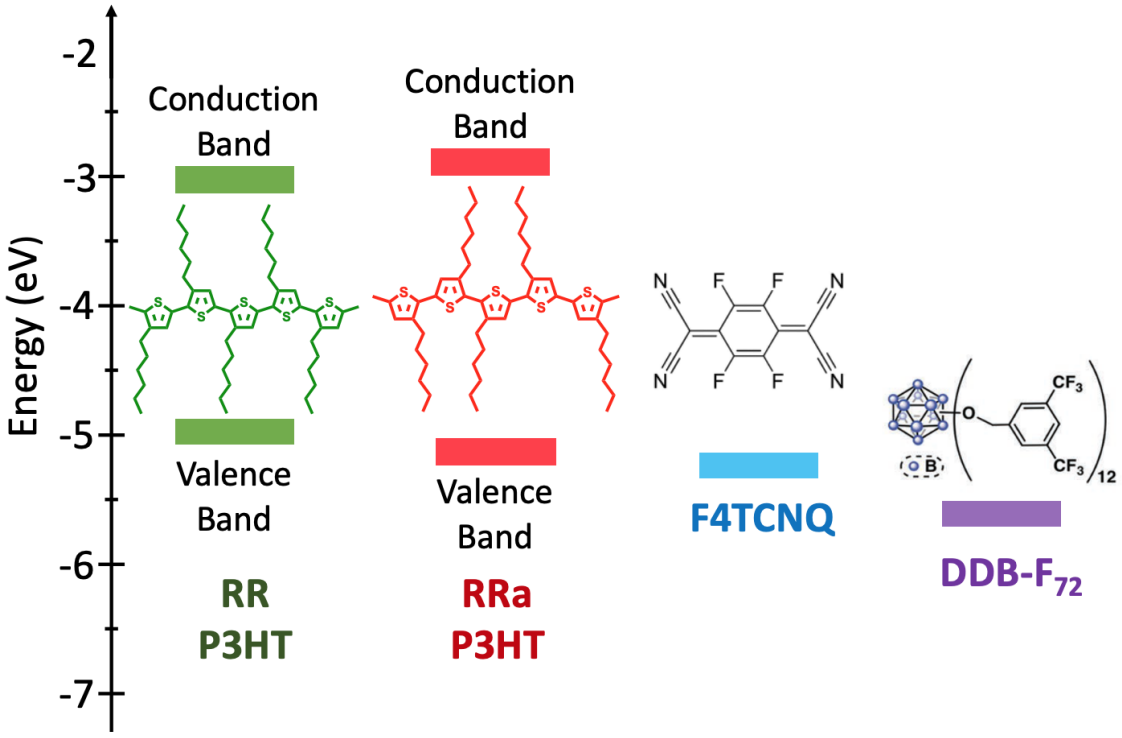

Figure 3.1: (a) Energy diagram of RR-P3HT, RRa-P3HT, and the F4TCNQ and DDB-F_{72} dopants. The valence band of RRa-P3HT is lower in energy than that of RR-P3HT due to the amorphous nature of the polymer.

electrons from the valence band and the creation of intra gap states causes the intensity of the bandgap transition to decrease and new peaks corresponding to polaronic transitions (P1 and P2) to appear.[22] Visually, these changes in absorbance upon doping result in a color change of the RRa-P3HT film from yellow/orange when undoped to purple when doped (Figure 3.2a inset). For the 1 mM DDB-F_{72} doping solution (red curve), the bandgap transition peak is largely absent, and an absorption peak at 2.4 eV corresponding to the DDB-F_{72} anion[15] becomes readily evident, indicating that the film is highly doped.

In our previous work, we studied the doping of RR-P3HT with DDB-F_{72}.[9,23] For RR-P3HT, we demonstrated that the more a polaron is Coulombically bound to its counterion, the more blue-shifted its P1 absorption peak is.[8,14] The P1 absorption peaks for DDB-F72-doped RR- and RRa-P3HT are shown in Figure 3.2b. The P1 peaks for F4TCNQ-doped RR- and RRa-P3HT from our previous work are also included for comparison.[8,23] The higher P1 transition energy for DDB-F_{72}-doped RRa-P3HT versus RR-P3HT is likely due to the larger bandgap energy of RRa-P3HT, as shown in Figure 3.1. The doped states for RR- and RRa-P3HT are depicted there to be similar in energy, a result supported by their similar doped structures based on X-ray data later discussed. The lower P1 transition energies for the DDB-F_{72}-doped films relative to the F4TCNQ-doped films of the same regioregularity indicate that the DDB-F_{72} dopant reduces Coulombic binding between the polaronic holes on P3HT and DDB-F_{72}^{-} anions in both polymer types. This is a direct result of the size of the DDB-F_{72} dopant; with its ~2 nm diameter, DDB-F_{72} effectively separates polarons on the polymer backbone from the counterion charge of DDB-F_{72}^{-}.[9] The DDB-F_{72} dopant is therefore a good potential choice for doping RRa-P3HT, in which kinks in the polymer chain decrease polaron delocalization and increase the binding of charge carriers.

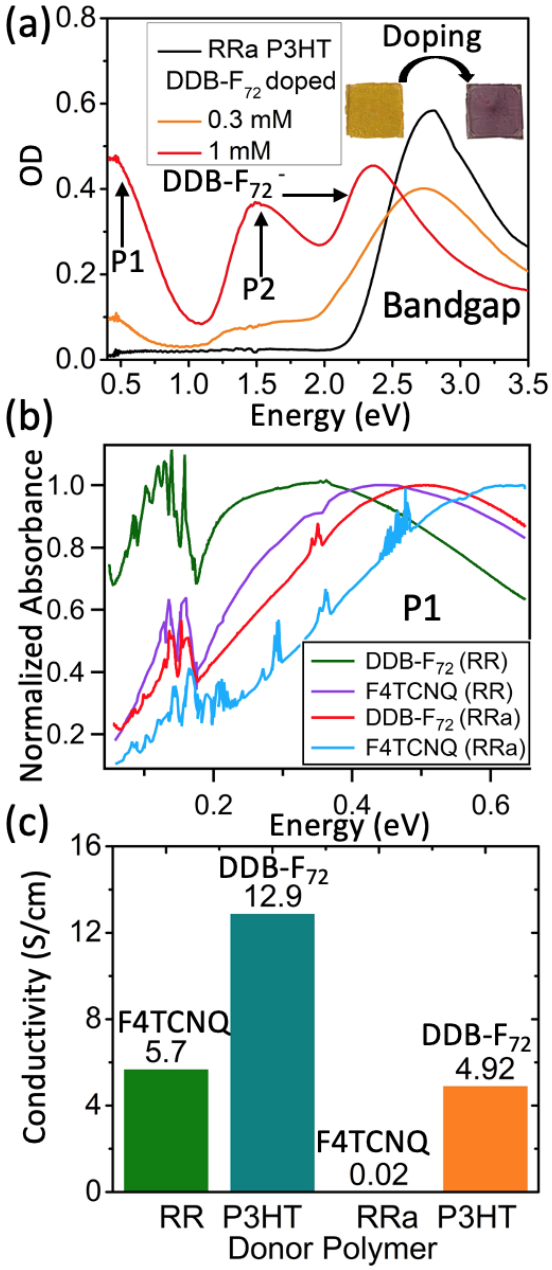

Figure 3.2: (a) UV-Vis-NIR absorbance spectra of RRa-P3HT doped with low and high concentrations of DDB-F_{72}. Doping is characterized by the bleaching of the P3HT neutral peak (~2.8 eV) corresponding to the bandgap transition and the appearance of polaron transitions in the red and near IR ranges (designated P1 & P2). (b) Normalized FT-IR spectra of the P1 transition of RR- and RRa-P3HT doped with DDB-F_{72} and F_4TCNQ. The position of the P1 transition has been shown to include a Coulombic binding energy term, where a lower energy P1 transition indicates reduced Coulombic binding. (c) Measured conductivities of RR- and RRa-P3HT doped with DDB-F_{72} and F_4TCNQ. For both polymers, DDB-F_{72} produced higher conductivities than F_4TCNQ.

While the DDB-F_{72} dopant has been shown to produce high conductivities in RR-P3HT,[15] conductivities from DDB-F_{72}-doped RRa-P3HT have not been previously reported. Figure 3.2c shows the conductivities of both RR- and RRa-P3HT films doped by sequential processing (SqP) with both F_4TCNQ and DDB-F_{72}. The conductivities of both RR- and RRa-P3HT films doped with DDB-F_{72} are higher than those doped with F_4TCNQ, in line with the reduced Coulombic binding spectroscopically observed with DDB-F72. Surprisingly, DDB-F_{72} improves the conductivity of RR-P3HT by only a factor of ~2× while RRa-P3HT conductivities with DDB-F_{72} are ~200× higher than those doped with F_4TCNQ. To explain this, we hope to show that this massive improvement in sample conductivity primarily reflects the ability of DDB-F_{72} to dope the amorphous regions of RRa-P3HT and therefore increase the fraction of the film used in conduction.

To identify whether the observed improvements in conductivity were due to increased carrier density or carrier mobility, we used AC-field Hall effect measurements to determine the density of mobile carriers (n_{Hall}) and their mobilities (μ_{H}). These values are summarized in Table 1.[9,24–26] Surprisingly, the hole mobilities of both RR- and RRa-P3HT doped with 1 mM DDB-F_{72} are nearly identical. The higher conductivity of the DDB-F_{72}-doped RR-P3HT therefore must result from its ~2.5× higher carrier density than for RRa-P3HT. This result is reasonable given that RRa-P3HT is several hundred mV harder to oxidize than RR-P3HT (Figure 3.1a). While the DDB-F_{72} dopant is able to produce high carrier mobilities from RRa-P3HT, it is ultimately limited in carrier production by its oxidizing potential relative to the low-lying valence band of RRa-P3HT.

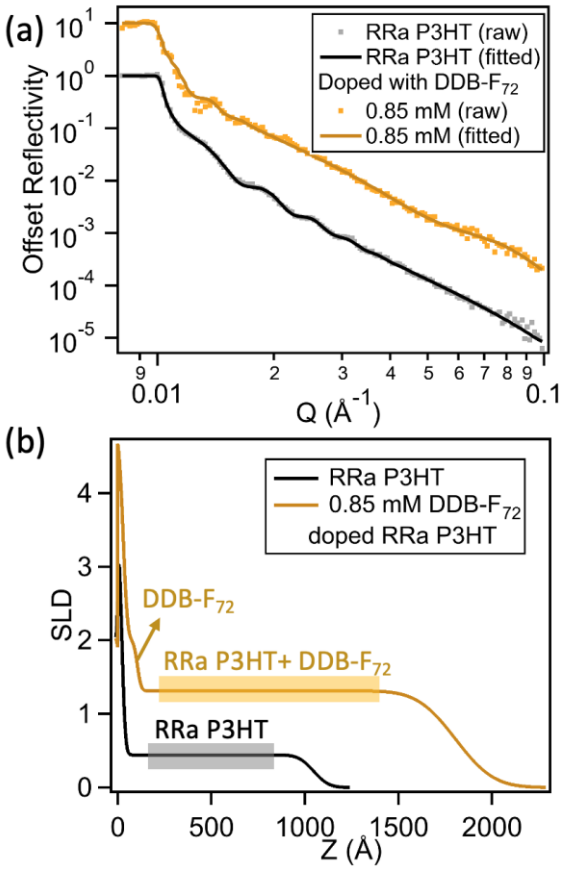

Figure 3.3: (a) Raw (dots) and fitted (solid line) neutron reflectometry (NR) spectra of undoped RRa-P3HT and DDB-F_{72}-doped RRa-P3HT. (b) SLD profiles of RRa-P3HT and DDB-F_{72}-doped RRa-P3HT. Though a slight buildup of DDB-F_{72} is visible near the substrate surface (Z = 0 Å), DDB-F_{72} distributes uniformly in the bulk of the RRa-P3HT film.

While the large size of the DDB-F_{72} dopant is good for reducing Coulombic binding forces, it is necessary to verify that the dopant can penetrate and dope the entirety of the polymer film volume. Neutron reflectometry (NR) measurements were performed on DDB-F_{72}-doped RR- and RRa-P3HT films to characterize the distribution of dopant molecules in the polymer films. The raw NR data and corresponding curves of fit are shown in Figure 3.3a. The reflectometry data were fit based on measured scattering length densities (SLDs) for RR-P3HT (measured at 0.56×10^{-2} Å^{-2}), RRa-P3HT (measured at 0.45×10^{-2} Å^{-2}), and DDB-F_{72} (calculated at 0.56×10^{-2} Å^{-2}) to determine the relative composition of polymer and dopant.[27,28] Figure 3.3b shows the fitted film

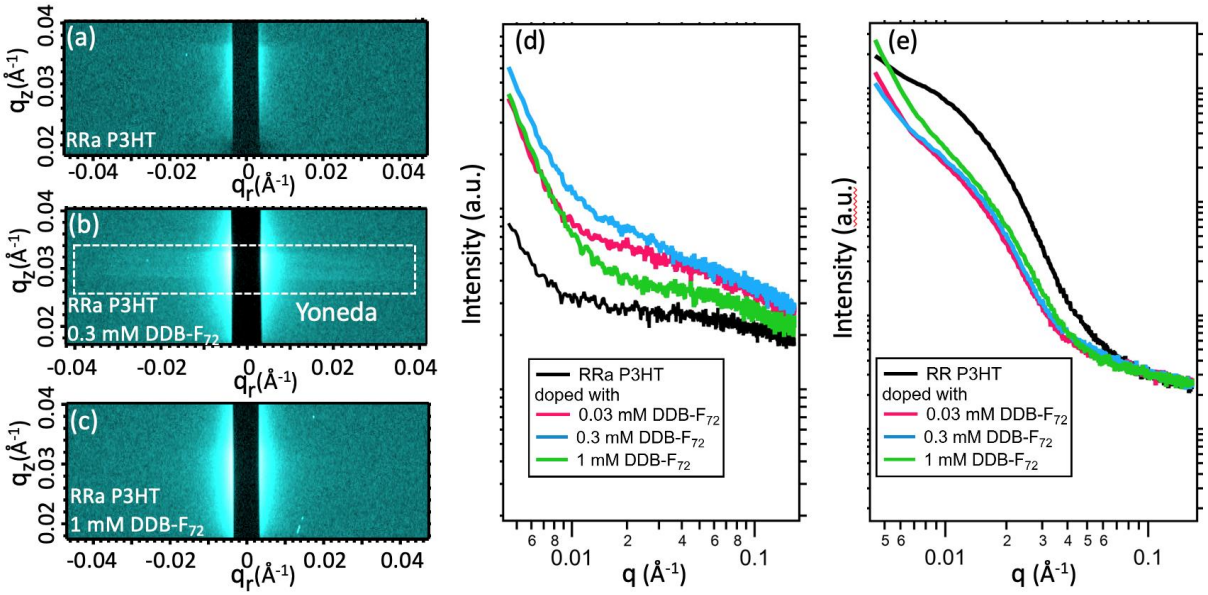

Figure 3.4: 2D GISAXS patterns of (a) RRa-P3HT, (b) RRa-P3HT doped with 0.3 mM DDB-F_{72}, and (c) RRa-P3HT doped with 1 mM DDB-F_{72}. Doping with low concentrations of DDB-F_{72} produced the horizontal Yoneda peak (boxed), indicating the introduction of electron density contrast at small length scales. Further doping is shown to erase the Yoneda peak, indicating the disappearance of electron density contrast. Integrated Yoneda regions for (d) RR- and (e) RRa-P3HT doped with DDB-F_{72}. DDB-F_{72}-doped RR-P3HT shows lower intensity and increased q-value of the scattering peak (q = 0.010-0.015 $Å^{-1}$) corresponding to a characteristic crystallite distance. In RRa-P3HT, DDB-F_{72} doping increases scattering greatly at low q-values and slightly at medium and high q-values. At high dopant concentrations, scattering intensity is reduced slightly due to a loss of domain contrast.

SLD as a function of distance from the substrate where Z = 0 is the substrate-film interface and the SLD approaches 0 near the film-air interface. While a slight buildup of DDB-F_{72} is observed near the substrate surface in the RRa-P3HT film, the higher bulk film SLD indicates that the DDB-F_{72} dopant is distributed throughout the film. The doped film is also shown to have swelled based on the higher distance Z at which the film SLD goes to zero, consistent with volume expansion due to dopant infiltration. Together, these results indicate that DDB-F_{72} is not diffusion-limited in its ability to dope.

Because the presence of dopant within the polymer film does not necessarily imply doping, doping efficiencies – the ratio of the number of carriers produced to the number of dopant

molecules present in the film – were calculated from the AC-field Hall and NR measurements to describe the utility of the infiltrated dopant molecules. Dopant number densities extracted from the DDB-F_{72}-doped film NR SLDs, and carrier densities for the films were calculated from AC-field Hall effect measurements using the same method as in our previous study[14] (described in the SI). These values were combined to calculated doping efficiencies for DDB-F_{72}-doped RR- and RRa-P3HT. Table 1 shows the calculated doping efficiencies are 96% and 77% for RR- and RRa-P3HT, respectively. The extremely high doping efficiency for DDB-F_{72}-doped RR-P3HT is consistent with previously values. Because the doping efficiencies were calculated at identical dopant concentrations for RR- and RRa-P3HT, the lower doping efficiency for RRa-P3HT may be partially due to its lower valence band (Figure 3.1), reducing the oxidizing potential of the RRa-P3HT and DDB-F_{72} couple. In both RR- and RRa-P3HT, high doping efficiencies indicate that most of the DDB-F_{72} molecules detected within the polymer films have contributed carriers to the film, reinforcing the role of reducing dopant-polaron Coulombic binding in shifting the doping equilibrium towards charge transfer.

While low Coulombic binding between DDB-F_{72} and generated polarons provides a partial explanation for the high carrier mobility in doped RRa-P3HT, it is surprising that the carrier mobility of an initially amorphous polymer like RRa-P3HT is finally similar to that of semicrystalline RR-P3HT when doped. Because carrier mobility is closely linked with film structure, an explanation may lie in structural similarities between the doped RR- and RRa-P3HT films. To investigate this, a combination of GISAXS and GIWAXS techniques were employed to probe the structural changes that occur during doping with DDB-F_{72}.

First, changes in the crystallite-scale structure of DDB-F_{72}-doped RR- and RRa-P3HT films were observed through GISAXS studies. 2D GISAXS patterns, zoomed in to emphasize the

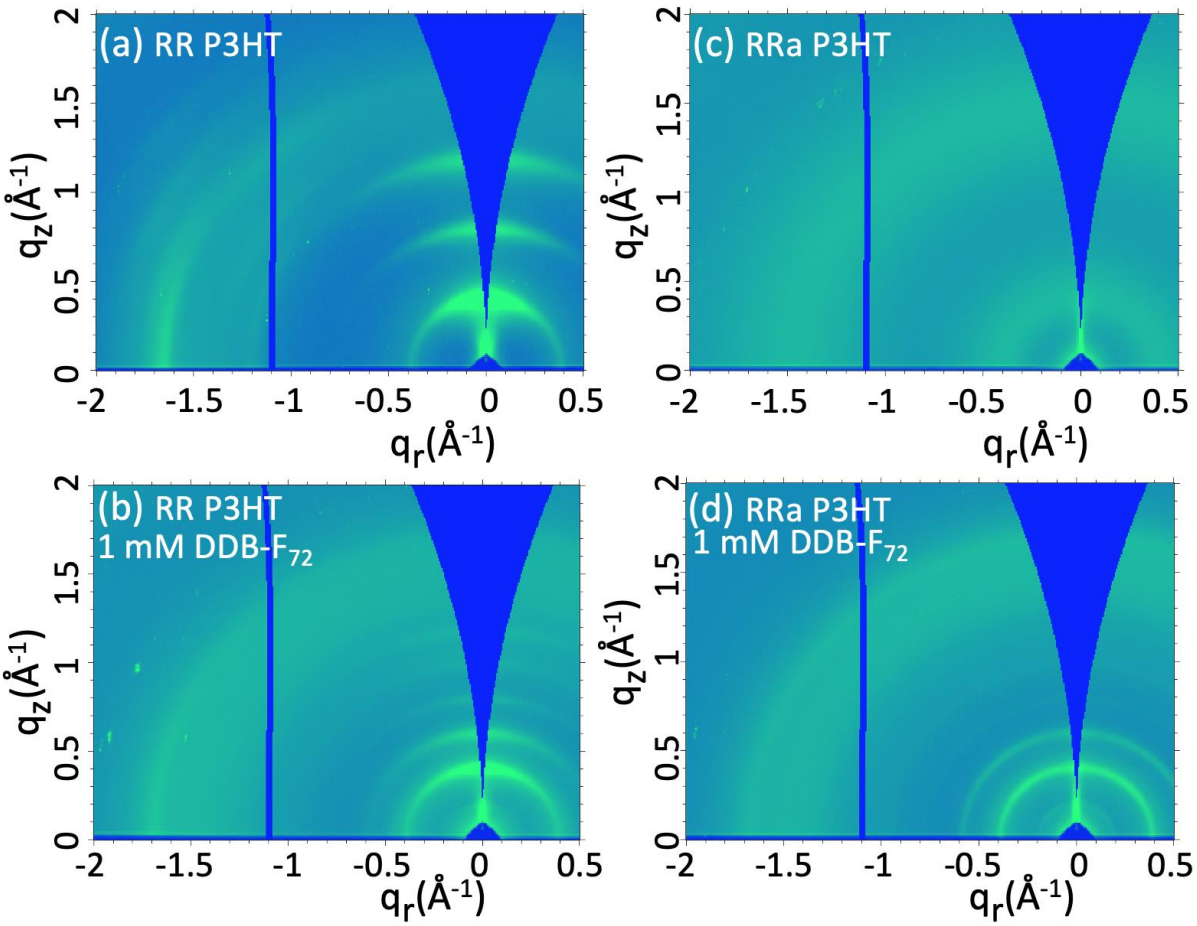

Figure 3.5: 2D GIWAXS patterns of (a) RR-P3HT, (b) RR-P3HT doped with 1 mM DDB-F_{72}, (c) RRa-P3HT, and (d) RRa-P3HT doped with 1 mM DDB-F_{72}. Doping with DDB-F_{72} is shown to induce crystallinity in RRa-P3HT polymer film, producing an identical crystalline structure in both RR and RRa-P3HT.

Yoneda peak region, are shown in Figures 3.4a-c. The Yoneda peak is a horizontal scattering peak produced by enhanced X-ray scattering near the angle of internal reflection at the polymer-air interface that contains information on the lateral electron density contrast in the thin film.[29] Horizontal integration of the Yoneda peak region of undoped and DDB-F_{72}-doped RRa-P3HT (Figure 3.4d) shows a large increase in scattering in the low *q*-value (large correlation distance, *d*) region caused by the nucleation and growth of large crystallites that scatter X-rays at the crystallite-amorphous interface. Scattering at medium and high q-values also increases slightly, suggesting a

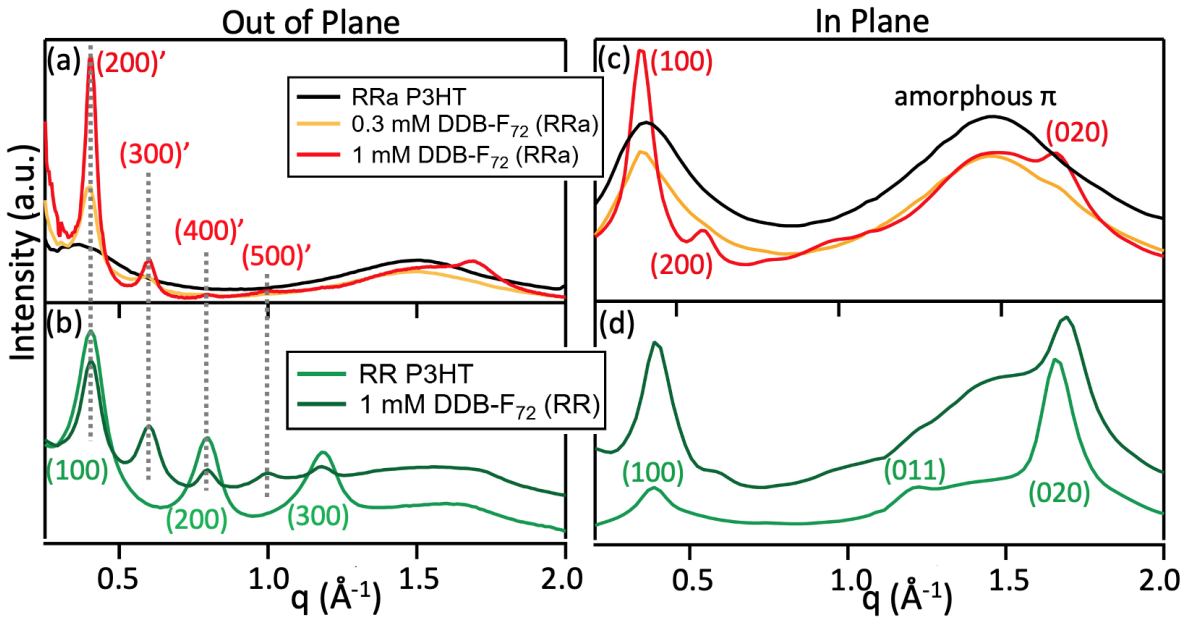

Figure 3.6: Radially integrated out-of-plane (perpendicular to substrate) and in-plane (parallel to substrate) 1D GIWAXS patterns for (a,c) RRa-P3HT and (b,d) RR-P3HT doped with DDB-F_{72}. Doped RR and RRa-P3HT show identical lamellar diffraction peak positions, indicating identical crystalline structures within the doping-induced crystalline regions of RRa-P3HT and the doped crystalline regions of RR-P3HT.

range of nucleated crystallite sizes. At high doping levels (1 mM DDB-F_{72}), scattering at low q-values decreases slightly due to a loss of domain contrast as the film further crystallizes.

The integrated Yoneda peak for undoped RR-P3HT (Figure 3.4e) contains a peak at ~0.01 $Å^{-1}$ (d ~ 60 nm). Upon dopant intercalation, this peak shifts to a larger q-value (q ~ 0.015 $Å^{-1}$; d ~ 42 nm) and decreases in scattering intensity. Previous work with the DDB-F_{72} dopant shows that the large molecule intercalates into the lamellar stacks of P3HT. The shift of the observed peak to larger q-value (smaller d) is believed to indicate the breaking up of existing crystallites into smaller regions of varying size due to the strain of dopant intercalation. At high doping levels (1 mM DDB-F_{72}), an increase in low q-value scattering is observed. Based on the appearance of crystalline regions in RRa-P3HT during doping, the DDB-F_{72} dopant is believed capable of converting amorphous P3HT to crystallites. This increase in low q-value scattering is therefore believed to

correlate with the expansion of crystallites into the surrounding amorphous regions, producing larger crystallites than present at low dopant concentrations.

Next, GIWAXS studies were performed to observe intra-crystallite differences in structure. Figures 3.5a-d show 2D GIWAXS patterns for undoped and DDB-F_{72}-doped RR- and RRa-P3HT and corresponding 1D patterns produced by radial integration near the q_r- and q_z-axes ("in-plane" and "out-of-plane" directions, respectively) are plotted in Figure 3.6. As is well-known, undoped RR-P3HT (Figure 3.5a) is "edge-on" oriented, with the alkyl side chains of the polymer crystallites stacking normal to the substrate surface and the polymer backbone and π-stacks lying in the plane of the substrate. The layers of polymer backbone separated by the side chain produce out-of-plane scattering peaks at multiples of $q_z \sim 0.4$ Å^{-1}, corresponding to a *d*-spacing of ~16 Å, which we refer to as the lamellar spacing, d_{lam}. The π-stacking of the thiophene rings produce scattering peaks in the plane of the substrate at $q_r \sim 1.65$ Å^{-1}, corresponding to a *d*-spacing of ~3.81 Å, which we refer to as d_π).[27] The broad peak centered at $q_r \sim 1.5$ Å^{-1} was confirmed by molecular modeling to correspond to disordered π-stacking distances caused by poor thiophene ring alignment (Figure S4). In contrast, undoped RRa-P3HT (Figure 3.5c) shows isotropic scattering rings corresponding to the lamellar spacing (i.e., alkyl side chain spacing, *q* centered at ~0.4 Å^{-1}; $d_{lam} \sim 16$ Å) and amorphous π-stacking distance (*q* centered at ~ 1.5 Å^{-1}; $d_\pi \sim 4.19$ Å), indicating a lack of specific crystallite orientation relative to the substrate. The broadness of the isotropic rings and the larger π-stacking distance of RRa-P3HT both suggest a high level of disorder in the polymer chain packing, as expected for a highly amorphous material.[11]

Upon doping RR-P3HT with DDB-F_{72} (Figure 3.5b), the lamellar distance doubles (scattering peaks at multiples of $q_z \sim 0.2$ Å^{-1}; $d_{lam} \sim 31$ Å) to accommodate the intercalation of the very large DDB cluster into the alkyl side chain region,[14] while the π-stacking distance ($q_r \sim 1.70$

$Å^{-1}$; d_π ~ 3.70 Å) becomes slightly contracted. Surprisingly, doping of RRa-P3HT with DDB-F_{72} produces a set of dopant-intercalated lamellar and π-stacking peaks (Figures 3.6a,b) that are identical to those of doped RR-P3HT. This indicates that ordered crystallites emerge from the amorphous RRa polymer upon doping, with a doped crystal structure that is the same as in doped RR-P3HT. The presence of higher-order lamellar overtones and sharper integrated 1D spectrum peaks for doped RRa-P3HT compared to RR-P3HT (Figure 3.6) indicate a higher level of paracrystalline order that supports the presence of large doping-induced crystallites in the RRa-P3HT polymer, as determined by GISAXS. The more isotropic (i.e., ring-like) lamellar peaks observed in doped RRa-P3HT (Figure 3.5d) are consistent with crystallites that nucleated in the bulk of the polymer film away from the lattice templating effects of the substrate.

Table 1. Electronic Properties of DDB-F_{72}-Doped RR- and RRa-P3HT[a]

Polymer	Polymer SLD[b] [$Å^{-2}$]	Dopant Density[b] [cm^{-3}]	μ_h[c] [$cm^2V^{-1}S^{-1}$]	σ[c] [$S\,cm^{-1}$]	n_{Hall}[c] [cm^{-3}]	Doping Efficiency[d] [%]
RRa-P3HT	0.45×10^{-2}	2.47×10^{20}	0.098	3.0	1.91×10^{20}	77
RR-P3HT	0.56×10^{-2}	5.3×10^{20}	0.084	6.8	5.08×10^{20}	96

[a] Calculations are detailed in the SI.
[b] Calculated from fitted NR measurements.
[c] Calculated from AC-field Hall Effect measurements.
[d] Estimated by comparing the obtained dopant density and carrier density values.

3.4 Summary

Here, we have demonstrated an effective strategy for the doping of RRa-P3HT. The dodecaborane (DDB) cluster-based large molecular dopant DDB-F_{72} was shown to dope RRa-P3HT with a 77% doping efficiency and to nucleate P3HT crystallites in the process. The doped RRa-P3HT film had a conductivity value of 4.9 S/cm, 200× higher than the conductivity of

F_4TCNQ-doped RRa-P3HT previously reported and comparable to that of DDB-F_{72}-doped RR-P3HT. Despite RRa-P3HT films starting in a highly amorphous state, structural comparisons of DDB-F_{72}-doped RR- and RRa-P3HT revealed close similarities in crystalline structure and in the extent of film crystallinity that translated into similar hole mobilities for both polymer regioregularities. Through careful selection of a compatible dopant that reduces Coulombic binding of polarons and induces crystallite formation, we have shown that initially amorphous semiconducting polymers can be made to have similar carrier mobilities to semicrystalline polymers.

3.5 Supporting Information

S1 Conductivity Measurements

Devices, RRa P3HT doped with 1 mM DDB-F_{72} on 1.5 cm × 1.5 cm glass substrates fabricated through sequential processing (SqP), were used to characterize the electrical conductivity of the polymer films. Conductivities measured can be seen in Table S1.

Table S1. Van der Pauw conductivity measurements of 1 mM DDB-F_{72} doped RRa P3HT films

Sample #	R□ $_{avg}$ (Ω/□)	Thickness $_{avg}$ (nm)	Conductivity(S/cm)
1	8178	236 ± 24	4.6 ± 0.5
2	10178	204 ± 17	4.8 ± 0.4
3	8538	219 ± 8	5.3 ± 0.2

The conductivity measurements were obtained from sheet resistance ($R_{\square}$ *or R square*) and film thickness (t). To measure $R_{\square}$, the Van der Pauw technique was used; probes were placed at each of the four corners of a square sample, with current flowing along one side (two probes

sharing an edge) and the voltage being measured across the opposite edge. Then, the measurement is repeated after rotating the contacts 90°. The in-home set-up uses Labview to fit the resistance values from the slope of the I-V curved to the Van der Pauw equation

$$(e^{(-\frac{\pi R_A}{R_\square})} + e^{(-\frac{\pi R_B}{R_\square})} = 1) \qquad (1)$$

to obtain $R_\square$. The second value, thickness, was obtained by profilometry (Dektak 150 stylus profilometer). At least three values on different locations of the film were used to report an average value. All reported values from Table S1 were results of multiple samples averaged and error propagated to conductivity.

S2 Neutron Reflectometry (NR) & Doping Efficiency Calculation

The active layer scattering length density (SLD) is the average of the SLD of all of the components. Since the SLD for the active layer and the components are known either by measurement or calculation, the SLD fraction can be calculated as shown in Table S2.

Table S2. NR calculation for DDB-F_{72} doped RRa P3HT

	Active Layer (AL)	RRa P3HT in AL	DDB-F_{72} in AL
SLD	1.36 (Measured)	0.45 (Measured)	2.0 (Calculated)
SLD Fraction	1	0.41	0.59
Monomer Ratio	N/A	7	1

P3HT has 25 atoms per monomer, DDB-F_{72} has 264 atoms per molecule. Using the SLD fraction, we can calculate the ratio of DDB-F_{72}:RRa P3HT monomer is 1:734 (1:7).

Dopant density in Table 1 is calculated based on the RRa P3HT monomer: DDB-F_{72} molecule ratio. We can calculate the number of RRa P3HT monomers in the pristine polymer film using RRa P3HT film density, film thickness, film area. The number of the RRa P3HT monomers

is constant during the doping process, thus the number of DDB-F_{72} molecules (dopant density) can be calculated using the previous calculated dopant:monomer ratio.

Hole mobilities (μ_h) are directly measured from the AC Hall measurement. The DDB-F_{72} concentration used in the AC-Hall measurement is 1 mM. The dopant concentration used in NR is 0.85 mM since higher dopant concentration makes the film too rough to get a reasonable fitting. If we assume the mobile carrier mobility measured by AC Hall is the same as in NR, we can use μ_h and conductivities (σ) measured using the same sample sets as NR to calculate the hole densities (n_{Hall}) using the following equation;

$$doping\ efficiency = \frac{n_{Hall}}{dopant\ density} \qquad (2)$$

S3 GIWAXS for P3HT films doped with DDB-F_{72}

2-D GIWAXS for DDB-F_{72} doped RR P3HT with more concentrations can be found in the supporting information in the previous work.[14] Below are the 2-D GIWAXS for DDB-F_{72} doped RRa P3HT and RR P3HT for this work..

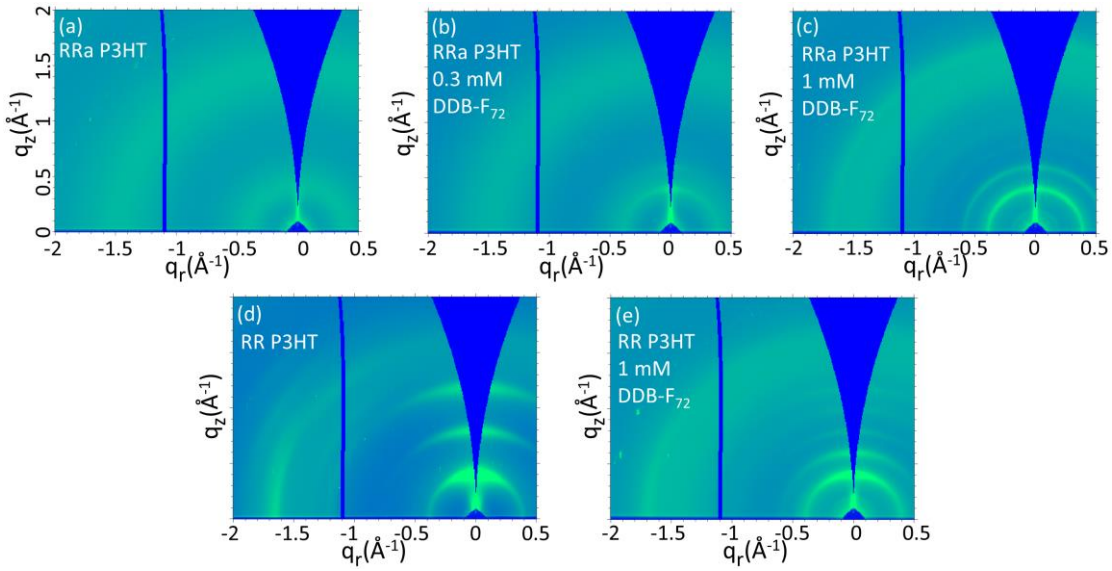

Figure S1: 2-D GIWAXS for (a) RRa P3HT, (b) RRa P3HT doped with 0.3 mM DDB-F_{72}, (c) RRa P3HT doped with 1 mM DDB-F_{72}, (d) RR P3HT and (e) RR P3HT doped with 1 mM DDB-F_{72}. For the amorphous RRa P3HT, crystalline structures start to form at 0.3 mM DDB-F_{72} doping level as shown by the appearance of lamellar overtones. Doping with DDB-F_{72} is shown to induce crystallinity in RRa P3HT polymer film, producing a similar crystalline structure in both RR and RRa P3HT at 1 mM dopant concentration.

S4 Crystallinity change of F4TCNQ and DDB-F_{72} doped RRa P3HT

Table S3. Crystallinity change of DDB-F_{72} and F_4TCNQ doped RRa P3HT

Normalized to (100)	RRa P3HT	F_4TCNQ (4 mM)	F_4TCNQ (2 mM)	F_4TCNQ (1 mM)	F_4TCNQ (0.02 mM)	DDB-F_{72} (1 mM)
Peak Area	1	1.66	0.75	~ 0.54	0.28	0.65

The above table summarizes the crystallinity changes of RRa P3HT doped with F_4TCNQ and DDB-F_{72}. The crystallinity is estimated by integrating the (100) peak area along the full chi distribution due to the untextured structure of RRa P3HT. The integrated peak area is normalized to the pristine RRa P3HT by taking the ratio of the integration of doped RRa P3HT (100) peak area over pristine RRa P3HT (100) peak area. All the datapoints are published data,[31,32] except the 1 mM F_4TCNQ datapoint is estimated by fitting a linear trend line over other F4TCNQ concentration data.

Table S3 indicates that F_4TCNQ and DDB-F_{72} doping induce similar crystallinity in RRa P3HT. This shows that the reduced Coulombic binding of polarons from the DDB dopant counterions in amorphous polymer regions is the key to the improved conductivity seen in the DDB-F_{72} case.

S5 GISAXS for DDB-F_{72} doped P3HT

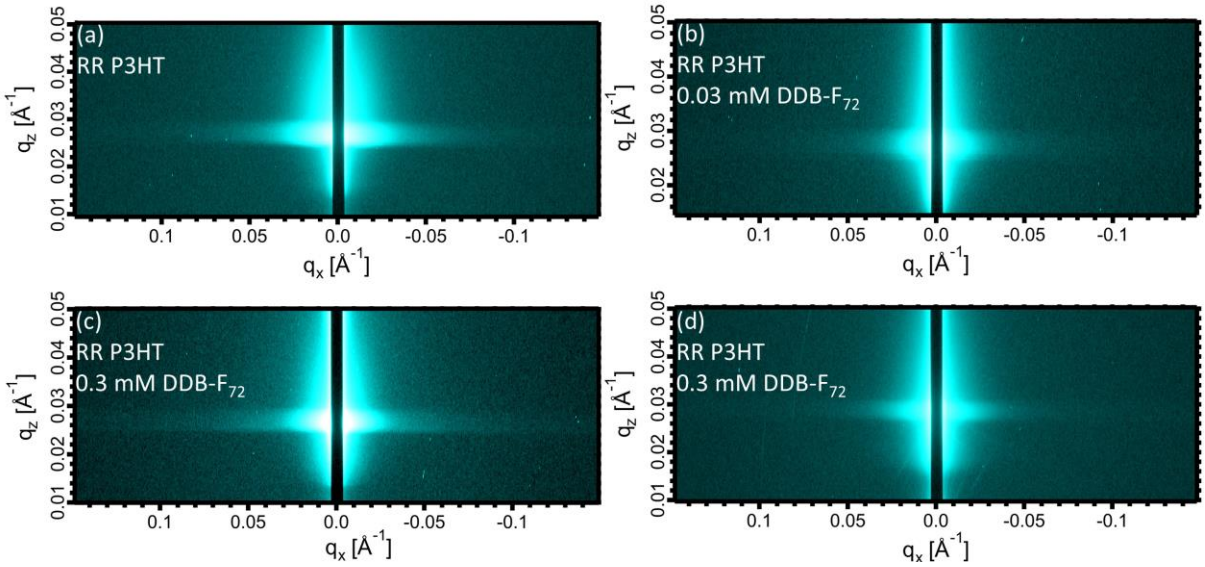

Figure S2: 2-D GISAXS for (a) RR P3HT, (b) RR P3HT doped with 0.03 mM DDB-F_{72}, (c) RR P3HT doped with 0.3 mM DDB-F_{72} and, (d) RR P3HT doped with 1 mM DDB-F_{72}.

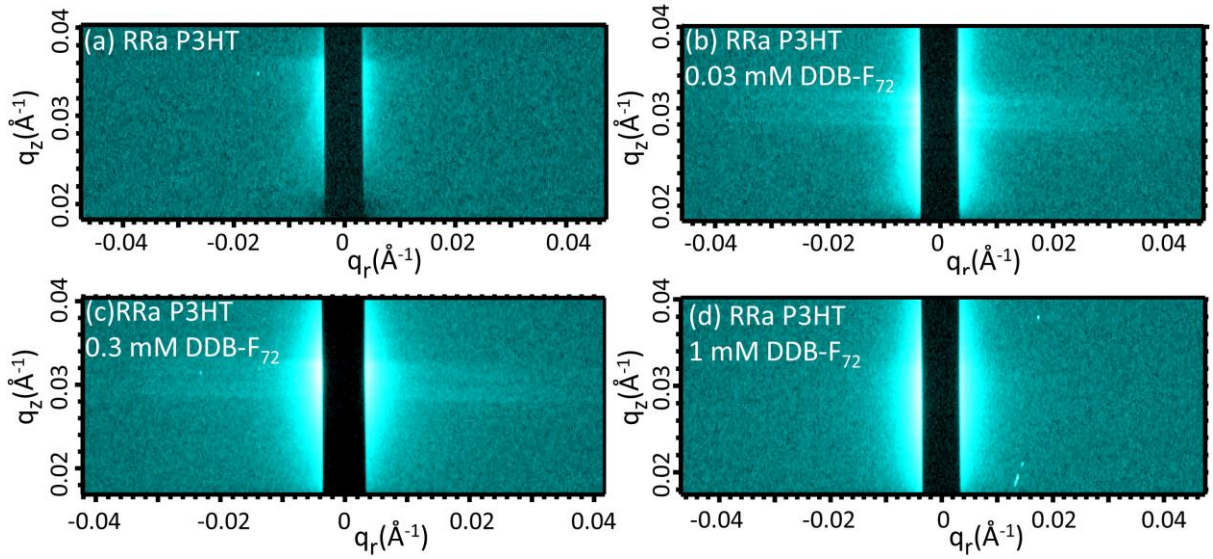

Figure S3: 2-D GISAXS for (a) RRa P3HT, (b) RRa P3HT doped with 0.03 mM DDB-F_{72}, (c) RRa P3HT doped with 0.3 mM DDB-F_{72}, and (d) RRa P3HT doped with 1 mM DDB-F_{72}.

S6 Simulation for RR and RRa P3HT

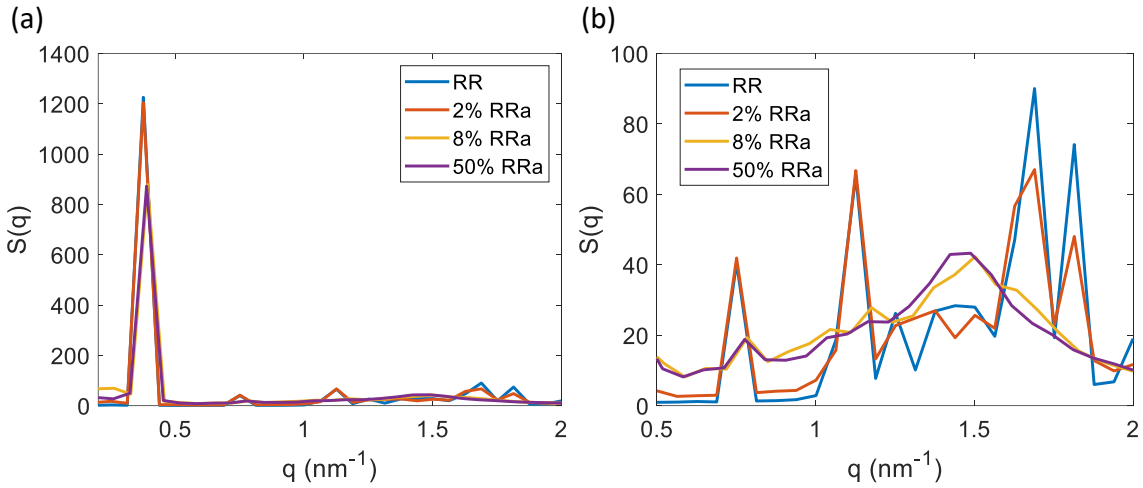

Figure S4: Calculated structure factor for RRa P3HT. The percent RRa indicates the percentage of thiophene units that are flipped, i.e. for 50% RRa, half of the thiophene units are randomly flipped. (b) shows the broad peak at 1.5 q

Simulation Methods

MD simulations and calculations were carried out using the GROMACS package.[8-11] DFT calculations were carried out using Gaussian[12] with PBE0-D3/6-31G(d,p). The parameters for the forcefield and the charges are listed below. The parameters for the monomers whose thiophene units are flipped are not changed. Identical dihedral angle potential for the inter-thiophene bond are used for all monomers. All the simulations were carried out with periodic boundary conditions in all three axes in the isothermal-isobaric (NPT) ensemble using the Berendsen thermostat with $\tau_p = 5.0$ ps. The pressure is set at 250 bar, respectively, to match the experimental density of pure P3HT films. A timestep of 1 fs and a leap-frog integration algorithm were used. Electrostatics were treated using the Fast smooth Particle-Mesh Ewald (SPME) with cutoff at 1.4 nm, Fourier spacing of 0.12 nm, and PME order of 4. The van der Waals cutoff was set at 1.4 nm. For thermodynamic integration, a soft-function with $\sigma = 0.3$ and $\alpha = 0.5$ is used for lambda. An example mdp file, which sets all the MD parameters, is also included. Each system is annealed

starting at 500 K at 2.5 ns, then at 400 K at 2.5 ns. Finally, at 300 K for 5 ns. The structure factors are calculated using the last ns of the trajectory. Structure factor is calculated using GROMACS's build-in function which uses an FFT algorithm.

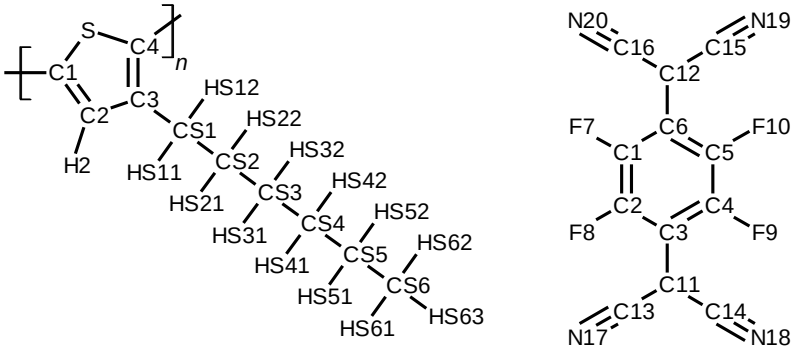

Scheme S1 Atom labels for the forcefield parameters

Table S4 LJ parameters

	σ (nm)	ϵ (kJ mol^{-1})
P3HT		
S	0.360	0.355
C1, C2, C3, C4	0.355	0.355
H2	0.242	0.242
CS1, CS2, CS3, CS4, CS5, CS6	0.350	0.350
HS11, HS12, HS21, HS22, HS31, HS32, HS41, HS42, HS51, HS52, HS61, HS62, HS63	0.250	0.250

Table S5 Bond Parameters

	b_0 (nm)	k_b (kJ mol^{-1} nm^{-2})
P3HT		
S-C1	0.1743	0.1734
S-C4	$0.1_{72}5$	0.1734
C1-C2	0.1367	0.1374
C1-C4	0.1458	0.1450
C2-C3	0.1430	0.1433
C2-H2	0.1084	0.1082
C3-C4	0.1374	0.1374
C3-CS1	0.1501	0.1509
CS1-HS11, CS1-HS12	0.1092	0.1098
CS1-CS2, CS2-CS3, CS3-CS4, CS4-CS5, CS5-CS6	0.1529	0.1542
CS2-HS21, CS2-HS22, CS3-HS31, CS3-HS32, CS4-HS41, CS4-HS42, CS5-HS51, CS5-HS52, CS6-HS61, CS6-HS62, CS6-HS63	0.1090	0.1095

Table S6 Angle Parameters

	θ_0 (deg)	k_θ (kJ mol^{-1} rad^{-2})
P3HT		
C1-S-C4	91.6	92.77
S-C1-C2	110.3	110.3
S-C4-C3	111.2	110.3
S-C1-C4	120.4	119.6
C2-C1-C4	128.4	130.1
C3-C2-H2	123.3	123.7
C1-C2-C3	114.0	113.3
C2-C3-C4	111.8	113.3
C1-C2-H2	122.6	123.0
C2-C3-CS1	122.8	123.4
C4-C3-CS1	125.4	124.5
C3-CS1-HS11, C3-CS1-HS12	111.3	109.2
C3-CS1-CS2	115.6	115.4
CS1-CS2-CS3, CS2-CS3-CS4, CS3-CS4-CS5, CS4-CS5-CS6	112.7	112.7
HS11-CS1-HS12	108.6	107.8
HS21-CS2-HS22, HS31-CS3-HS32, HS41-CS4-HS42, HS51-CS5-HS52, HS61-CS6-HS62, HS61-CS6-HS63, HS62-CS6-HS63	107.8	107.8
HS11-CS1-CS2, HS12-CS1-CS2, CS1-CS2-HS21, CS1-CS2-HS22, HS21-CS2-CS3, HS22-CS2-CS3, CS2-CS3-HS31, CS2-CS3-HS32, HS31-CS3-CS4, HS32-CS3-CS4, CS3-CS4-HS41, CS3-CS4-HS42, HS41-CS4-CS5, HS42-CS4-CS5, CS4-CS5-HS51, CS4-CS5-HS52, HS51-CS5-CS6, HS52-CS5-CS6, CS5-CS6-HS61, CS5-CS6-HS62, CS5-CS6-HS63	110.7	110.7

Table S7 Dihedral Parameters

(kJ mol^{-1})	C0	C1	C2	C3	C4
C2-C1-S-C4, S-C1-C2-H2, S-C1-C2-C3, C1-S-C4-C3, C1-S-C4-C1, C1-C2-C3-CS1, C1-C2-C3-C4, H2-C2-C3-CS1, H2-C2-C3-C4, C2-C3-C4-S, C2-C3-C4-C1, CS1-C3-C4-S, CS1-C3-C4-C1, C4-C1-S-C4, C4-C1-C2-H2, C4-C1-C2-C3	30.33	0	–30.33	0	0
C2-C3-CS1-HS11, C2-C3-CS1-HS12, C2-C3-CS1-CS2, C4-C3-CS1-HS11, C4-C3-CS1-HS12, C4-C3-CS1-CS2	0	0	0	0	0
C3-CS1-CS2-HS21, C3-CS1-CS2-HS22	0.9665	2.900	0	–3.866	0
C3-CS1-CS2-CS3	2.929	–1.464	0.2092	–1.674	0
HS11-CS1-CS2-HS21, HS11-CS1-CS2-HS22, HS11-CS1-CS2-CS3, HS12-CS1-CS2-HS21, HS12-CS1-CS2-HS22, HS12-CS1-CS2-CS3, CS1-CS2-CS3-HS31, CS1-CS2-CS3-HS32, CS1-CS2-CS3-CS4, HS21-CS2-CS3-HS31, HS21-CS2-CS3-HS32, HS21-CS2-CS3-CS4, HS22-CS2-CS3-HS31, HS22-CS2-CS3-HS32, HS22-CS2-CS3-CS4, CS2-CS3-CS4-HS41, CS2-CS3-CS4-HS42, CS2-CS3-CS4-CS5, HS31-CS3-CS4-HS41, HS31-CS3-CS4-HS42, HS31-CS3-CS4-CS5, HS32-CS3-CS4-HS41, HS32-CS3-CS4-HS42, HS32-CS3-CS4-CS5, CS3-CS4-CS5-HS51, CS3-CS4-CS5-HS52, CS3-CS4-CS5-CS6, HS41-CS4-CS5-HS51, HS41-CS4-CS5-HS52, HS41-CS4-CS5-CS6, HS42-CS4-CS5-HS51, HS42-CS4-CS5-HS52, HS42-CS4-CS5-CS6, CS4-CS5-CS6-HS61, CS4-CS5-CS6-HS62, CS4-CS5-CS6-HS62, HS51-CS5-CS6-HS61, HS51-CS5-CS6-HS62, HS51-CS5-CS6-HS63, HS52-CS5-CS6-HS61, HS52-CS5-CS6-HS62, HS52-CS5-CS6-HS63	0.6276	1.883	0	–2.510	0
S-C4-C1-S, C3-C4-C1-C2	0.4377	–0.3997	–3.027	1.712	–0.8584
S-C4-C1-C2, C3-C4-C1-S	0.4377	0.3997	–3.027	–1.712	–0.8584
C4-C3-S-C1 (improper)	180	4.602	–	–	–

Table S8 Partial Charges

	q
P3HT	FF1
S	–0.011
C1	0.118
C2	–0.260
H2	0.155
C3	0.078
C4	–0.118
CS1	–0.114
HS11, HS12	0.053
CS2	0.074
HS21, HS22	–0.005
CS3	–0.036
HS31, HS32	0.002
CS4	–0.014
HS41, HS42	0.002
CS5	0.1_{72}
HS51, HS52	–0.031
CS6	–0.215
HS61, HS62, HS63	0.043

Below is the mdp file used for the calculation.

```
title            =  cpeptid position restraining
cpp              =  /usr/bin/cpp
constraints      =  none
integrator       =  md
dt               =  0.001    ; ps !
nsteps           =  10000000     ; total 1.0 ps.
nstcomm          =  100
nstxout          =  10000
nstvout          =  10000
nstfout          =  0
nstlog           =  100
nstenergy        =  100
nstlist          =  100
ns_type          =  grid
rlist            =  1.0
coulombtype      = PME
vdwtype          = cut-off
rcoulomb         =  1.0
rvdw             =  1.0
fourierspacing   = 0.12
fourier_nx       = 0
fourier_ny       = 0
fourier_nz       = 0
pme_order        = 4
ewald_rtol       = 1e-5
optimize_fft     = yes
pbc              = xyz
periodic-molecules  = yes
; Berendsen temperature coupling is on
Tcoupl = v-rescale
tau_t = 0.1
tc-grps  =system
ref_t =   300
; Pressure coupling is  on
Pcoupl           = berendsen
pcoupltype       = isotropic
; Pcoupl           =  no
tau_p            =  5.0
compressibility  =  4.5e-5
ref_p            =  250.0
; Generate velocites is on at 300 K.
gen_vel          =  yes
gen_temp         =  500.0
; Anneal
annealing        =  single
annealing-npoints   =  3
annealing-time   =  0 2500 5000
annealing-temp   =  500 400 300
```

3.6 References

(1) Wang, Y.; Zhu, C.; Pfattner, R.; Yan, H.; Jin, L.; Chen, S.; Molina-Lopez, F.; Lissel, F.; Liu, J.; Rabiah, N. I.; et al. A Highly Stretchable, Transparent, and Conductive Polymer. *Sci. Adv.* **2017**, *3* (3), 1–11.

(2) Lim, E.; Peterson, K. A.; Su, G. M.; Chabinyc, M. L. Thermoelectric Properties of Poly(3-Hexylthiophene) (P3HT) Doped with 2,3,5,6-Tetrafluoro-7,7,8,8-Tetracyanoquinodimethane (F4TCNQ) by Vapor-Phase Infiltration. *Chem. Mater.* **2018**, *30* (3), 998–1010.

(3) Zhong, W.; Fan, B.; Cui, J.; Ying, L.; Liu, F.; Peng, J.; Huang, F.; Cao, Y.; Bazan, G. C. Regioisomeric Non-Fullerene Acceptors Containing Fluorobenzo[c][1,2,5]Thiadiazole Unit for Polymer Solar Cells. *ACS Appl. Mater. Interfaces* **2017**, *9* (42), 37087–37093.

(4) Salzmann, I.; Heimel, G.; Oehzelt, M.; Winkler, S.; Koch, N. Molecular Electrical Doping of Organic Semiconductors: Fundamental Mechanisms and Emerging Dopant Design Rules. *Acc. Chem. Res.* **2016**, *49* (3), 370–378.

(5) Ghosh, R.; Chew, A. R.; Onorato, J.; Pakhnyuk, V.; Luscombe, C. K.; Salleo, A.; Spano, F. C. Spectral Signatures and Spatial Coherence of Bound and Unbound Polarons in P3HT Films: Theory Versus Experiment. *J. Phys. Chem. C* **2018**, *122* (31), 18048–18060.

(6) Ghosh, R.; Luscombe, C. K.; Hambsch, M.; Mannsfeld, S. C. B.; Salleo, A.; Spano, F. C. Anisotropic Polaron Delocalization in Conjugated Homopolymers and Donor–Acceptor Copolymers. *Chem. Mater.* **2019**, acs.chemmater.9b01704.

(7) Qarai, M. B.; Ghosh, R.; Spano, F. C. Understanding Bipolarons in Conjugated Polymers Using a Multiparticle Holstein Approach. *J. Phys. Chem. C* **2021**, *125* (44), 24487–24497.

(8) Scholes, D. T.; Yee, P. Y.; Lindemuth, J. R.; Kang, H.; Onorato, J.; Ghosh, R.; Luscombe, C. K.; Spano, F. C.; Tolbert, S. H.; Schwartz, B. J. The Effects of Crystallinity on Charge Transport and the Structure of Sequentially Processed F4TCNQ-Doped Conjugated Polymer Films. *Adv. Funct. Mater.* **2017**, *27* (44), 1–13.

(9) Aubry, T. J.; Axtell, J. C.; Basile, V. M.; Winchell, K. J.; Lindemuth, J. R.; Porter, T. M.; Liu, J. Y.; Alexandrova, A. N.; Kubiak, C. P.; Tolbert, S. H.; et al. Dodecaborane-Based Dopants Designed to Shield Anion Electrostatics Lead to Increased Carrier Mobility in a Doped Conjugated Polymer. *Adv. Mater.* **2019**, *31* (11).

(10) Pingel, P.; Zhu, L.; Park, K. S.; Vogel, J. O.; Janietz, S.; Kim, E. G.; Rabe, J. P.; Brédas, J. L.; Koch, N. Charge-Transfer Localization in Molecularly Doped Thiophene-Based Donor Polymers. *J. Phys. Chem. Lett.* **2010**, *1* (13), 2037–2041.

(11) Noriega, R.; Rivnay, J.; Vandewal, K.; Koch, F. P. V; Stingelin, N.; Smith, P.; Toney, M. F.; Salleo, A. A General Relationship between Disorder, Aggregation and Charge Transport in Conjugated Polymers. *Nat. Mater.* **2013**, *12* (11), 1038–1044.

(12) Lim, E.; Glaudell, A. M.; Miller, R.; Chabinyc, M. L. The Role of Ordering on the Thermoelectric Properties of Blends of Regioregular and Regiorandom Poly(3-

hexylthiophene). *Adv. Electron. Mater.* **2019**, *1800915*, 1800915.

(13) Stanfield, D. A.; Wu, Y.; Tolbert, S. H.; Schwartz, B. J. Controlling the Formation of Charge Transfer Complexes in Chemically Doped Semiconducting Polymers. *Chem. Mater.* **2021**, *33* (7), 2343–2356.

(14) Aubry, T. J.; Winchell, K. J.; Salamat, C. Z.; Basile, V. M.; Lindemuth, J. R.; Stauber, J. M.; Axtell, J. C.; Kubena, R. M.; Phan, M. D.; Bird, M. J.; et al. Tunable Dopants with Intrinsic Counterion Separation Reveal the Effects of Electron Affinity on Dopant Intercalation and Free Carrier Production in Sequentially Doped Conjugated Polymer Films. *Adv. Funct. Mater.* **2020**, *2001800*, 1–13.

(15) Aubry, T. J.; Axtell, J. C.; Basile, V. M.; Winchell, K. J.; Lindemuth, J. R.; Porter, T. M.; Liu, J. Y.; Alexandrova, A. N.; Kubiak, C. P.; Tolbert, S. H.; et al. Dodecaborane-Based Dopants Designed to Shield Anion Electrostatics Lead to Increased Carrier Mobility in a Doped Conjugated Polymer. *Adv. Mater.* **2019**, *31* (11), 1–8.

(16) Wixtrom, A. I.; Shao, Y.; Jung, D.; Machan, C. W.; Kevork, S. N.; Qian, E. A.; Axtell, J. C.; Khan, S. I.; Kubiak, C. P.; Spokoyny, A. M. Rapid Synthesis of Redox-Active Dodecaborane B12(OR)12 Clusters under Ambient Conditions. *Inorg. Chem. Front.* **2016**, *3* (5), 711–717.

(17) Scholes, D. T.; Hawks, S. A.; Yee, P. Y.; Wu, H.; Lindemuth, J. R.; Tolbert, S. H.; Schwartz, B. J. Overcoming Film Quality Issues for Conjugated Polymers Doped with F4TCNQ by Solution Sequential Processing: Hall Effect, Structural, and Optical Measurements. *J. Phys. Chem. Lett.* **2015**, *6* (23), 4786–4793.

(18) Doucet, M.; Ferraz Leal, R. M.; Hobson, T. C. Web Interface for Reflectivity Fitting. *SoftwareX* **2018**, *7*, 287–293.

(19) Jiang, Z. GIXSGUI: A MATLAB Toolbox for Grazing-Incidence X-Ray Scattering Data Visualization and Reduction, and Indexing of Buried Three-Dimensional Periodic Nanostructured Films. *J. Appl. Crystallogr.* **2015**, *48*, 917–926.

(20) Ilavsky, J. Nika: Software for Two-Dimensional Data Reduction. *J. Appl. Crystallogr.* **2012**, *45* (2), 324–328.

(21) Müller-Buschbaum, P. The Active Layer Morphology of Organic Solar Cells Probed with Grazing Incidence Scattering Techniques. *Adv. Mater.* **2014**, *26* (46), 7692–7709.

(22) Tremel, K.; Ludwigs, S. *P3HT Revisited – From Molecular Scale to Solar Cell Devices*; 2014; Vol. 265.

(23) Aubry, T. J.; Winchell, K. J.; Salamat, C. Z.; Basile, V. M.; Lindemuth, J. R.; Stauber, J. M.; Axtell, J. C.; Kubena, R. M.; Phan, M. D.; Bird, M. J.; et al. Tunable Dopants with Intrinsic Counterion Separation Reveal the Effects of Electron Affinity on Dopant Intercalation and Free Carrier Production in Sequentially Doped Conjugated Polymer Films. *Adv. Funct. Mater.* **2020**.

(24) Lindemuth, J.; Mizuta, S.-I. Hall Measurements on Low-Mobility Materials and High Resistivity Materials. In *Thin Film Solar Technology III*; Eldada, L. A., Ed.; SPIE, 2011; Vol. 8110, pp 65–71.

(25) Lindemuth, J. Variable Temperature Hall Measurements on Low-Mobility Materials.

In *Thin Film Solar Technology IV*; Eldada, L. A., Ed.; SPIE, 2012; Vol. 8470, pp 58–66.

(26) Chen, Y.; Yi, H. T.; Podzorov, V. High-Resolution Ac Measurements of the Hall Effect in Organic Field-Effect Transistors. *Phys. Rev. Appl.* **2016**, *5* (3), 1–9.

(27) Scholes, D. T.; Yee, P. Y.; Lindemuth, J. R.; Kang, H.; Onorato, J.; Ghosh, R.; Luscombe, C. K.; Spano, F. C.; Tolbert, S. H.; Schwartz, B. J. The Effects of Crystallinity on Charge Transport and the Structure of Sequentially Processed F4TCNQ-Doped Conjugated Polymer Films. *Adv. Funct. Mater.* **2017**, *27* (44).

(28) Mitchell, W. J.; Burn, P. L.; Thomas, R. K.; Fragneto, G.; Markham, J. P. J.; Samuel, I. D. W. Relating the Physical Structure and Optical Properties of Conjugated Polymers Using Neutron Reflectivity in Combination with Photoluminescence Spectroscopy. *J. Appl. Phys.* **2004**, *95* (5), 2391–2396.

(29) Murrey, T. L.; Guo, K.; Mulvey, J. T.; Lee, O. A.; Cendra, C.; Bedolla-Valdez, Z. I.; Salleo, A.; Moulin, J. F.; Hong, K.; Moulé, A. J. Additive Solution Deposition of Multi-Layered Semiconducting Polymer Films for Design of Sophisticated Device Architectures. *J. Mater. Chem. C* **2019**, *7* (4), 953–960.

(30) Perlich, J.; Rubeck, J.; Botta, S.; Gehrke, R.; Roth, S. V.; Ruderer, M. A.; Prams, S. M.; Rawolle, M.; Zhong, Q.; Körstgens, V.; et al. Grazing Incidence Wide Angle X-Ray Scattering at the Wiggler Beamline BW4 of HASYLAB. *Rev. Sci. Instrum.* **2010**, *81* (10), 1–7.

(31) Yee, P. Y.; Scholes, D. T.; Schwartz, B. J.; Tolbert, S. H. Dopant-Induced Ordering of Amorphous Regions in Regiorandom P3HT. *J. Phys. Chem. Lett.* **2019**, *10* (17), 4929–4934.

(32) Aubry, T. J.; Winchell, K. J.; Salamat, C. Z.; Basile, V. M.; Lin-, J. R.; Stauber, J. M.; Axtell, J. C.; Kubena, R. M.; Phan, M. D.; Bird, J.; et al. Tunable Dopants with Intrinsic Counterion Separation Reveal the Effects of Electron Affinity on Dopant Intercalation and Free Carrier Production in Sequentially Doped Conjugated Polymer Films. 1–41.

Chapter 4. Tuning the Structure of P3HT by Rub-Aligning to Control the Propensity for Chemical Doping

4.1 Introduction

Semiconducting polymers are predicted to find wide use in future electronic devices because of their low cost, versatility, scalability, and solution processability.[1–8] Undoped semiconducting polymers are inherently poor conductors due to their wide band gaps and low density of intrinsic charge carriers.[9] As a result, doping is required to generate the carriers that make semiconducting polymers conductive.[10] Similar to impurity doping in inorganic semiconductors, semiconducting polymer doping occurs via charge transfer between the polymer and dopant molecules introduced into the polymer film.[11] Electrons can be either injected into the polymer conduction band (*n*-type) or withdrawn from the polymer valence band (*p*-type) to determine the majority carrier type in the film.[12,13] Most studies focus on *p*-type semiconducting polymers due to their better stability than *n*-type materials.[14]

In addition to selecting a dopant with a redox level that matches or exceeds the valence band energy of a semiconducting polymer, it is also critical to understand the structural changes of the host polymer during dopant introduction. Semiconducting polymer films are usually semicrystalline, containing both crystalline and amorphous regions.[15] Our previous work shows that the polymer's degree of crystallinity can affect charge mobility by controlling where the dopants reside in the polymer film's structure.[16] Compared with amorphous regions, crystalline regions are easier to dope and the resulting carriers have better mobility.[17,18] This means that the macroscopic doped polymer film conductivity is governed by the structure and extent of the crystalline regions.[19]. For this reason, it is crucial to understand how a conjugated polymer's crystalline structure affects the doping process.

It has been well-established that when semiconducting polymers become doped, dopant molecules intercalate into the lamellar side-chain regions of the polymer crystallites.[20] Due to limited space in the lamellar region, the crystallite structure must often undergo a phase transition to accommodate the dopant molecules, resulting in a new crystal structure with an extended side chain distance and decreased π-π distance.[18,21,22] Many doped conjugated polymer systems, including doped polymers that have undergone anion exchange, exhibit such a structural rearrangement.[20,21,23–25] Interestingly, our previous work shows that very large (~2 nm dia.) dodecaborane-based dopants also intercalate into the polymer lamellar side-chain region, in this case leading to a doubling of the crystallite lamellar spacing.[26,27] Such structural rearrangement upon doping does not happen if there is steric hindrance in the lamellar region, as shown by Thomas *et al*., who found that the use of branched side chains on a poly(3-hexylthiophene-2,5-diyl) (P3HT) derivative forced the dopant 2,3,5,6-tetrafluoro-7,7,8,8-tetracyanoquinodimethane (F4TCNQ) to π-stack with the polymer backbone, changing the nature of the doping.[28]

Among doped semiconducting polymers, the F4TCNQ-doped P3HT system is well-studied. P3HT crystallites have a monoclinic unit cell with tilted side chains.[29] P3HT has been shown to form both edge-on (i.e., alkyl side chains contacting the substrate) and face-on (i.e., backbone rings contacting the substrate) crystallites depending on processing conditions and substrate interfacial energy.[30–33] Work from Brinkmann and co-workers showed that rubbing P3HT films aligns the polymer chains, resulting in high crystallinity along the backbone direction.[21,34–37] Electron diffraction (ED) showed that the rub-aligned films are composed of both face-on and edge-on oriented P3HT polymorphs.[21,23,35] These workers were able to use the aligned P3HT system to investigate how the P3HT crystalline structure changed upon doping by separating the different lattice directions. They found that when F4TCNQ intercalates into the polymer lamellar side chain

region, the polymer side chains untilt, resulting in a new unit cell structure. [21] We note, however, that the use of ED in their work, which can only probe in-plane periodicity, means that the observed structure changes were based on examining the lamellar distance in face-on doped P3HT polymorphs and the π-π distance in edge-on polymorphs.

In this work, we build on this previous work by using 2-D grazing-incidence wide-angle x-ray scattering (GIWAXS)[38] to fully characterize the structures of both the edge-on and face-on polymorphs in F4TCNQ-doped rub-aligned P3HT films. GIWAXS reveals that although the two polymorphs have similar crystal structures, their unit cells are in fact somewhat different. Compared to the edge-on P3HT polymorph, the face-on P3HT polymorph has a slightly larger lamellar spacing, less tilted side chain angle, and smaller π-π distance. We then show that by starting with a very low doping concentration and increasing the doping in small steps, we can examine a region where both undoped and F4TCNQ-doped polymorphs coexist. We find that the face-on P3HT polymorph becomes doped first, followed by the edge-on P3HT polymorph at higher doping concentrations. We argue that this results from the fact that the undoped face-on polymorph has a crystal structure that is more akin to the final doped crystal structure, explaining why it is easier to dope. This finding demonstrates that even minor variations in the initial polymer crystallite structure strongly influences the ease of conjugated polymer doping, and suggests a strategy to design new polymers that are easier to dope.

4.2 Experimental and Methods

Materials

Poly(3-hexylthiophene-2,5-diyl) (Mn = 50-70 kg/mol, regioregularity 91-94%) was purchased from Rieke metals inc. F4-TCNQ (Purity > 99.0%) were purchased from Ossila. 1,2 dichlorobenzene (anhydrous, 99%), Acetonitrile (anhydrous, 98%), and Dichloromethane (anhydrous, 99.8% with 40-150ppm of amylene as a stabilizer) were purchased from Sigma-Aldrich.

Experimental Methods

Aligned Film Fabrication

P3HT films were prepared on ~1.5 x 1.5 cm substrates (glass or silicon). The substrates were cleaned sequentially with Alconox detergent, deionized water, isopropanol, and acetone. Immediately after washing, the substrates were plasma cleaned using Harrick Plasma Cleaner PDC-32G for 15 minutes. Substrates were then transferred to a nitrogen glove box and spin-coated with 20 mg/mL P3HT in 1,2 dichlorobenzene. Spin coating was done at 1000 rpm for 60 seconds, followed by 4000 rpm for 5 seconds to remove excess solvent. Next, the pre-cast P3HT films were transferred to an argon glove box for rub-aligning. The rub-aligning was done by heating the pre-cast P3HT films to 140^{o}C and translating it across a rotating microfiber wheel. The aligned films were doped with F4TCNQ at the stated concentrations and solvent through a second spin coating step at 4000 rpm for 10 seconds.

Spectroscopy

Polarized UV-Vis absorptions were done using a Shimadzu UV3101PC Scanning Spectrophotometer. All samples for polarized UV-Vis absorptions were prepared on glass substrates.

GIWAXS

Samples were prepared on silicon substrates. Measurements were performed on beamline 11-3 at the Stanford Synchrotron Radiation Lightsource. The beam wavelength is 0.9742 Å and incidence angle is 0.12◦. Samples were placed in a helium chamber to increase signal-to-noise. The sample to detector distance is 250 mm and the spot size on the image plate is ∼150 µm. The 2-D diffractograms were radially integrated with 0-10◦ and 80-90◦ to obtain the in-plane and out-of-plane diffraction patterns. The Nika macro was used to calibrate the beam and the WAXStools macro was used to reduce the GIWAXS data and for subsequent analysis in IgorPro.

4.3 Results and Discussions

To carry out our studies, we utilized the high-temperature rubbing method introduced by Brinkmann and co-workers to obtain highly-aligned P3HT films.[34] First, P3HT was spin-coated onto glass substrates from 1,2-dichlorobenzene (ODCB) to produce films of uniform thickness. The P3HT films were then rub-aligned using a microfiber wheel while being heated (see the Supporting Information, SI, for more details). The degree of film alignment was then characterized using polarized UV-Vis spectroscopy, in which the polarized light was oriented parallel (||) or perpendicular (⊥) to the direction of rub alignment.

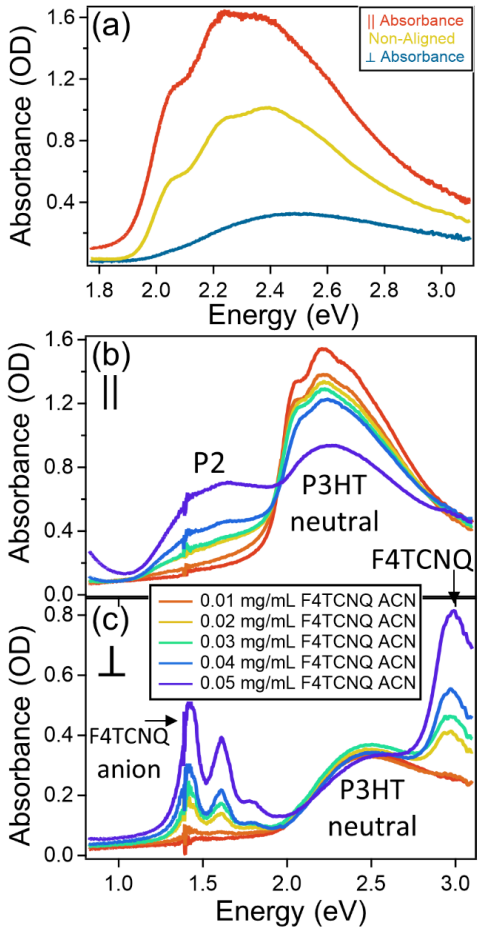

Figure 4.1: Polarized UV-Vis absorbance of (a) unaligned P3HT and aligned P3HT in the parallel (||) and perpendicular (⊥) directions. Aligned P3HT shows anisotropic absorbance spectra in the two polarization directions. (b) Aligned P3HT doped by F4TCNQ at varied concentrations in the (b) parallel and (c) perpendicular directions. Both the decreasing bandgap transition and increasing P2 transition in the parallel direction indicate higher doping level with increasing dopant concentration. F4CTNQ does not appear to dope polymer species visible in the perpendicular direction. Absorbance features of the F4TCNQ dopant anion in the perpendicular direction indicate the long axis of the F4TCNQ molecule is perpendicular to the P3HT backbone.

Figure 4.1a shows polarized UV-Vis spectra of unaligned (orange curve) and rub-aligned (red curve for || and blue curve for ⊥) P3HT films. The polarized absorbance of the aligned film shows significant anisotropy, with a dichroic ratio of ~14 at 610 nm, comparable to previous work.[35,39] In addition to the anisotropy, the absorption spectrum of the rub-aligned film is quite different from the unaligned film, showing that rub-alignment has had a significant effect on the film's structure. The isotropic absorbance of unaligned P3HT shows a vibronic progression with

peaks at 2.03 eV (0-0 transition, $A_{0\text{-}0}$) and 2.23 eV (0-1 transition, $A_{0\text{-}1}$). In contrast, the aligned P3HT films shows an absorption spectrum polarized in the parallel direction with a larger $A_{0\text{-}0}$-to-$A_{0\text{-}1}$ peak ratio than is seen with unaligned P3HT. This results from improved intrachain coupling caused by backbone straightening during rub-aligning (Figure 4.1a).[40–42] With perpendicular polarization, rub-aligned P3HT reveals a blue-shifted absorbance peak with no vibronic features, likely corresponding to the residual absorbance of short or amorphous polymer chains.[21]

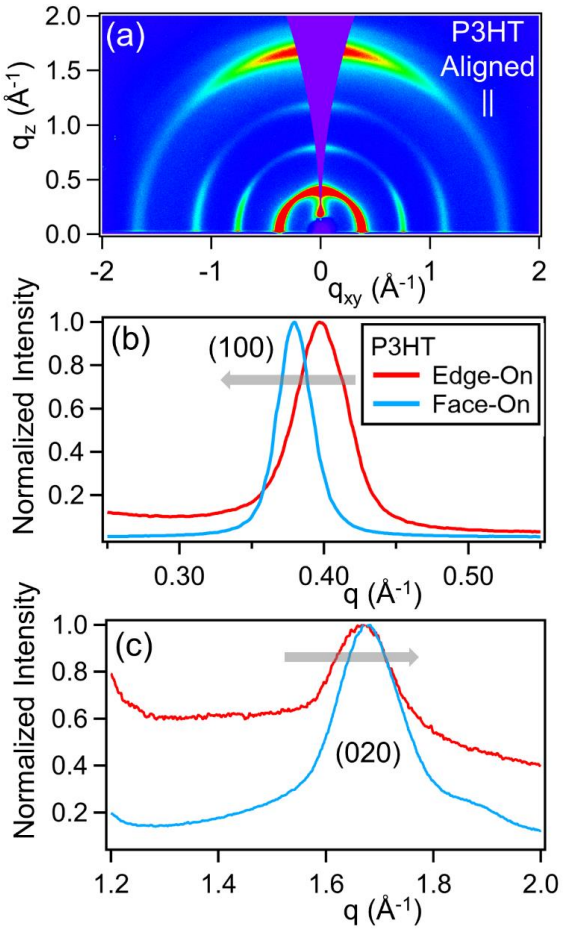

Figure 4.2: (a) 2D GIWAXS pattern for aligned P3HT in the parallel direction. Integrated (b) (100) lamellar and (c) π-stacking peak of aligned P3HT for the edge-on and face-on oriented crystallites, based on panel (a). Face-on P3HT has a larger lamellar side chain spacing and smaller π-stacking distance compared to edge-on P3HT.

Although polarized UV-Vis spectroscopy can help determine the degree of polymer alignment, it does not provide details on the structure and orientation of polymer crystallites. This is why we employed GIWAXS to determine the structure of the polymer crystallites in rub-aligned P3HT films.[43,44] As illustrated in Figure S1a, the crystallites in unaligned P3HT films usually adopt an edge-on orientation with respect to the substrate.[45] The out-of-plane diffraction peaks corresponding to the unit cell distance along the lamellar side chain direction are designated (100), (200), and (300), while the in-plane diffraction peak corresponding to the π-stacking distance is labeled (020).[36] We note that the P3HT monomer repeat distance and the π-stacking distance have comparable length scales, so these two peaks can be difficult to distinguish.[21]

As mentioned in the Introduction, when F4TCNQ dopants infiltrate into the lamellar region of unaligned P3HT cyrstrallites, the side-chains are straightened, resulting in a new crystalline structure with an increased side-chain distance (Figure S1c orange curve) and decreased π-stacking distance (Figure S1d orange curve).[21] Figure 4.2a shows a GIWAXS diffraction pattern for a rub-aligned P3HT film in which the X-ray beam is incident parallel to the rub-alignment direction. Unlike with unaligned films, both lamellar and π-stacking diffraction peaks are seen in both the in-plane and out-of-plane directions, suggesting the coexistence of edge-on and face-on P3HT polymorphs. Integrating the diffraction peaks along q in the different directions reveals differences between the two crystalline structures. The face-on P3HT polymorph has a larger lamellar distance and a smaller π-stacking distance than the edge-on polymorph, as seen in Figures 4.2b, c, and the face-on polymorph has a less tilted unit cell. We note that the face-on P3HT polymorph has a more similar structure to that of F4TCNQ-doped P3HT than the edge-on polymorph. In what follows, we will take advantage of the fact that we can easily observe the two differently-oriented

polymorphs to showthat the subtle differences in structure between the edge-on and face-on P3HT polymorphs affect the energetics for doping.

To examine the effect of crystallite structure on doping, we doped rub-aligned P3HT films with F4TCNQ at low concentrations in small increments to capture the doping phase transition point of both the edge-on and face-on P3HT polymorphs. The films were doped using sequential processing (SqP), in which dopant solutions were spin-coated onto rub-aligned P3HT films from solvents that swell but do not dissolve the polymer, an approach that generally preserves the underlying film morphology while doping.[45] The polarized absorption spectra of rub-aligned P3HT films doped with different concentrations of F4TCNQ are shown in Figure 4.1b, c. The fact that the polarized absorption is still anisotropic indicates that most of the alignment is retained through the SqP doping process.[21]

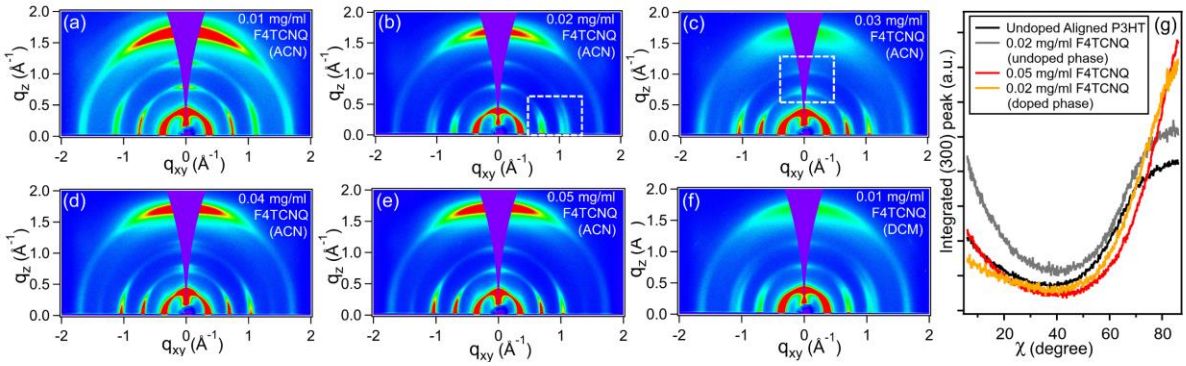

Figure 4.3: (a)-(e) 2D GIWAXS patterns of aligned P3HT doped with different concentrations of F4TCNQ in ACN (parallel direction). Face-on-oriented P3HT dopes first at 0.02 mg/ml F4TCNQ, then edge-on P3HT dopes at 0.03 mg/ml F4TCNQ. (f) 2D GIWAXS pattern of aligned P3HT doped with 0.01 mg/ml F4TCNQ in DCM. (g) 1D integrated GIWAXS patterns along the altitudinal angle χ of the lamellar (300) peak of undoped, 0.02 mg/ml and 0.05 mg/ml F4TCNQ-doped aligned P3HT. Compared with undoped face-on P3HT, the doped phase has a narrower χ -distribution, indicating more parallel with the substrate.

As is well documented, doping P3HT bleaches the bandgap transition and generates new intraband electronic states, which are usually labelled P1 and P2 in order of their energy. The P2 transition near 1.5 eV is visible in Figure 4.1b only using light polarized along the alignment direction, as also seen previously by Brinkmann and co-workers.[46] With the perpendicular polarization, only the absorption spectrum of the $F4TCNQ^{-}$ anion is seen in this spectral region, showing that the F4TCNQ dopant counterions sit in the crystallite with their long axis oriented perpendicular to the P3HT backbone. Taken together, the data in Figure 4.1 indicate that at these low doping concentrations, only aligned crystallites are doped. This fits with previous work that also found that crystalline regions doped more easily than amorphous regions.[18]

We can gain molecular insight into the nature of the aligned doping process using GIWAXS. Figures 4.3a-e show GIWAXS diffraction patterns of the same samples whose polarized absorption spectra are characterized in Figures 4.1b, c. All the samples exhibit out-of- and in-plane diffraction peaks, indicating co-existence of face-on and edge-on polymorphs throughout the doping process. Close inspection of the data shows that the face-on P3HT polymorph ((*h*00) peaks lying in-plane) has a doubled lamellar peak when the F4TCNQ dopant concentration is 0.02 mg/ml, as seen in the white box in Figure 4.3b. Figures 4.4a, c show the 1D radial integration patterns of face-on and edge-on P3HT lamellar peaks in Figure 4.3a-e. The (200) peak in Figures 4.4a, c is enlarged in Figures 4.4b, d. The doubled lamellar peak in Figure 4.4b (orange curve) further confirms the doubled lamellar diffraction spots in Figure 4.3b. Such doubled lamellar peak has been observed in F4TCNQ doped unaligned P3HT film (Figure S1b-d). The presence of two different peaks implies phase coexistence, as is expected to occur during a first-order phase transition in which a discrete change in system energy occurs that favors the nucleation of the new phase within the existing phase.[47] Crucially, the edge-on polymorph ((*h*00)

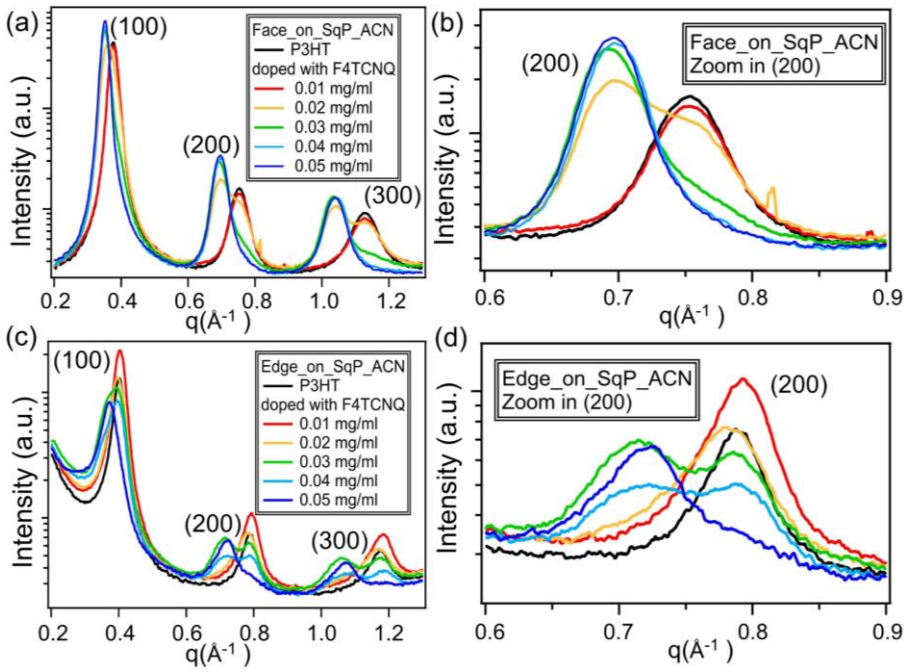

Figure 4.4: 1D integrated GIWAXS patterns in the lamellar peaks region of the aligned P3HT (a) face-on and (c) edge-on fractions. Zoomed-in 1D integrated patterns of the (b) face-on and (d) edge-on P3HT (200) peak. The double lamellar peak indicates the coexistence of undoped and doped phases. Face-on P3HT is doped first at 0.02 mg/ml F4TCNQ, followed by edge-on P3HT at 0.03 mg/ml.

peaks lying out-of-plane) shows no such peak doubling at this concentration, indicating that the face-on and edge-on polymorphs undergo different doping kinetics. Thus, the data in Figure 4.3b and 4.4b indicate that the face-on P3HT polymorph becomes doped and undergoes a phase transition at a 0.02 mg/ml F4TCNQ dopant concentration, while the edge-on P3HT polymorph remains undoped. Figure 4.3c (inside white box) and Figure 4.4d (green curve) show that upon increasing the concentration of F4TCNQ to 0.03 mg/mL, the doping phase transition for the face-on P3HT polymorph continues and the edge-on P3HT begins to show its doping-induced phase transition. By 0.05 mg/ml F4TCNQ concentration, both the face-on and edge-on P3HT polymorphs have completed their doping phase transition, as indicated by Figure 4.3e and Figure 4.4b, d (navy blue curve). In general, the appearance of the face-on lamellar double-peak of before

that of edge-on P3HT in Figure 4.3 and 4.4 provides evidence that the face-on polymorph is easier to dope.

The results in Figure 4.3 and 4.4 lead to the question of whether the difference in doping onset for the face-on and edge-on polymorphs is due to different energetics for doping these different structures or different kinetics in accessing the different polymorphs during the doping process. For example, if the face-on-oriented crystallites were primarily located at the upper part of the film from the rubbing process, they might be easier to access during sequential doping than edge-on oriented crystallites that might lie closer to the substrate. Indeed, the data shown in Figures 4.3 and 4.4 were taken on rub-aligned P3HT that were sequentially doped using acetonitrile (ACN), a poor swelling solvent for P3HT that might not provide good access to the bottom of the film. Thus, to make sure that swelling kinetics were not important in the observed order of the doping phase transition, we repeated the experiment using dichloromethane (DCM) as the doping solvent; DCM is an excellent swelling solvent for P3HT, allowing large molecules like fullerenes to penetrate all the way to the substrate through thick polymer films.[26] Figure 4.3f (along with additional data in Figure S4) shows that the use of DCM lowers the concentration needed to start the doping transition to 0.01 mg/mL F4TCNQ, consistent with the better swelling, but it also shows that the face-on P3HT polymorph still dopes first. This supports our theory that the face-on P3HT polymorph dopes more easily because its initial crystallite structure is closer to the final doped structure.

Lattice spacings calculated based on the lamellar and π-stacking peak positions of doped and undoped face-on and edge-on P3HT polymorphs are shown in Table S1. The lattice spacings of the two doped polymorphs are same (17.94 Å for lamellar distance and 3.55 Å for π-π distance). The undoped face-on polymorph has a larger lamellar distance (16.53 Å) than edge-on polymorph

(16.10 Å), and a smaller pi-pi distance (3.76 Å) than edge-on polymorph (3.78 Å). So the spacing of the face-on P3HT polymorphs is closer to that of the doped structure. Thus face-on P3HT polymorph requires less structural rearrangement to reach the final doped structure, which translates into less energetics to transform to the doped phase. Face-on P3HT polymorph also has a smaller π-stacking distance than edge-on one, which may lead to greater polaron delocalization as a stabilizing factor initially upon doping and prior to crystallite rearrangement. The reason for the preferential doping of the face-on polymorph at low dopant concentrations likely lies in a balance of these two factors. The difference in doping order of edge-on and face-on P3HT polymorphs is therefore attributed to the more similar structure of the face-on P3HT polymorph to that of the doped one. This similarity makes it more energetically favorable to dope the face-on polymorph first.

An interesting consequence of the changes in lattice spacings observed is the narrowing of the χ-angular distribution of the face-on polymorph fraction. 1D integrated patterns of the (300) lamellar peak of undoped, partially doped (0.02 mg/mL F4TCNQ), and fully doped (0.05 mg/ml F4TCNQ) aligned P3HT films are shown in Figure 4.3g. The (300) peak of the doped film is observed to have a broader distribution in altitudinal χ-angle (~15° FWHM) than the undoped film (~30°). This difference is mirrored in the partially doped film, in which the doped phase has a broader distribution in altitudinal χ-angle (~20°) than the undoped phase (~30°) of the same film. Because the χ-distribution of a diffraction peak relates to the angular distribution of crystallites in the film, the face-on crystallites align more parallel to the substrate when doped. This effect is possibly due to interactions between the expanding crystallites; as the face-on crystallites expand in the lamellar stacking direction during doping, they exert torque on each other through points of contact that aligns them more mutually parallel. Crystallite expansion upon doping is thus

observed to be an ordering force, reducing some of the angular disorder produced during the rub-aligning process.

4.4 Summary

In summary, we have shown that rub-aligned P3HT contains two different crystalline polymorphs: the typical edge-on oriented polymorph seen in unaligned films, and a new rub-induced polymorph that sits face-on to the substrate and has a slightly larger lamellar and slightly smaller p-stacking spacing than the edge-on polymorph. The fact that the two polymorphs are oriented in different directions allows us to use GIWAXS to investigate how slightly altering the crystal structure of a polymer changes its propensity to be doped. We find that the face-on polymorph undergoes its first-order doping phase transition more easily than the edge-on polymorph. This is because the initial crystallite structure of the face-on P3HT polymorph is more similar to the final doped P3HT structure, providing either a lower barrier to doping or a larger thermodynamic driving force. This finding provides a design rule for creating new semiconducting polymers that are more easily doped: the more the undoped crystal structure resembles the doped crystal structure, the easier it will be to insert dopants because the energetics of making the phase transition are more favorable.

4.5 Supporting Information

Grazing-Incidence Wide-Angle X-ray Scattering (GIWAXS)

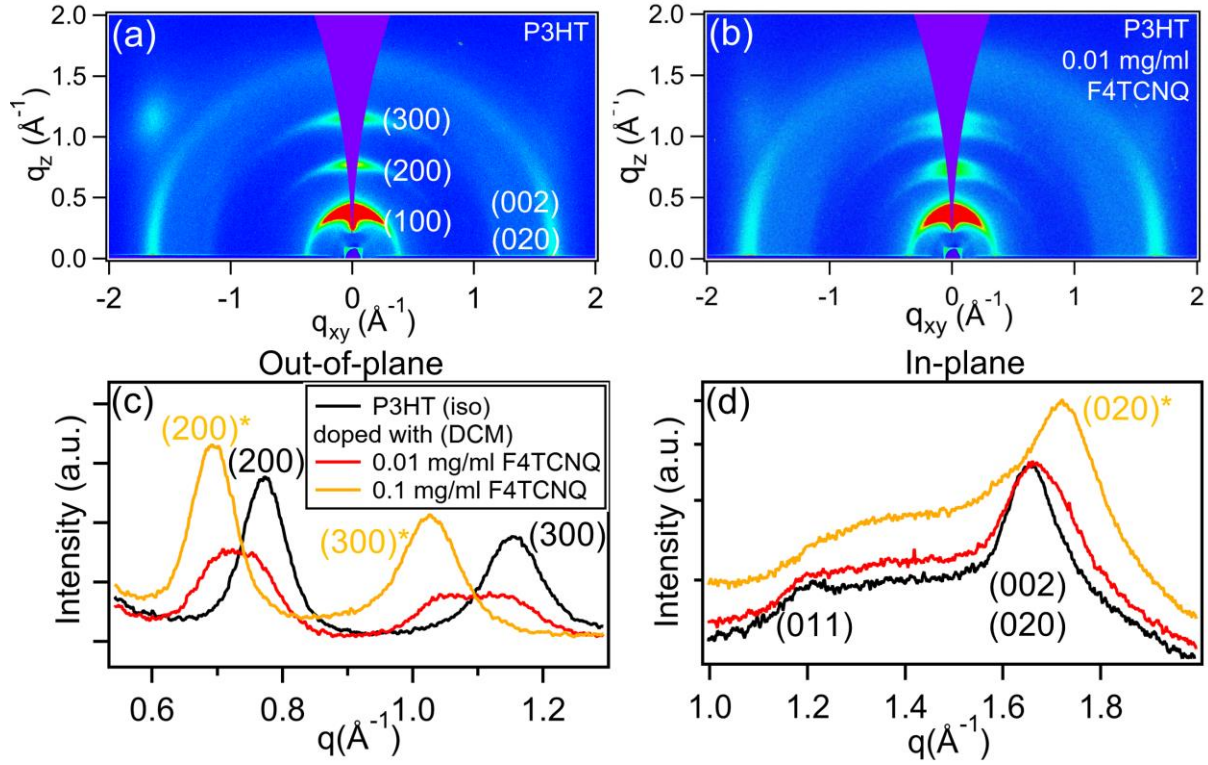

Figure S1: (a) GIWAXS for unaligned P3HT. P3HT is in edge-on texture. Lamellar peaks are out-of-plane and labeled as (100), (200) and (300). Monomer peak and π-π stacking peak are in-plane and labeled as (002) and (020). (b) P3HT doped with 0.01 mg/ml F4TCNQ. Lamellar overtones show the doubled lamellar peak, indicating the co-existence of undoped and doped P3HT (first-order phase transition). (c) Integrated lamellar peaks and (d) π peaks of F4TCNQ doped P3HT.

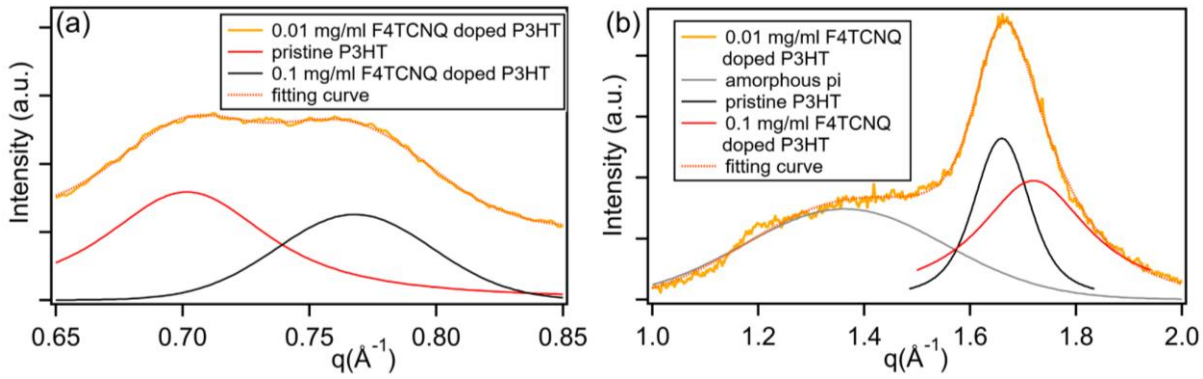

Figure S2: Peak fitting of 0.01 mg/ml F4TCNQ doped P3HT with undoped and doped P3HT peaks. (a) (200) peak fitting, (b) (020) peak fitting.

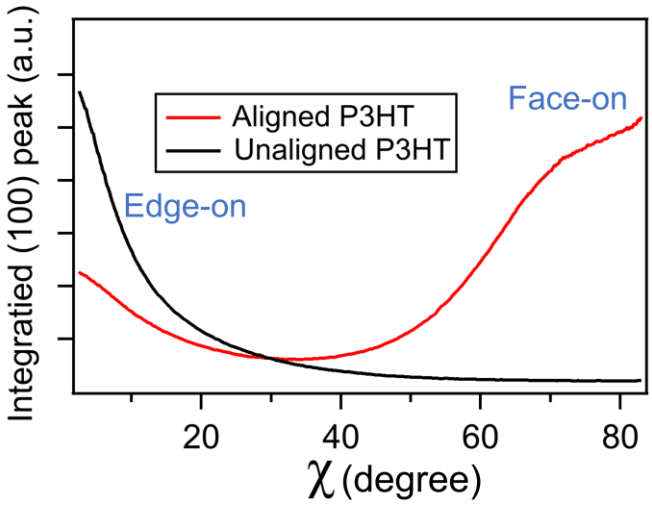

Figure S3: χ integration of (100) lamellar peak of unaligned and aligned P3HT (parallel direction). Unaligned P3HT is edge-on texture, aligned P3HT has both edge-on and face-on textures.

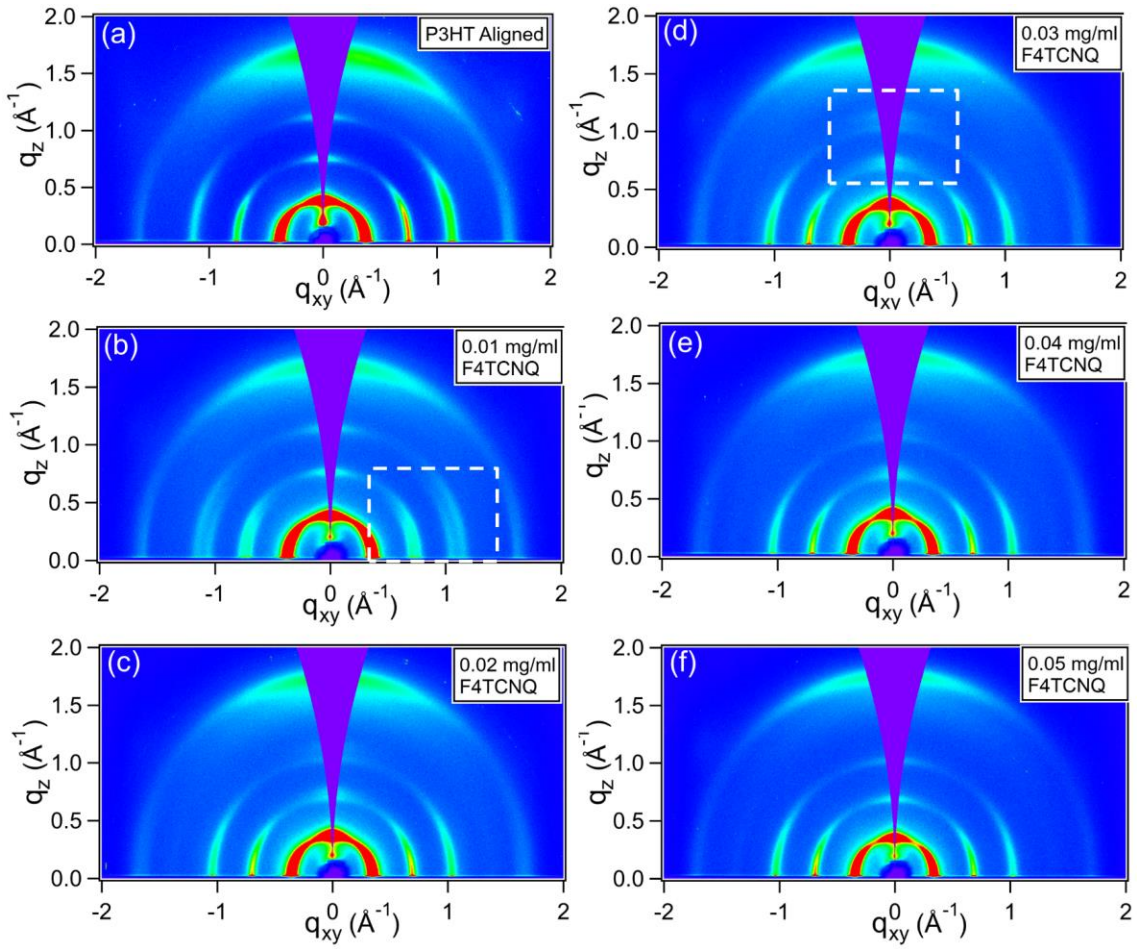

Figure S4: GIWAXS for aligned P3HT parallel direction (a), aligned P3HT SqP doped from DCM with 0.01 mg/ml F4TCNQ (b), 0.02 mg/ml F4TCNQ (c), 0.03 mg/ml F4TCNQ (d), 0.04 mg/ml F4TCNQ (e), 0.05 mg/ml F4TCNQ. Face-on P3HT gets doped first at 0.01 mg/ml F4TCNQ, followed by edge-on P3HT which gets doped at 0.02 mg/ml F4TCNQ.

Table S1: Lamellar and π- π distance of undoped and doped aligned P3HT edge-on and face-on polymorphs.

	Face-on	Doped face-on	Edge-on	Doped edge-on
Lamellar Distance (Å)	16.53	17.94	16.10	17.94
π Distance (Å)	3.76	3.55	3.78	3.55

4.6 References

(1) Forrest, S. R. Electronic Appliances on Plastic. *Nature* **2004**, *428* (6986), 911–918.

(2) Tiwari, S.; Singh, A. K.; Joshi, L.; Chakrabarti, P.; Takashima, W.; Kaneto, K.; Prakash, R. Poly-3-Hexylthiophene Based Organic Field-Effect Transistor: Detection of Low Concentration of Ammonia. *Sensors Actuators, B Chem.* **2012**, *171–172*, 962–968.

(3) Hou, L.; Zhang, X.; Cotella, G. F.; Carnicella, G.; Herder, M.; Schmidt, B. M.; Pätzel, M.; Hecht, S.; Cacialli, F.; Samorì, P. Optically Switchable Organic Light-Emitting Transistors. *Nat. Nanotechnol.* **2019**.

(4) Chung, D. Y.; Huang, J.; Bradley, D. D. C.; Campbell, A. J. High Performance, Flexible Polymer Light-Emitting Diodes (PLEDs) with Gravure Contact Printed Hole Injection and Light Emitting Layers. *Org. Electron.* **2010**, *11* (6), 1088–1095.

(5) Rezvani, M. H.; Farajollahi, F.; Nikfarjam, A.; Bakhtiarpour, P.; Saydanzad, E. Effect of Solvents, Their Mixture and Thermal Annealing on the Performance of Solution Processed Polymer Light-Emitting Diodes. *Materials (Basel).* **2013**, *6* (5), 1994–2006.

(6) Zhang, S.; Ye, L.; Hou, J. Breaking the 10% Efficiency Barrier in Organic Photovoltaics: Morphology and Device Optimization of Well-Known PBDTTT Polymers. *Adv. Energy Mater.* **2016**, *6* (11), 1–20.

(7) Nelson, J. Polymer: Fullerene Bulk Heterojunction Solar Cells. *Mater. Today* **2011**, *14* (10), 462–470.

(8) Qiu, L.; Zheng, X.; Zhang, J.; Yang, Y.; Cao, W.; Dong, Y.; Xia, D.; Zhou, X.; Fan, R. Insights into the Mechanism of Solid-State Metal Organic Complexes as Controllable and Stable p-Type Dopants in Efficient Planar Perovskite Solar Cells. *ACS Appl. Mater. Interfaces* **2020**, *12* (1), 546–555.

(9) Tremel, K.; Ludwigs, S. *P3HT Revisited – From Molecular Scale to Solar Cell Devices*; 2014; Vol. 265.

(10) Heeger, A. J. Semiconducting Polymers: The Third Generation. *Chem. Soc. Rev.* **2010**, *39* (7), 2354–2371.

(11) Oba, F.; Tatsumi, K.; Adachi, H.; Tanaka, I. N- and p-Type Dopants for Cubic Silicon Nitride. *Appl. Phys. Lett.* **2001**, *78* (11), 1577–1579.

(12) Yang, C. Y.; Jin, W. L.; Wang, J.; Ding, Y. F.; Nong, S.; Shi, K.; Lu, Y.; Dai, Y. Z.; Zhuang, F. D.; Lei, T.; et al. Enhancing the N-Type Conductivity and Thermoelectric Performance of Donor–Acceptor Copolymers through Donor Engineering. *Adv. Mater.* **2018**, *30* (43), 1–9.

(13) Yoon, S. E.; Kang, Y.; Jeon, G. G.; Jeon, D.; Lee, S. Y.; Ko, S. J.; Kim, T.; Seo, H.; Kim, B. G.; Kim, J. H. Exploring Wholly Doped Conjugated Polymer Films Based on Hybrid Doping: Strategic Approach for Optimizing Electrical Conductivity and Related Thermoelectric Properties. *Adv. Funct. Mater.* **2020**.

(14) Otellin, V. A.; Korzhevskii, D. E. Formation and Structural Organization of a Barrier on the Brain Outer Surface. *Morfologiia* **2002**, *122* (6), 14–18.

(15) Noriega, R.; Rivnay, J.; Vandewal, K.; Koch, F. P. V; Stingelin, N.; Smith, P.; Toney, M. F.; Salleo, A. A General Relationship between Disorder, Aggregation and Charge Transport in Conjugated Polymers. *Nat. Mater.* **2013**, *12* (11), 1038–1044.

(16) Scholes, D. T.; Yee, P. Y.; Lindemuth, J. R.; Kang, H.; Onorato, J.; Ghosh, R.; Luscombe, C. K.; Spano, F. C.; Tolbert, S. H.; Schwartz, B. J. The Effects of Crystallinity on Charge Transport and the Structure of Sequentially Processed F4TCNQ-Doped Conjugated Polymer Films. *Adv. Funct. Mater.* **2017**, *27* (44).

(17) Aubry, T. J.; Axtell, J. C.; Basile, V. M.; Winchell, K. J.; Lindemuth, J. R.; Porter, T. M.; Liu, J. Y.; Alexandrova, A. N.; Kubiak, C. P.; Tolbert, S. H.; et al. Dodecaborane-Based Dopants Designed to Shield Anion Electrostatics Lead to Increased Carrier Mobility in a Doped Conjugated Polymer. *Adv. Mater.* **2019**, *31* (11), 1–8.

(18) Scholes, D. T.; Yee, P. Y.; Lindemuth, J. R.; Kang, H.; Onorato, J.; Ghosh, R.; Luscombe, C. K.; Spano, F. C.; Tolbert, S. H.; Schwartz, B. J. The Effects of Crystallinity on Charge Transport and the Structure of Sequentially Processed F4TCNQ-Doped Conjugated Polymer Films. *Adv. Funct. Mater.* **2017**, *27* (44), 1–13.

(19) Alberga, D.; Perrier, A.; Ciofini, I.; Mangiatordi, G. F.; Lattanzi, G.; Adamo, C. Morphological and Charge Transport Properties of Amorphous and Crystalline P3HT and PBTTT: Insights from Theory. *Phys. Chem. Chem. Phys.* **2015**, *17* (28), 18742–18750.

(20) Yamashita, Y.; Tsurumi, J.; Ohno, M.; Fujimoto, R.; Kumagai, S.; Kurosawa, T.; Okamoto, T.; Takeya, J.; Watanabe, S. Efficient Molecular Doping of Polymeric Semiconductors Driven by Anion Exchange. *Nature* **2019**, *572* (7771), 634–638.

(21) Hamidi-Sakr, A.; Biniek, L.; Bantignies, J. L.; Maurin, D.; Herrmann, L.; Leclerc, N.; Lévêque, P.; Vijayakumar, V.; Zimmermann, N.; Brinkmann, M. A Versatile Method to Fabricate Highly In-Plane Aligned Conducting Polymer Films with Anisotropic Charge Transport and Thermoelectric Properties: The Key Role of Alkyl Side Chain Layers on the Doping Mechanism. *Adv. Funct. Mater.* **2017**, *27* (25), 1–13.

(22) Kohno, S.; Yamashita, Y.; Kasuya, N.; Mikie, T.; Osaka, I.; Takimiya, K.; Takeya, J.; Watanabe, S. Controlled Steric Selectivity in Molecular Doping towards Closest-Packed Supramolecular Conductors. *Commun. Mater.* **2020**, *1* (1), 1–8.

(23) Vijayakumar, V.; Zaborova, E.; Biniek, L.; Zeng, H.; Herrmann, L.; Carvalho, A.; Boyron, O.; Leclerc, N.; Brinkmann, M. Effect of Alkyl Side Chain Length on Doping Kinetics, Thermopower, and Charge Transport Properties in Highly Oriented F 4 TCNQ-Doped PBTTT Films. *ACS Appl. Mater. Interfaces* **2019**, *11* (5), 4942–4953.

(24) Karpov, Y.; Kiriy, N.; Formanek, P.; Hoffmann, C.; Beryozkina, T.; Hambsch, M.; Al-Hussein, M.; Mannsfeld, S. C. B.; Büchner, B.; Debnath, B.; et al. Sequentially Processed P3HT/CN6-CP•−NBu4+ Films: Interfacial or Bulk Doping? *Adv. Electron. Mater.* **2020**, *6* (5).

(25) Kroon, R.; Kemerink, M.; Hynynen, J.; Cano, A.; Nai, D.; McCulloch, I.; Liu, X.; Hofmann, A. I.; Marder, S. R.; Stegerer, D.; et al. Double Doping of Conjugated Polymers with Monomer Molecular Dopants. *Nat. Mater.* **2019**, *18* (2), 149–155.

(26) Aubry, T. J.; Axtell, J. C.; Basile, V. M.; Winchell, K. J.; Lindemuth, J. R.; Porter, T.

M.; Liu, J. Y.; Alexandrova, A. N.; Kubiak, C. P.; Tolbert, S. H.; et al. Dodecaborane-Based Dopants Designed to Shield Anion Electrostatics Lead to Increased Carrier Mobility in a Doped Conjugated Polymer. *Adv. Mater.* **2019**, *31* (11).

(27) Aubry, T. J.; Winchell, K. J.; Salamat, C. Z.; Basile, V. M.; Lin-, J. R.; Stauber, J. M.; Axtell, J. C.; Kubena, R. M.; Phan, M. D.; Bird, J.; et al. Tunable Dopants with Intrinsic Counterion Separation Reveal the Effects of Electron Affinity on Dopant Intercalation and Free Carrier Production in Sequentially Doped Conjugated Polymer Films. 1–41.

(28) Thomas, E. M.; Davidson, E. C.; Katsumata, R.; Segalman, R. A.; Chabinyc, M. L. Branched Side Chains Govern Counterion Position and Doping Mechanism in Conjugated Polythiophenes. *ACS Macro Lett.* **2018**, *7*, 1492–1497.

(29) Kayunkid, N.; Uttiya, S.; Brinkmann, M. Structural Model of Regioregular Poly(3-Hexylthiophene) Obtained by Electron Diffraction Analysis. *Macromolecules* **2010**, *43* (11), 4961–4967.

(30) Skrypnychuk, V.; Boulanger, N.; Yu, V.; Hilke, M.; Mannsfeld, S. C. B.; Toney, M. F.; Barbero. Enhanced Vertical Charge Transport in a Semiconducting P3ht Thin Film on Single Layer Graphene. *Adv. Funct. Mater.* **2015**, *25* (5), 664–670.

(31) Reinspach, J. A.; Diao, Y.; Giri, G.; Sachse, T.; England, K.; Zhou, Y.; Tassone, C.; Worfolk, B. J.; Presselt, M.; Toney, M. F.; et al. Tuning the Morphology of Solution-Sheared P3HT:PCBM Films. *ACS Appl. Mater. Interfaces* **2016**, *8* (3), 1742–1751.

(32) Meredig, B.; Salleo, A.; Gee, R. Ordering of Poly (3-Hexylthiophene) Surface Energy. *ACS Nano* **2009**, *3* (10), 2881–2886.

(33) Watanabe, S. I.; Tanaka, H.; Ito, H.; Kuroda, S. I.; Mori, T.; Marumoto, K.; Shimoi, Y. Direct Determination of Interfacial Molecular Orientations in Field-Effect Devices of P3HT/PCBM Composites by Electron Spin Resonance. *Org. Electron.* **2011**, *12* (4), 716–723.

(34) Biniek, L.; Pouget, S.; Djurado, D.; Gonthier, E.; Tremel, K.; Kayunkid, N.; Zaborova, E.; Crespo-Monteiro, N.; Boyron, O.; Leclerc, N.; et al. High-Temperature Rubbing: A Versatile Method to Align π-Conjugated Polymers without Alignment Substrate. *Macromolecules* **2014**, *47* (12), 3871–3879.

(35) Hartmann, L.; Tremel, K.; Uttiya, S.; Crossland, E.; Ludwigs, S.; Kayunkid, N.; Vergnat, C.; Brinkmann, M. 2D versus 3D Crystalline Order in Thin Films of Regioregular Poly(3-Hexylthiophene) Oriented by Mechanical Rubbing and Epitaxy. *Adv. Funct. Mater.* **2011**, *21* (21), 4047–4057.

(36) Untilova, V.; Biskup, T.; Biniek, L.; Vijayakumar, V.; Brinkmann, M. Control of Chain Alignment and Crystallization Helps Enhance Charge Conductivities and Thermoelectric Power Factors in Sequentially Doped P3HT:F4TCNQ Films. *Macromolecules* **2020**.

(37) Vijayakumar, V.; Durand, P.; Zeng, H.; Untilova, V.; Herrmann, L.; Algayer, P.; Leclerc, N.; Brinkmann, M. Influence of Dopant Size and Doping Method on the Structure and Thermoelectric Properties of PBTTT Films Doped with F6TCNNQ and F4TCNQ. *J. Mater. Chem. C* **2020**, *8* (46), 16470–16482.

(38) Rivnay, J.; Mannsfeld, S. C. B.; Miller, C. E.; Salleo, A.; Toney, M. F. Quantitative Determination of Organic Semiconductor Microstructure from the Molecular to Device Scale. *Chem. Rev.* **2012**, *112* (10), 5488–5519.

(39) Hamidi-Sakr, A.; Biniek, L.; Fall, S.; Brinkmann, M. Precise Control of Lamellar Thickness in Highly Oriented Regioregular Poly(3-Hexylthiophene) Thin Films Prepared by High-Temperature Rubbing: Correlations with Optical Properties and Charge Transport. *Adv. Funct. Mater.* **2016**, *26* (3), 408–420.

(40) Ghosh, R.; Pochas, C. M.; Spano, F. C. Polaron Delocalization in Conjugated Polymer Films. *J. Phys. Chem. C* **2016**, *120* (21), 11394–11406.

(41) Ghosh, R.; Luscombe, C. K.; Hambsch, M.; Mannsfeld, S. C. B.; Salleo, A.; Spano, F. C. Anisotropic Polaron Delocalization in Conjugated Homopolymers and Donor–Acceptor Copolymers. *Chem. Mater.* **2019**, acs.chemmater.9b01704.

(42) Clark, J.; Chang, J. F.; Spano, F. C.; Friend, R. H.; Silva, C. Determining Exciton Bandwidth and Film Microstructure in Polythiophene Films Using Linear Absorption Spectroscopy. *Appl. Phys. Lett.* **2009**, *94* (16), 3–6.

(43) Hexemer, A.; Müller-Buschbaum, P. Advanced Grazing-Incidence Techniques for Modern Soft-Matter Materials Analysis. *IUCrJ* **2015**, *2*, 106–125.

(44) Rivnay, J.; Mannsfeld, S. C. B.; Miller, C. E.; Salleo, A.; Toney, M. F. Quantitative Determination of Organic Semiconductor Microstructure from the Molecular to Device Scale. *Chem. Rev.* **2012**, *112* (10), 5488–5519.

(45) Scholes, D. T.; Hawks, S. A.; Yee, P. Y.; Wu, H.; Lindemuth, J. R.; Tolbert, S. H.; Schwartz, B. J. Overcoming Film Quality Issues for Conjugated Polymers Doped with F4TCNQ by Solution Sequential Processing: Hall Effect, Structural, and Optical Measurements. *J. Phys. Chem. Lett.* **2015**, *6* (23), 4786–4793.

(46) Bredas, J. L.; Street, G. B. Polarons, Bipolarons, and Solitons in Conducting Polymers. *Acc. Chem. Res.* **1985**, *18* (10), 309–315.

(47) Cook, J. B.; Lin, T. C.; Kim, H. S.; Siordia, A.; Dunn, B. S.; Tolbert, S. H. Suppression of Electrochemically Driven Phase Transitions in Nanostructured MoS2 Pseudocapacitors Probed Using Operando X-Ray Diffraction. *ACS Nano* **2019**, *13* (2), 1223–1231.

Chapter 5. Controlling Co-assemblies of Amphiphilic Polymers and Small Molecule Acceptors that Facilitate Excited-State Electron Transfer

5.1 Introduction

Photoinduced electron transfer (PET) has many applications including catalysis, water splitting, and organic photovoltaics (OPVs), to name a few.[1–4] For PET to occur, the optically accessible excited state of the electron donor must be aligned with a low-lying unoccupied molecular orbital on the electron acceptor so that electrons can transfer from the photoexcited donor to the acceptor. Excitons created on the donors after absorbing light can charge separate to pass the excited electron to the acceptor, leaving behind a positively-charged hole on the donor.

Biological photosynthesis is a representative PET system. The precise packing of acceptor molecules around the primary porphyrin-based electron donor enables charge separation with near unity quantum yield.[5] Inspired by this incredibly efficient natural process, researchers have made tremendous progress in mimicking many aspects of photosynthesis by building charge-transfer complexes based on small light-absorbing molecules.[6,7] Although many of these systems can achieve efficient charge transfer, there are two main drawbacks. First, small-molecule charge-transfer complexes have a limited number of accessible crystal structures, so the relative orientations of the donor and acceptor are hard to control. For example, co-crystals of tetrathiafulvalene (TTF) and tetracyanoquinodimethane (TCNQ) need to have segregated stacking to have high conductivity, but many crystallization conditions produce mixed stacking complexes.[8] In addition, some small-molecule charge-transfer complexes produce integer charge transfer while others only yield fractional charge transfer, further complicating matters.[9] Second, small-molecule charge-transfer systems often have low charge transport efficiency after charge separation due to the lack of an extended charge carrier propagation network. This means that the electron will often

transfer back to the donor molecule, resulting in charge recombination.[10] Natural photosynthesis avoids this problem by utilizing a membrane that both facilitates long-range electron transfer and provides structural connectivity to the various active components.[11,12]

One route to achieving similar success in artificial photosynthetic systems without a membrane is to design one of the charge-transfer components as a matrix that simultaneously acts as an electron donor (or acceptor), structure director, and charge transport medium. The idea is to provide a network where the electron transfer direction is different from the charge propagation direction, which can mitigate photogenerated carrier recombination losses. Examples of such donor matrices include carbon nanotubes and graphene,[13,14] semiconducting polymers,[15–17] and organogelator materials.[18] Among these materials, semiconducting polymers are particularly interesting due to their synthetically tunable extinction coefficients, narrow band gaps, and broad absorbance spectra.[19–21] The charge transfer direction at a polymer donor/acceptor interface is typically away from the polymer backbone, while the charge propagation direction is along the backbone.[22,23]

Because of this anisotropy in the charge transfer and propagation directions and because they are solution processable, tunable and low-cost, semiconducting polymers have already been successfully used as PET donors in various optoelectronic fields, such as organic photovoltaics (OPVs).[24–26] For OPVs, a semiconducting polymer is usually paired in a so-called bulk heterojunction (BHJ) with an organic acceptor such as a fullerene derivative.[17,27] After PET occurs at the donor-acceptor interface, the separated charges transverse the polymer or the acceptor network and are eventually extracted to generate current.[28] One issue with BHJ-based devices is that it is difficult to control or even characterize the morphology of the interpenetrating BHJ network, which makes it hard to find the specific molecular conformations that enhance device

efficiency. One of the goals of this paper is to explore ways to control not only the polymer donor structure but also the way the polymer packs with acceptors to understand the connections between specific molecular conformations and device efficiency.

Many groups have worked to control polymer structure and increase molecular order through methods such backbone and side-chain design,[29,30] increasing the overall crystallinity through enhanced π-stacking,[31,32] and straightening of polymer backbones via aligned nanopores or mechanical rubbing.[33,34] To control how polymers mix with acceptors, researchers have also developed methods including varying the solvents used for processing, annealing conditions, and utilizing processing additives, such as 1,8-diiodoctane, to tune the structure of the domains of the two components.[35–37] Clearly, additional methods that can precisely drive and control how semiconducting polymers co-assemble with acceptors are needed.

To provide exactly this type of control, we have synthesized and studied derivatives of two amphiphilic semiconducting polymers, poly(fluorene-alt-thiophene) (PFT) and poly(cyclopentadithiophene-alt-thiophene) (PCT), whose chemical structures are shown in Figure 5.1.[38,39] These two amphiphilic polymers are conjugated polyelectrolytes that consist of a conjugated backbone with side-chains containing two charged ammonium groups per fluorene or cyclopentadithiophene unit. These polymers were designed such that in polar solvents such as water, the hydrophobic backbones self-assemble into cylindrical micelles with the charged side chains interacting with the polar solvent. The controlled and ordered assembly of these polymers into micelles provides an appropriate platform with which to study PET with various electron acceptors.

In previous work, we used PFT as a conjugated polyelectrolyte scaffold for co-assembly with charged fullerene derivates to facilitate PET. PFT form highly ordered and extended polymer

micelle in water. In turn, the ordered solution-phase assemblies enabled precise positioning of the acceptors, leading to the formation of long-lived polarons upon photoexcitation.[40] Because of the similarity in chemical structure between PFT and PCT,[39] we expect that PCT should also form similar assemblies with electron acceptors such as charged fullerenes.

In this work, we further explore the co-assembly process between ordered semiconducting polyelectrolytes with different acceptors. We exploit subtle differences in the micelle geometry of PFT and PCT, the use of acceptors with different shapes and thus different propensities to co-assemble, and different processing conditions to control the co-assembled structures and thus excited-electron transfer. Our choice of the two self-assembled semiconducting polymers is based on the fact that PCT makes straighter micelles than PFT.[39] We then co-assemble these polyelectrolytes in aqueous solution with amphiphilic electron acceptors that are both flat, based on perylenediimide (PDI), and spherical, based on fullerenes (Figure 5.1) and study the structures of the co-assemblies via small-angle X-ray scattering (SAXS). We show via photoluminescence (PL) quenching that more loose and disordered polymer micelles can form similar co-assemblies independent of the acceptor shape. In contrast, more tightly ordered polymer micelles co-assemble with flat acceptors much more easily than spherical ones. We also show that after the initial co-assembly, solvent annealing can be used to drive additional acceptors, which were previously excluded due to size constraints, into the polymer micelle structure. Overall, by manipulating the way semiconducting polyelectrolytes form micelles, we are able to probe the structural factors that influence excited-state electron transfer and provide insight into their systematic design of artificial photosynthetic systems.

5.2 Experimental and Methods

Materials and Sample Preparation.

Synthetic details and characterization of PDI**1** (Figure 5.1) can be found in the supporting information. PFT, PCT and $C_{60}(PyI)_2$ (Figure 5.1) synthesis methods are in previous work.[39–41]

The various polymer solutions were made by weighing the polymer powders into vials and stirring into water. Co-assembled solutions were made by first dissolving the polymer in water prior to directly adding the acceptor powders. All reported polymer/acceptor ratios are by mass. Note that the two acceptors have similar molecular weight (PDI**1** Mw: 751.2, $C_{60}(PyI)_2$ Mw: 624.3), so that co-assemblies with these acceptors have a similar mole-ratio when they have the same mass ratio. Tetrahydrofuran (THF) annealing was performed by adding a volume of THF equal to ¼ the volume of the original solution and then stirring overnight before slowly heating to 80 °C to evaporate the THF. All sample preparations with PCT were done in air-free conditions to avoid PCT degradation in air. Since PFT does not degrade in air, the PFT experiments were performed under ambient conditions.

Spectroscopy Measurements.

UV-Visible absorption spectra were acquired using a Shimadzu UV- 3101PC UV-VIS-NIR Scanning Spectrophotometer for both solutions and films. PL measurements were carried out using a Jobin Yvon Horiba Fluorolog-3 spectrofluorometer using a front-face geometry for collecting the emission. Spectroscopic measurements on solutions were performed in a quartz cuvette with a 1-mm path length.

Solution SAXS.

Solution SAXS data were collected at the Stanford Synchrotron Radiation Laboratory (SSRL) using beamline 4-2. Solutions were loaded in a quartz capillary and held at room temperature. The scattering X-rays (12 keV) were collected using a 2-D detector and radially averaged to obtain 1-D data. *P*(*r*) plots were obtained using the GNOM software from EMBL. The smoothed *P*(*r*) data was used for bead modeling, using DAMMIN, a Monte Carlo-based modeling software. The parameters for the DAMMIN bead modeling can be found in the supporting information.

Cyclic Voltammetry (CV).

CV for PCT and PFT were measured in propylene carbonate with Li/Li^+ as the reference electrode and ITO glass as the working electrode, with the counter and reference electrodes being lithium metal.

5.3 Results and Discussions

Structure of Self-Assembled PFT and PCT Micelles in Water

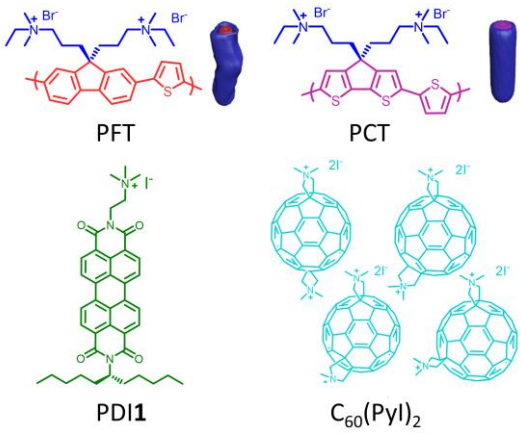

Figure 5.1: Molecular structure of poly(fluorine-alt-thiophene) (PFT), poly(cyclo-pentadithiophene-alt-thiophene) (PCT), charged perylenediimide (PDI**1**) and charged fullerenes ($C_{60}(PyI)_2$).

A critical part of our design rules for controlling the polymer and acceptor co-assemblies lies in controlling the chemical structure of the individual components.[38–40] PFT and PCT are both amphiphilic polymers that contain hydrophobic conjugated backbones and hydrophilic quaternized ammonium side chains branched off a sp^3 carbon, shown in **Error! Reference source not found.**. This tetrahedral site forces the side chains away from the backbone, resulting in a "pie-wedge" shape for each polymer chain. The individual chains assemble in water into cylindrical micelles, with the backbone forming the length of the micelle and the side chains forming a hydrophilic sheath around the conjugated backbone. Since the backbone runs the length of the

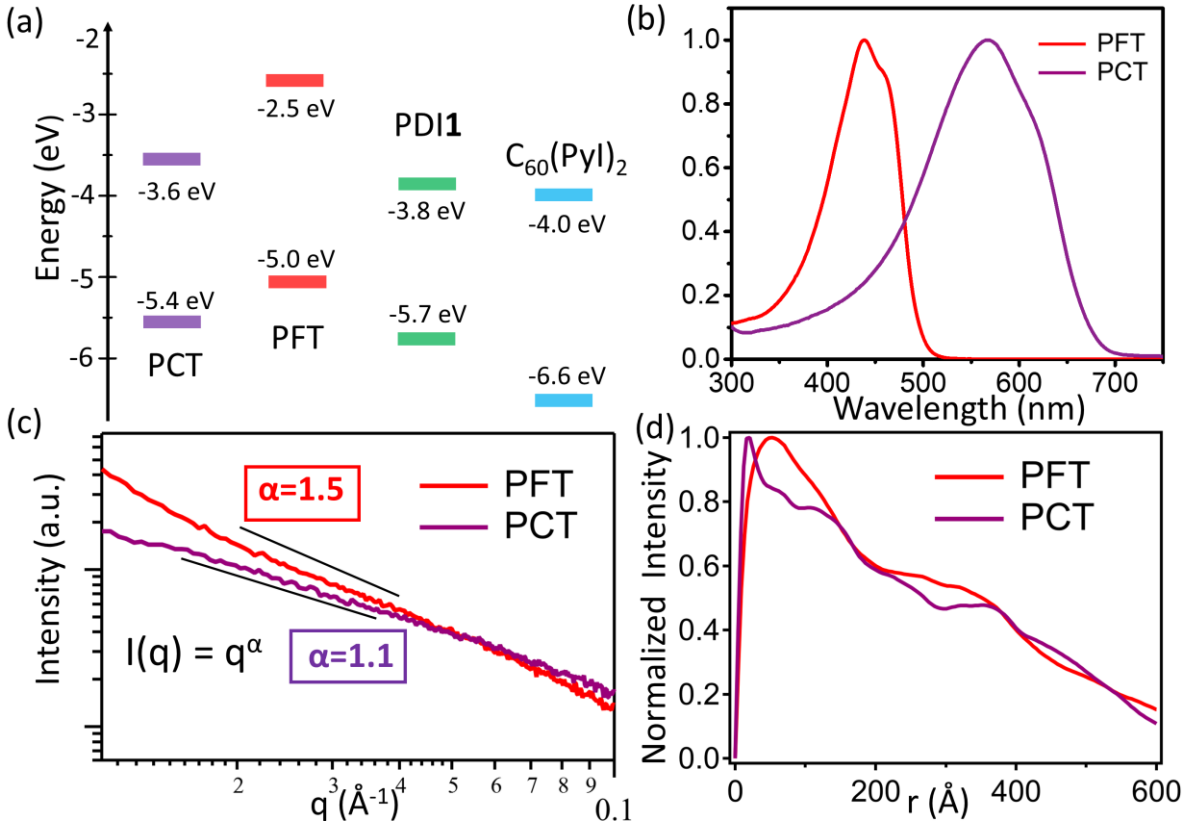

Figure 5.2: (a) Energy levels of PCT, PFT, PDI1 and $C_{60}(PyI)_2$. Excited electron transfer between the polymers and acceptors is possible given their LUMO levels, (b) Absorbance of PCT and PFT. PCT absorbs at a wider visible light range than PFT, (c) Solution SAXS of PCT and PFT in water. The power law fit of the curves show that PCT forms a straighter, cylindrical micelle compared to PFT. (d) Fourier transform of the SAXS data in (c). Both PCT and PFT shows a cylinder shape profile, but PCT has a smaller micelle diameter.

micelle, its geometry determines the longitudinal shape of the micelle. PFT and PCT are both alternating co-polymers containing thiophene and three-fused ring monomer units. The cyclopentadithiophene and thiophene subunits in PCT have little steric restriction to rotation, in contrast to the sterically clashing hydrogens in the fluorene/thiophene units of PFT; this should lead to an overall straighter polymer backbone for PCT.[39] This results in PCT forming straighter, tighter micelles relative to PFT (Figure 5.1 cartoon).

Optical spectroscopy of the two polymers in aqueous solution are shown in Figure 5.2b. The bandgap of PCT is shifted to longer wavelengths by about 170 nm in comparison to PFT. Thus, in addition to creating a straighter, tighter micelles, switching the fluorene unit in PFT with a cyclopentadithiophene unit in PCT also causes the polymer to absorb more of the visible spectrum.

Solution SAXS allows for quantitative determination of the shape and size of solution-phase assemblies.[42,43] The raw scattering curves are shown in Figure 5.2c. These curves appear relatively featureless, but fitting the raw data to a power law in the Guinier region can be used to extract the polymer fractal structure in solution. The slope of the fit indicates the dimensionality of the object: a slope of 1 indicates a rigid rod or cylinder, a slope of 2 indicates a flat disk, and a slope of 3 indicates a spherical structure.[44,45] Interactions or fluctuations between different structures will result in deviations in the slope from the ideal integer values. In the case of cylinders, deviations from a slope of 1 indicate either branching or bending, a sign of less linear rods.

Figure 5.2c shows the raw solution SAXS data for the two conjugated polyelectrolytes. The Gunier region of PCT can be fit to a power-law slope of nearly 1, whereas that of PFT has a slope of 1.5, which is consistent with our previous work.[39,40] This indicates that PCT forms a nearly straight, perfect cylinder in solution, while PFT is more disordered and bent, as predicted based on

the expected rigidity of their respective backbones. Fourier transformation of the raw solution SAXS data from Figure 5.2c gives pair-distance distribution functions, $P(r)$, which are used to correlate the structure of the scattering object by presenting the distribution of electron densities as a function of the separation distance, r.[46,47] The combination of a peak at lower r followed by a linear decay is the $P(r)$ signature of a cylindrical structure; the peak at lower reflects the cylinder's diameter while the intersection with x axis indicates the cylinder's length. PCT shows a narrower peak at lower r than PFT, indicating that PCT forms tighter cylindrical micelles (Figure 5.2d). But despite this difference, the data make clear that both amphiphilic polymers form cylindrical

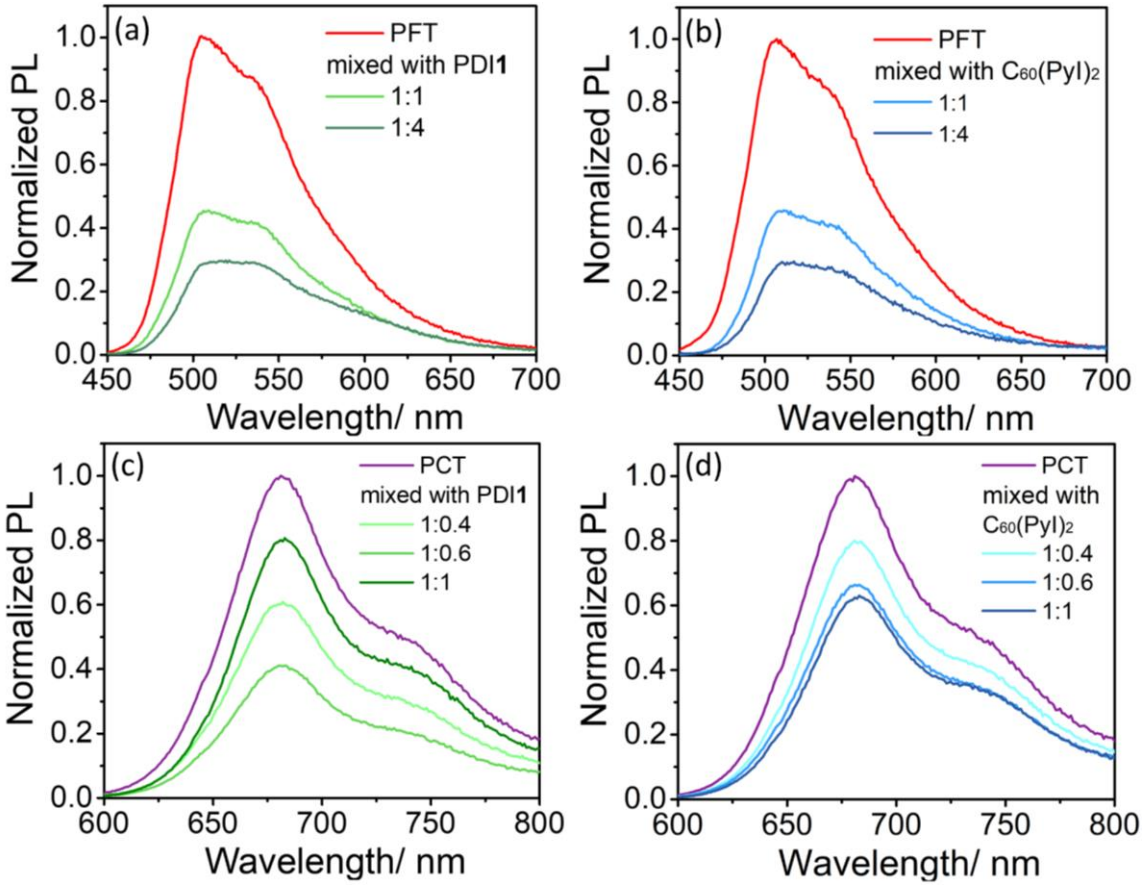

Figure 5.3: PL spectrum of (a) PFT and PDI1, (b) PFT and $C_{60}(PyI)_2$, (c) PCT and PDI1, and (d) PCT and $C_{60}(PyI)_2$. PDI1 and $C_{60}(PyI)_2$ quench PFT PL similarly, but quench PCT PL differently due to complementary micelle and acceptor geometry. PDI1 is a better fit for PCT micelle than PFT, thus quench PCT at lower acceptor ratios. $C_{60}(PyI)_2$, however, does not fit in PCT well as compared with PFT due to the size and shape constraint.

micelles, so both can be used as a scaffold for studying co-assembly and photoinduced charge transfer.

Spectroscopy and Structure of Co-Assembled Polymers and Acceptors

To probe the effect of electron acceptor structure on co-assembly with our polymer donor cylindrical micelles, we synthesized two acceptors with drastically different shapes but similar LUMO levels (cf. Figure 5.2a). PDI**1** is a relatively small, flat acceptor with a singly-charged side chain (Figure 5.1). Similar to PFT and PCT, PDI**1** contains an ammonium side chain on one end, but it also has a long-branched alkyl side chain on the opposite end to help prevent self-aggregation (Scheme S1, Figures S1-S6). The opposing hydrophilicity of these side chains makes PDI**1** amphiphilic. The other electron acceptor is $C_{60}(PyI)_2$, a mixture of four bis-pyrrolidium functionalized fullerenes, with the placement of the two rings on each fullerene resulting in trans-like or cis-like adducts (Figure 5.1). The trans-like and cis-like adducts prefer to sit in different parts of the polymer micelles, and we have previously used such adducts to study photoinduced charge transfer with PFT.[40] It is worth noting that $C_{60}(PyI)_2$ is poorly water soluble on its own (Figure S9f), while PDI**1** forms aggregates in water that also have limited solubility (Figure S9c). Thus both acceptors require the amphiphilic polymers to drive their co-assembly in water.

The energy levels of PCT, PFT, PDI**1** and $C_{60}(PyI)_2$ are shown in Figure 5.2a. The HOMO levels of PCT and PFT were determined via CV (Figure S7, 8), and LUMO levels for PCT and PFT were calculated based on the measured HOMO levels and the optical bandgap in Figure 5.2b. The LUMO levels of $C_{60}(PyI)_2$ and PDI**1** are taken from published work.[40,48] Based on the energy levels shown in Figure 5.2a, both polymers should be able to undergo PET with both acceptors. Since both polymers are also quite luminescent, we can therefore use PL quenching as an indirect

method of assessing how well these assemblies are structured for promoting photoinduced charge transfer.

Our PL quenching studies begin by mixing each polymer with each acceptor at matching molar ratios to explore the effect of both acceptor shape and concentration. For ease of comparison, we normalized the measured PL spectra to that of the polymer without any acceptor polymer PL intensity to better show the degree of quenching (the corresponding absorption spectra are shown in Figures S9). The PL quenching of PFT mixed with PDI**1** (Figure 5.3a**)** and mixed with $C_{60}(PyI)_2$ (Figure 5.3b) are identical, with the same acceptor concentration dependence. In contrast, the PL of PCT is quenched ≥ 20% more with PDI**1** (Figure 5.3c) than with the same ratio of $C_{60}(PyI)_2$

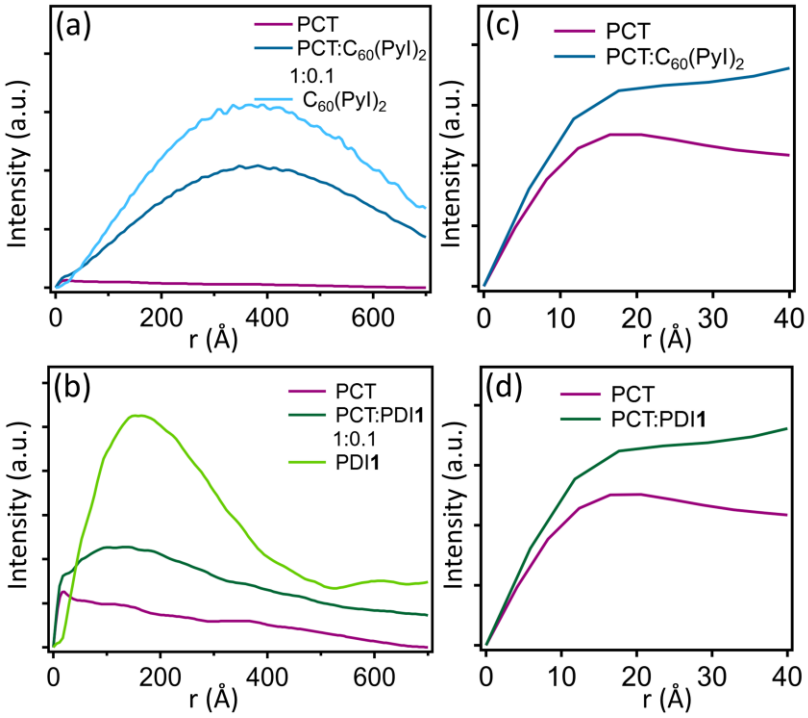

Figure 5.4: *P(r)* curves of (a) PCT, PDI**1** and PCT with PDI**1**, (b) PCT, $C_{60}(PyI)_2$ and PCT with $C_{60}(PyI)_2$. Both PDI**1** and $C_{60}(PyI)_2$ intensity decrease when mixed with PCT than alone, indicating the co-assembly with the polymer. PDI**1** intensity decrease more in the co-assembly compared with $C_{60}(PyI)_2$ because PDI**1** forms more complementary assemblies with PCT. (c) and (d) are zoomed in PCT micelle diameter correlation peak in (a) and (b). The unchanged peak position in the co-assemblies of both the acceptors demonstrates that the micelle structure is conserved after acceptor co-assembly.

(Figure 5.3d). This difference in quenching behavior must be due to structural differences between the PFT and PCT micelles. PCT forms a more defined and tighter micelle, which leaves smaller pockets of space to accommodate acceptors compared to the more disordered and looser micelles of PFT. Thus, the smaller and flatter PDI**1** can effectively co-assemble around the PCT micelle, whereas the spherical bulk of $C_{60}(PyI)_2$ cannot pack well into those same spaces. In contrast, the more disordered PFT micelles contain spaces that can fit PDI**1** and $C_{60}(PyI)_2$ equally well, so that both acceptors have similar abilities to quench PFT.

Figures 5.3a and 5.3c show that the degree of PL quenching of PCT with PDI**1** at a 1:0.6 ratio is similar to that of PFT with PDI**1** at a 1:1 ratio. This suggests that PDI**1** fits better in the tight PCT micelles than in the looser PFT micelles. We also see that further increasing PDI**1** ratio (1:1) does not lead to additional quenching of the PCT PL (Figure 5.3c). This is because PDI**1** can aggregates in water (Figure S9c), so that at high concentrations, PDI**1** forms soluble self-aggregates that are too large to fit into a tight PCT micelle. PFT, on the other hand, has many fewer space constraints for aggregates of PDI**1**. This idea also fits what the PL quenching observed with $C_{60}(PyI)_2$, which is much less soluble in water compared with PDI**1** (Figure S9c, f) and thus needs to form co-assemblies with the polymers to dissolve. With PCT, $C_{60}(PyI)_2$ does not provide any additional quenching at higher acceptor ratio simply because there is no room for any additional acceptor in the tight PCT micelle (Figure 5.3d). PFT has more space to incorporate large spherical acceptors, so at high acceptor ratios, $C_{60}(PyI)_2$ can co-assemble with and quench PFT's PL better than PCT's.

It is worth noting that due to the overlap of the PDI**1** absorption and the PFT emission spectra, PL quenching for this donor/acceptor combination might also be caused by resonant energy transfer. Energy transfer should not be possible between PCT and PDI**1** because PCT's

absorption spectrum is too red, and energy transfer also should not be possible from either polymer to $C_{60}(PyI)_2$, since the latter does not absorb in the visible region. We believe that energy transfer between PFT and PDI**1** plays at most a minor role in the observed PL quenching for several reasons. First, energy transfer requires fairly strict conditions for the orientation of the donor and acceptor transition dipole orientations,[49] and the loose micelle structure of PFT is unlikely to hold the chromophores rigidly in the best orientation for energy transfer. Second, we see that at the same PDI**1** concentration, PFT is quenched less than PCT. If both energy and electron transfer were taking place between PFT and PDI**1**, we would expect greater PL quenching for this combination instead of less. Finally, even if some of the quenching were due to energy transfer, the energy level diagram in Figure 5.2 shows that hole transfer can readily take place between excited PDI**1** and PFT, so the net result of any PL quenching event will still be photoinduced electron transfer.

To confirm our picture of space in the different polymer micelles controlling the nature of the co-assembly and thus degree of PET and therefore PL quenching, we turn to solution SAXS to quantify the structural changes that take place in our donor/acceptor co-assemblies. In our previous work, we found that PFT co-assembled with $C_{60}(PyI)_2$ tightly without micelle structure deformation using solution SAXS. Due to the larger size and poorer water solubility of $C_{60}(PyI)_2$ compared with PDI**1**, we are confident to infer that PDI**1** can also insert into the PFT micelle. Thus, in this paper, we will only focus on the structure change of the newly synthesized polymer PCT. Figures 5.4a, b show the $P(r)$ curves for the pure PCT polymer (purple curves), pure acceptors (light blue, green curves) and PCT/acceptor co-assemblies (dark blue, green curves). Figures 5.4c, d show the lower r region of the same data as in Figure 5.4a, b but on an expanded scale to better show the peak representing the PCT micelle diameter. The peak position is unchanged after incorporating either of the two acceptors, indicating that the size of the micelle is determined

primarily by the polymer and not by the co-assembly. The correlation peaks at higher *r* in the co-assemblies matches those seen in the pure acceptor solutions (at about 180 Å for PDI**1** and centered at 400 Å for $C_{60}(PyI)_2$) and thus likely arises from acceptor aggregates that are not part of the co-assembly. In fact, when co-assembled with PCT, this correlation peak for both acceptors decreases in intensity, indicating the some of the acceptor self-aggregation is disrupted by co-assembly with the polymer, a trend that is greater for PDI**1** than $C_{60}(PyI)_2$. This provides another indication that PDI**1** co-assembles better with PCT than $C_{60}(PyI)_2$, as also suggested by the PL quenching. Together, all of the data affirms our hypothesis that co-assembly is determined by how well the acceptors fit into the pre-existing micelle network.

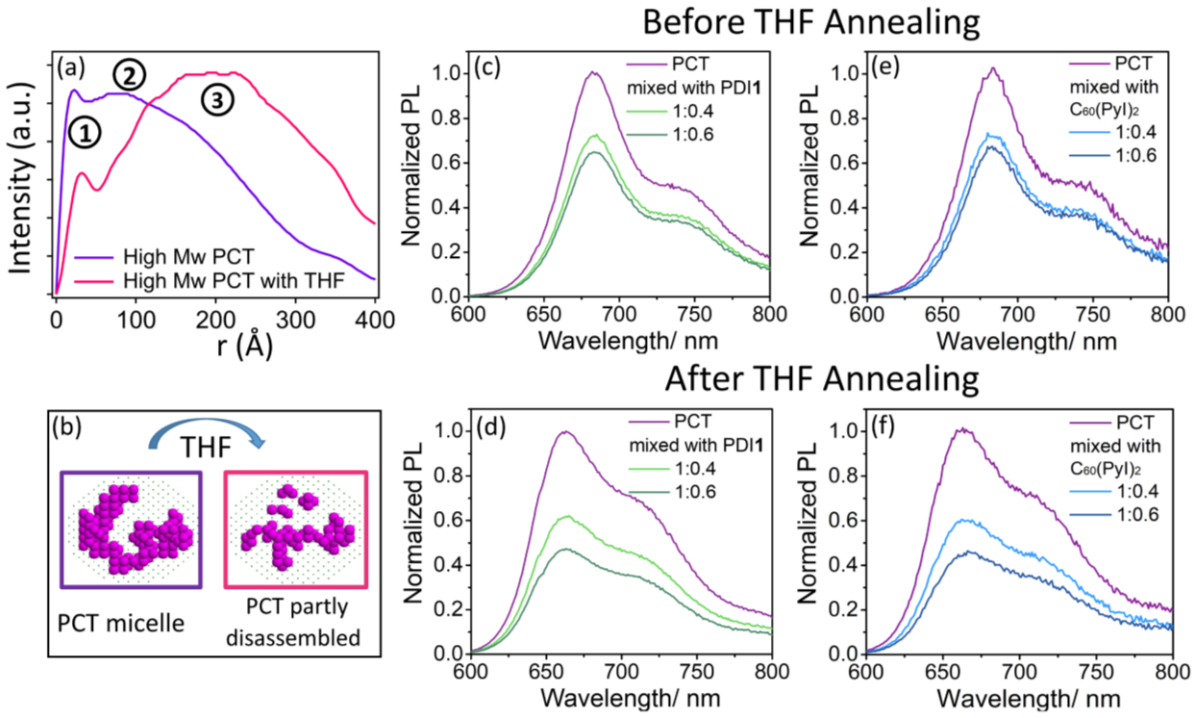

Figure 5.5: (a) *P(r)* of PCT without and with THF. Adding THF loosens the micelle structure and induces both intra- and inter-micelle interaction. (b) DAMMIN Beads modeling of PCT after adding THF shows a decrease in electron density. PL quenching spectrum of (c) PCT and PDI**1**, (d) PCT and PDI**1** after THF annealing, (e) PCT and $C_{60}(PyI)_2$, and (f) PCT and $C_{60}(PyI)_2$ after THF annealing. Consistent with the solution SAXS data, higher PCT concentrations are used so the PDI**1** ratios and quenching are less than those in Figure 5.3. THF annealing influence PFT PL quenching less than PCT due to the structural difference between PCT and PFT.

The Effects of Solvent Annealing on Co-Assembled Structures

Even though PCT forms highly ordered micelles, it has the potential drawback that the tight micelles are unable to accommodate acceptors of all shapes or sizes. In this section, we work to mitigate this drawback by using solvent annealing, which is a common method used to tune polymer morphology.[37,50–52] For PCT, the idea is that solvent annealing temporarily loosens the micelles, allowing acceptors to incorporate into the newly opened spaces. Prior work from our groups showed that aqueous PFT micelles solution were relaxed upon addition of tetrahydrofuran (THF), with the micelles becoming more robust after the THF was subsequently removed.[41] Thus, we performed a series of experiments solvent annealing PCT micelles with THF to allow co-assembly with larger electron acceptors, such as the bulky $C_{60}(PyI)_2$.

The purple curve in Figure 5.5a shows SAXS data indicating that PCT forms cylindrical micelles, where peak 1 corresponds to the micelle diameter and peak 2 reflects correlations from micelle curvature. Upon addition of THF to pre-assembled PCT micelles in water, the pink curve in Figure 5.4e shows that the intensity of peak1 decreases, while the intercorration peak becomes broader and shifts to higher *r*. This means that THF does not completely disrupt the PCT micelle structure, but instead creates a partly dissolved and more disordered micelle.[39] The structure of the partly dissolved micelles can be inferred using DAMMIN bead modeling to simulate the corresponding solution SAXS data.[51] Briefly, in this Monte-Carlo-based method, a set of beads, corresponding to electron density, are moved inside the simulation box until the simulated scattering profile of the structure matches the experimental scattering data. The result in Figure 5.5b shows that the compact cylindrical micelles in water evolve into more diffuse scattering structures with less electron density upon THF addition, verifying that THF partly dissolves and relaxes the polymer micelle structure.

This effect of THF relaxing the micelles can be seen via PL quenching. Figure 5.5c-f shows the PL quenching of PCT by the two acceptors before and after THF annealing (PL quenching percentage are shown in SI Table 3-5). By adding THF, we not only get more PL quenching with PDI**1**, showing increased incorporation, but we also get significant quenching with $C_{60}(PyI)_2$. Both of these observations show that THF annealing allows for increased incorporation. THF annealing has much smaller effect on PFT PL quenching by PDI**1** compared with PCT (Figure S11a, b). This indicates that THF annealing has limited effect on an already loose and disorder system and is more effective when the polymer system is too tight for acceptors to incorporate.

5.4 Summary

In summary, we have worked to elucidate the effects of how controlling the self-assembly of conjugated polyelectrolytes changes the efficiency of photoinduced charge transfer. To accomplish this, we studied aqueous co-assemblies of two amphiphilic donor polymers and two small-molecule acceptors. The two conjugated polymers form cylindrical micelles with slightly different structures, providing a platform to probe the effects of micelle geometry on co-assembly and charge transfer with differently-shaped molecular acceptors. When the polymer micelle is relatively loose, as with PFT, there is little selectivity for co-assembly with different acceptors, but the polymer backbones are not optimally arranged for long-range charge transport. with acceptor geometries. When the polymer micelle is tight and ordered, as with PCT, only acceptors with an appropriate geometry to fit with the more compact micelle can form co-assemblies. However, the geometric constraints on co-assembly can be overcome by solvent annealing, which relaxes the polymer micelle and creates more space for larger acceptor molecules. Overall, we were able to validate that control of co-assembly between semiconducting polymers and molecular acceptors can be tuned via the polymer micelle structure, which in turn can be controlled either by changing

the chemical structure of the polymer or by changing the assembled micelle structure through solvent annealing. All of this work highlights important design principles for creating next-generation artificial photosynthetic systems.

5.5 Supporting Information

Synthetic details

General procedures:

Chemical reagents were obtained from commercial sources and used without further purification. Unless otherwise noted, all reactions were performed under argon at 25 °C. Silicycle (Siliflash P60) silica gel 60 (240-400 mesh) was used for all column chromatography. NMR spectra were obtained on a Bruker AV500 instrument. 2,9-di(undecan-6-yl)anthra[2,1,9-def:6,5,10-d'e'f']diisoquinoline-1,3,8,10(2H,9H)-tetraone (1),[53] PFT,[38] the $C_{60}(PyI)_2$ charged fullerenes,[40] and PCT[39] were synthesized according to published procedures.

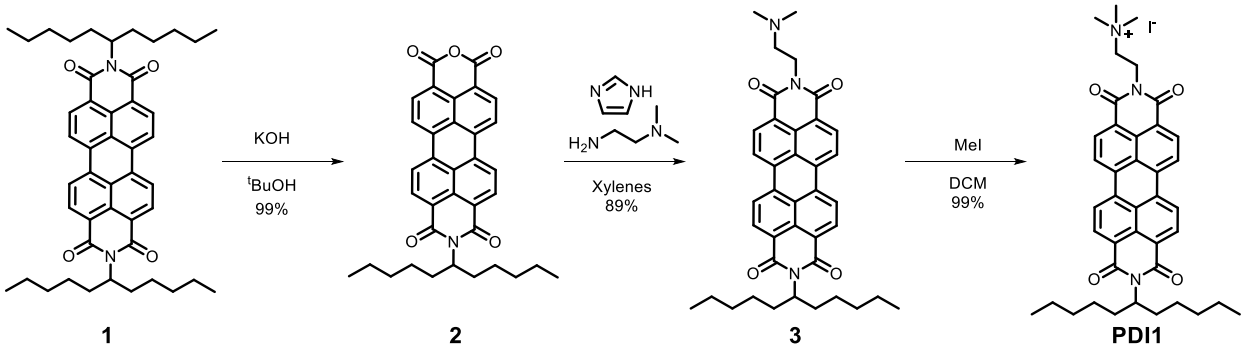

Scheme S1: Synthesis of PDI**1**.

9-(undecan-6-yl)-1H-isochromeno[6',5',4':10,5,6]anthra[2,1,9-def]isoquinoline-1,3,8,10(9H)-tetraone (2)

Compound **1** (1.000g, 1.432 mmol, 1.0 eq) was dissolved in tert-butanol (36 mL). Potassium hydroxide pellets (401 mg, 7.16 mmol, 5.0 eq) were added and the solution heated to 90 °C. After 1 hour, the reaction was checked by TLC and then poured into stirring glacial acetic acid (36 mL). This was allowed to stir for 2 hours at room temperature before 2N HCl (18 mL) was added and stirred for an additional 30 min. The mixture was then filtered and washed with H_2O until the filtrate was at neutral pH. The resulting red solid was then purified via column chromatography on silica gel using chloroform to chloroform with 10% acetic acid. 490 mg (63%) of the final compound was recovered. ^{1}H NMR (400 MHz, $CDCl_3$): δ (ppm) 8.69 (m, 8H), 5.18 (m, 1H), 2.23 (m, 2H), 1.86 (m, 2H), 1.27 (m, 12H), 0.83 (t, *J* = 4.7 Hz 6H); ^{13}C NMR (125 MHz, $CDCl_3$): δ (ppm) 160.0, 136.5, 133.6, 131.9, 129.5, 126.9, 126.6, 123.9, 123.2, 119.0, 54.9, 32.3, 31.7, 26.6, 22.6, 14.0; HRMS (DART) Calculated for $C_{35}H_{31}NO_5$ [M+H]: 545.22022; found 545.22104.

2-(2-(dimethylamino)ethyl)-9-(undecan-6-yl)anthra[2,1,9-def:6,5,10-d'e'f']diisoquinoline-1,3,8,10(2H,9H)-tetraone (3)

To a solution of compound **2** (481 mg, 0.882 mmol, 1.0 eq) in xylenes (2.0 mL) were added imidazole (481 mg, 7.66 mmol, 8.0 eq) and N,N-dimethylethylenediamine (0.145 mL, 1.32 mmol, 1.5 eq). The reaction was heated to 120 °C for 3.5 hours under argon. After cooling to room temperature, the mixture was poured into methanol (30 mL), sonicated and filtered. Purification by column chromatography in CH_2Cl_2 with 10% methanol and 2.5% trimethylamine afforded a red solid as the product (409 mg, 89%). ^{1}H NMR (400 MHz, $CDCl_3$): δ (ppm) 8.67 (d, *J* = 4.0 Hz, 4H), 8.61 (d, *J* = 2.4 Hz, 2H), 8.59 (d, *J* = 2.4 Hz, 2H), 5.19 (m, 1H), 4.37 (t, J = 6.9 Hz, 2H), 2.75

(t, J = 6.9 Hz, 2H), 2.40 (s, 6H), 2.25 (m, 2H), 1.87 (m, 2H), 1.26 (m, 12H), 0.83 (t, *J* = 6.9 Hz, 6H); ^{13}C NMR (125 MHz, $CDCl_3$): δ (ppm) 163.5, 134,8, 134.4, 131.5, 129.6, 129.5, 126.5, 126.4, 123.2, 123.0, 56.9, 54.8, 45.8, 45.6, 38.1, 32.3, 31.8, 26.6, 22.6, 14.1; HRMS (DART) Calculated for $C_{39}H_{41}N_3O_4$ [M+H]: 615.30971; found 615.30508.

N,N,N-trimethyl-2-(1,3,8,10-tetraoxo-9-(undecan-6-yl)-3,8,9,10-tetrahydroanthra[2,1,9-def:6,5,10-d'e'f']diisoquinolin-2(1H)-yl)ethan-1-aminium iodide (PDI1)

Compound **3** (409 mg, 0.665 mmol) was dissolved in CH_2Cl_2 (14 mL) and iodomethane (0.91 mL) was added. The solution was allowed to stir at room temperature before concentrating to yield the final compound (425 mg, 99%) as a red solid. ^{1}H NMR (400 MHz, d_6-DMSO): δ (ppm) 8.70 (t, *J* = 8.8 Hz, 4H), 8.45 (br, 2H), 8.38 (d, *J* = 3.9, 2H), 5.05 (m, 1H), 4.45 (t, *J* = 7.1 Hz, 2H), 3.64 (t, *J* = 7.1 Hz, 2H), 3.22 (s, 9H), 2.17 (m, 2H), 1.80 (m, 2H), 1.23 (m, 12H), 0.75 (t, *J* = 6.9 Hz, 6H); ^{13}C NMR (125 MHz, d_6-DMSO): δ (ppm) 163.2, 134.6, 131.3, 128.9, 125.8, 124.6, 122.6, 62.3, 55.4, 54.0, 53.0, 34.2, 32.1, 31.6, 26.5, 22.4, 14.4, 7.9.

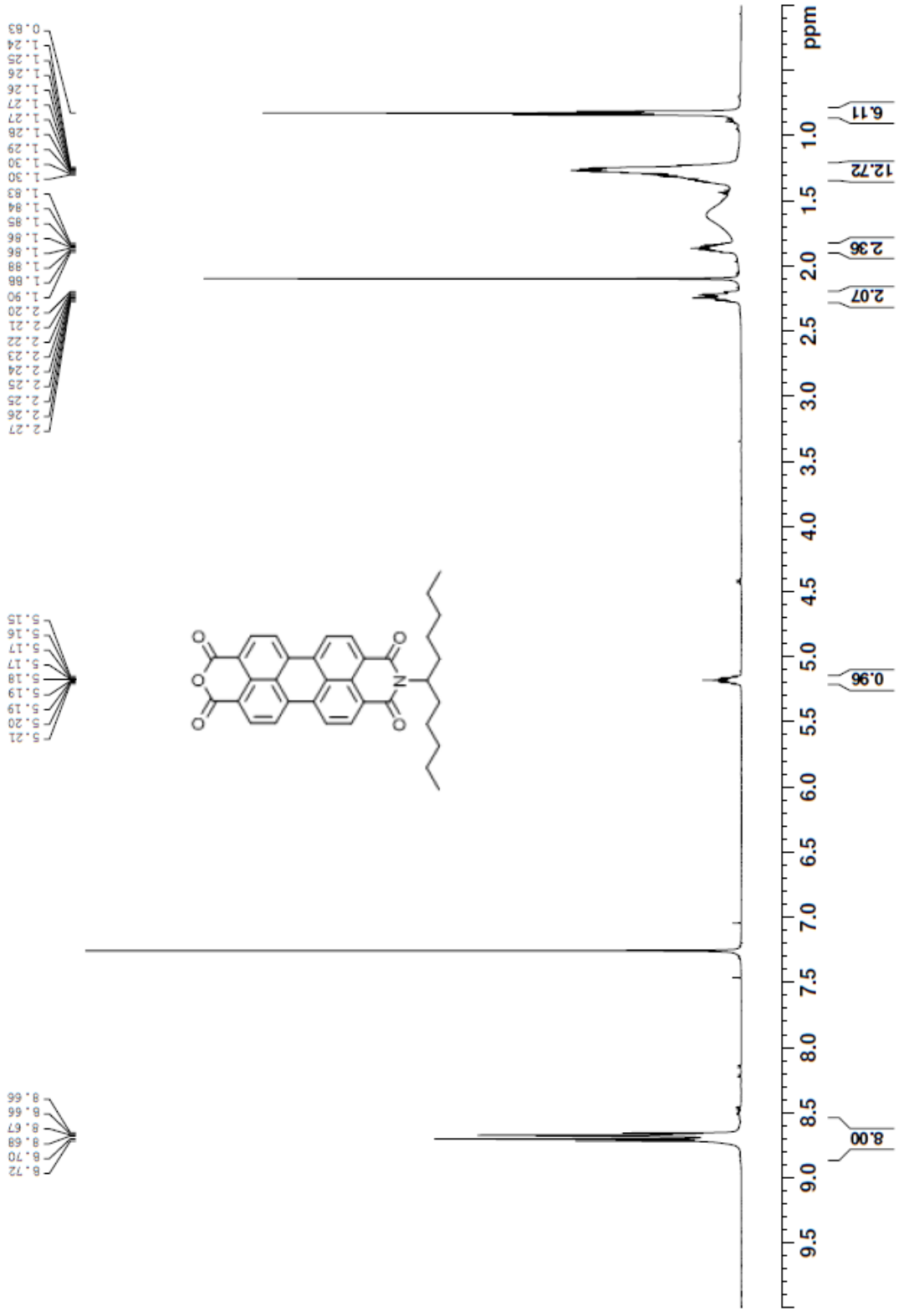

Figure S1: ^{1}H NMR spectrum of compound **2** in $CDCl_3$.

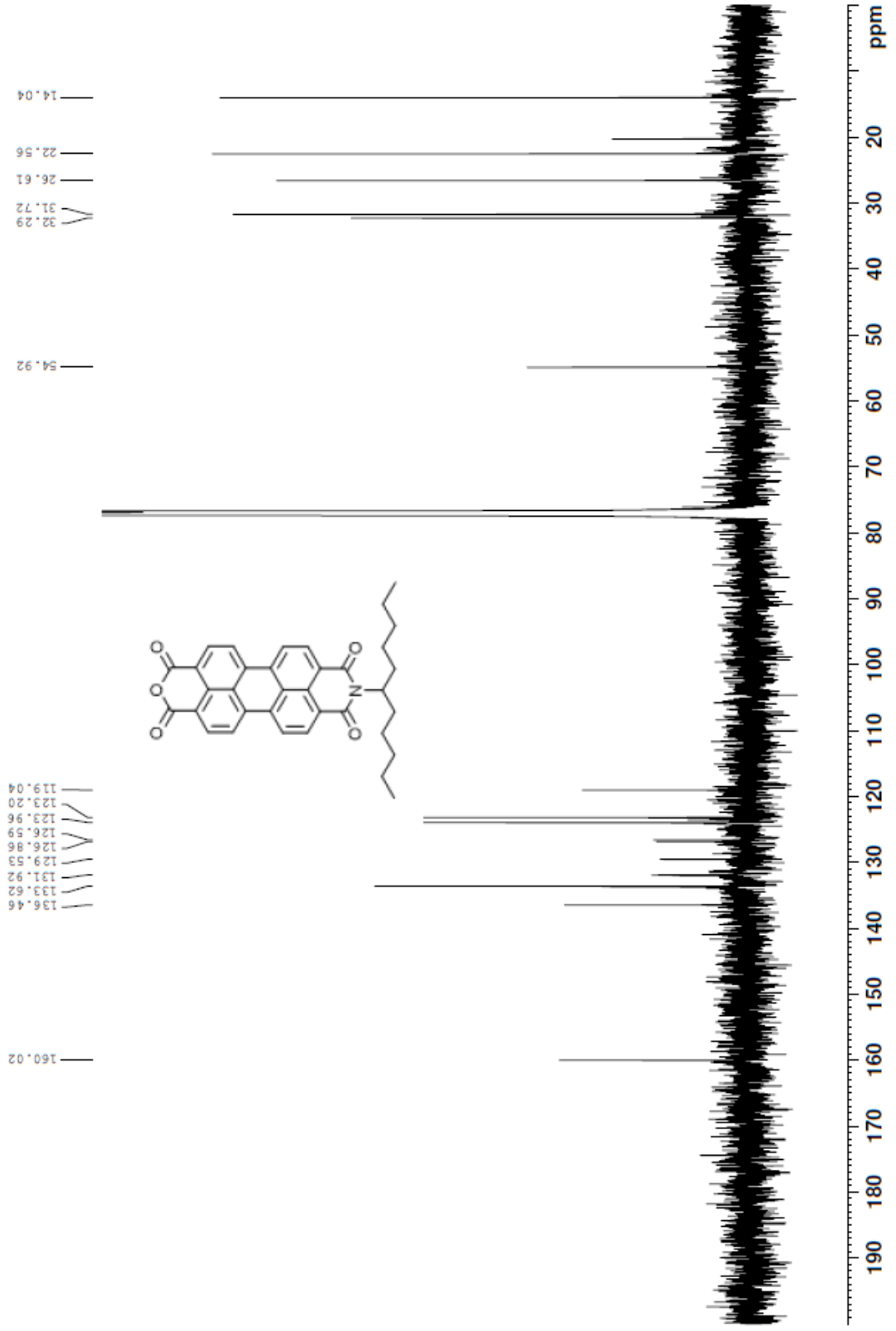

Figure S2: ^{13}C NMR spectrum of compound **2** in $CDCl_3$.

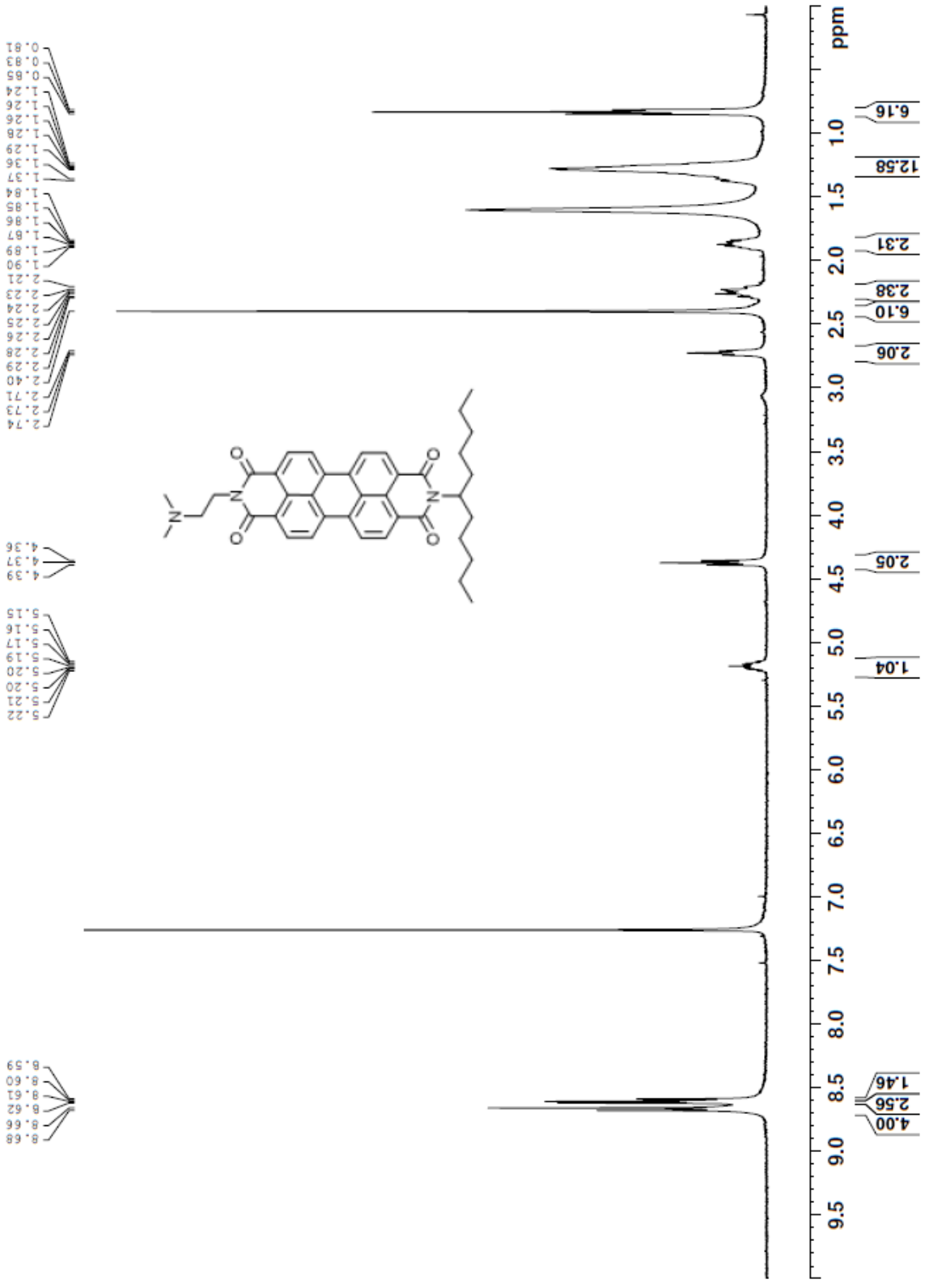

Figure S3: ^{1}H NMR spectrum of compound **3** in $CDCl_3$.

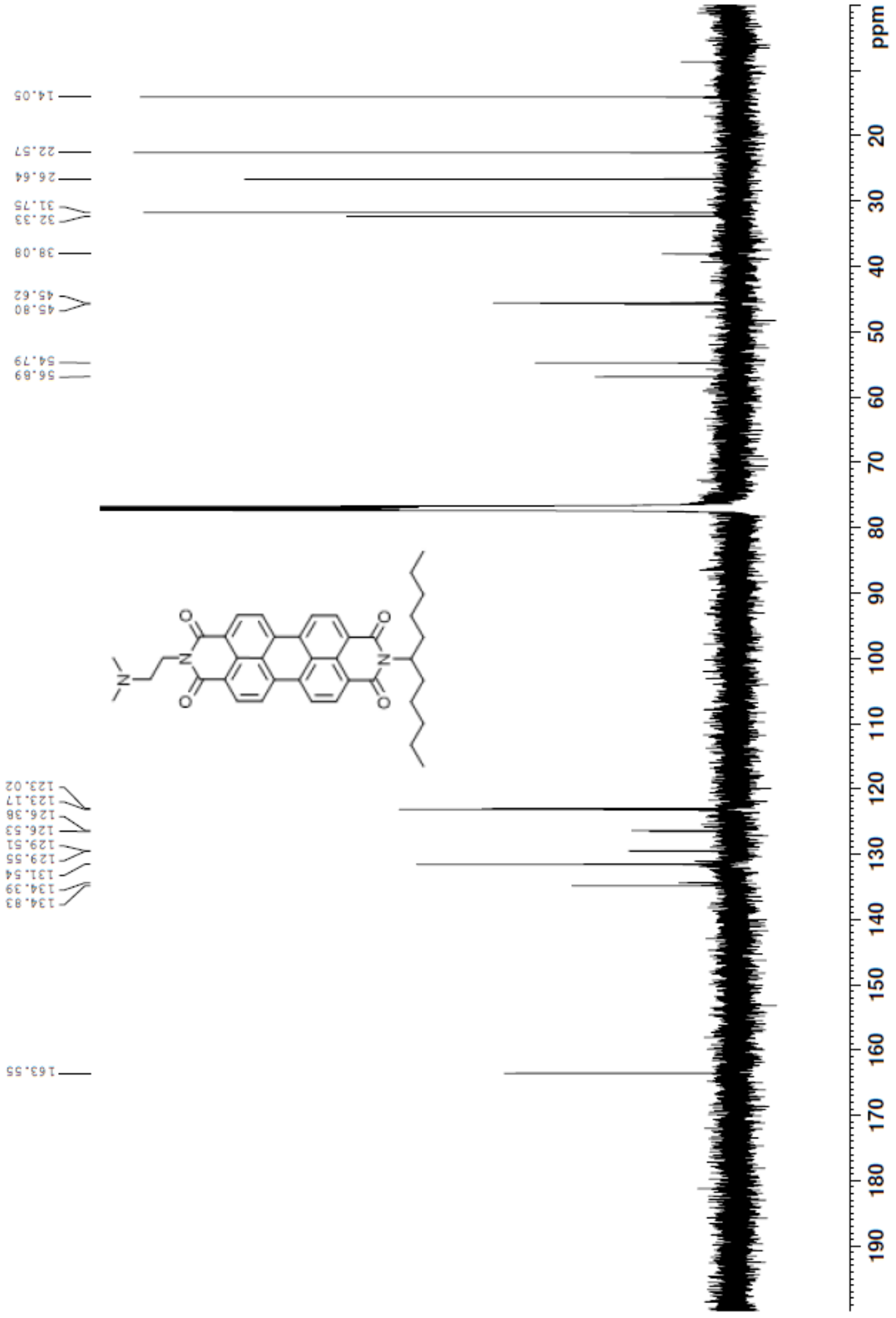

Figure S4: ^{13}C NMR spectrum of compound **3** in $CDCl_3$.

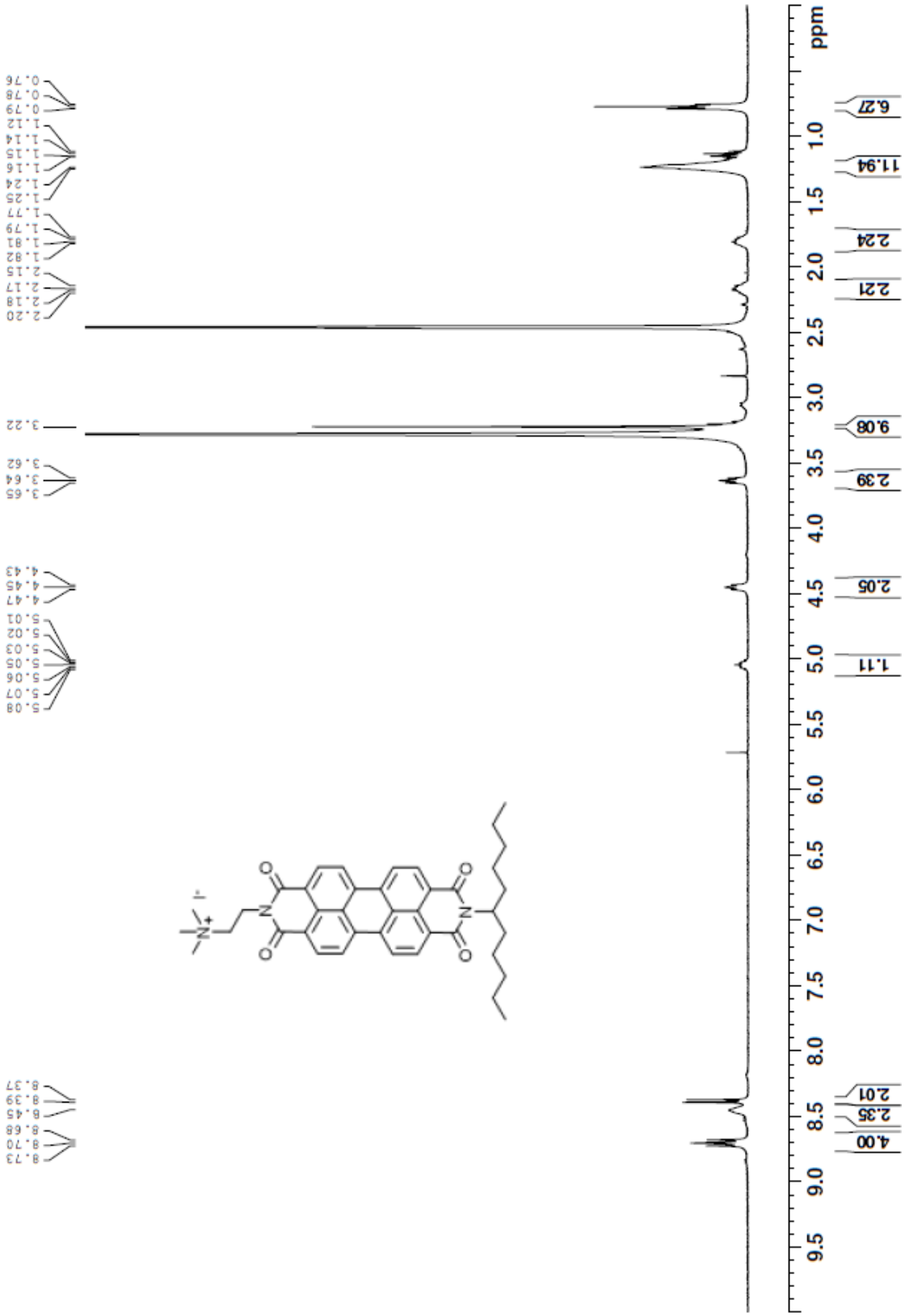

Figure S5: ^{1}H NMR spectrum of compound **PDI1** in d_6-DMSO.

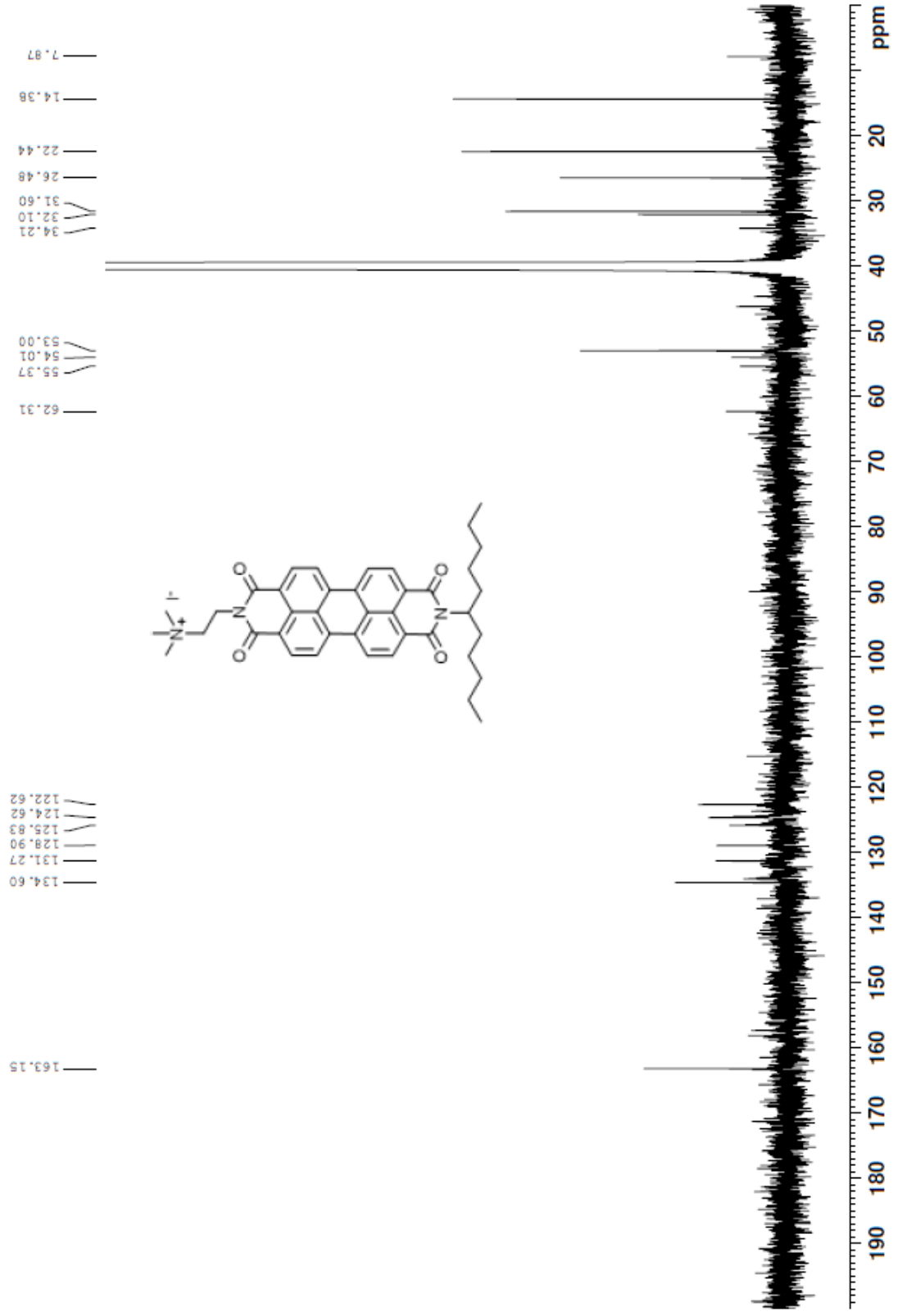

Figure S6: ^{13}C NMR spectrum of compound **PDI-1** in d_6-DMSO.

Cyclic Voltammetry (CV)

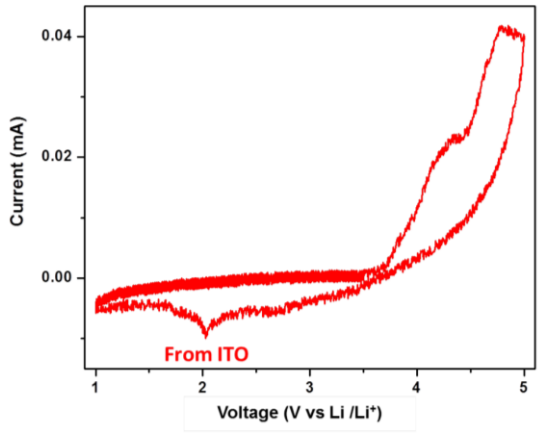

Figure S7: CV for PCT, measured in propylene carbonate with Li/Li^+ as the reference electrode and ITO glass as the working electrode using a sweep rate of 0.5 mV/s. PCT exhibits two irreversible oxidation peaks at 4.1 and 4.5 V vs. Li/Li^+. The reduction peak could not be measured, possibly due to the degradation of the polymer during oxidation. Absolute ionization potentials were calculated using –4.3 V as the absolute electrode potential for the standard hydrogen electrode and –3.0 V as the standard reduction potential of Li/Li^+ vs. the standard hydrogen electrode.

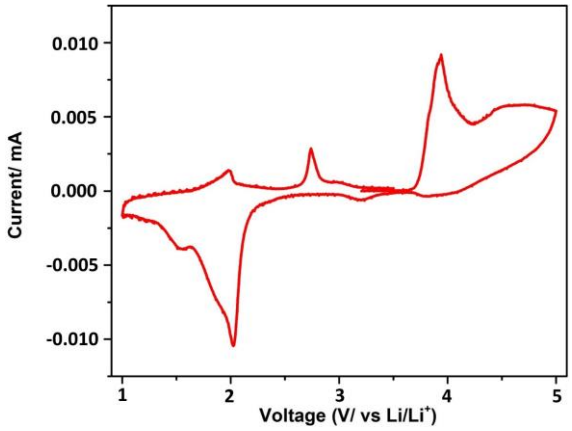

Figure S8: CV for PFT, measured in propylene carbonate with Li/Li^+ as the reference electrode and ITO glass as the working electrode using a sweep rate of 5 mV/s. PFT exhibits two irreversible oxidation peaks at 3.75 and 4.2 V vs. Li/Li^+. The reduction peak could not be measured, possibly due to the degradation of the polymer during oxidation. Absolute ionization potentials were calculated using –4.3 V as the absolute electrode potential for the standard hydrogen electrode and –3.0 V as the standard reduction potential of Li/Li^+ vs. the standard hydrogen electrode.

UV-Vis Spectroscopy

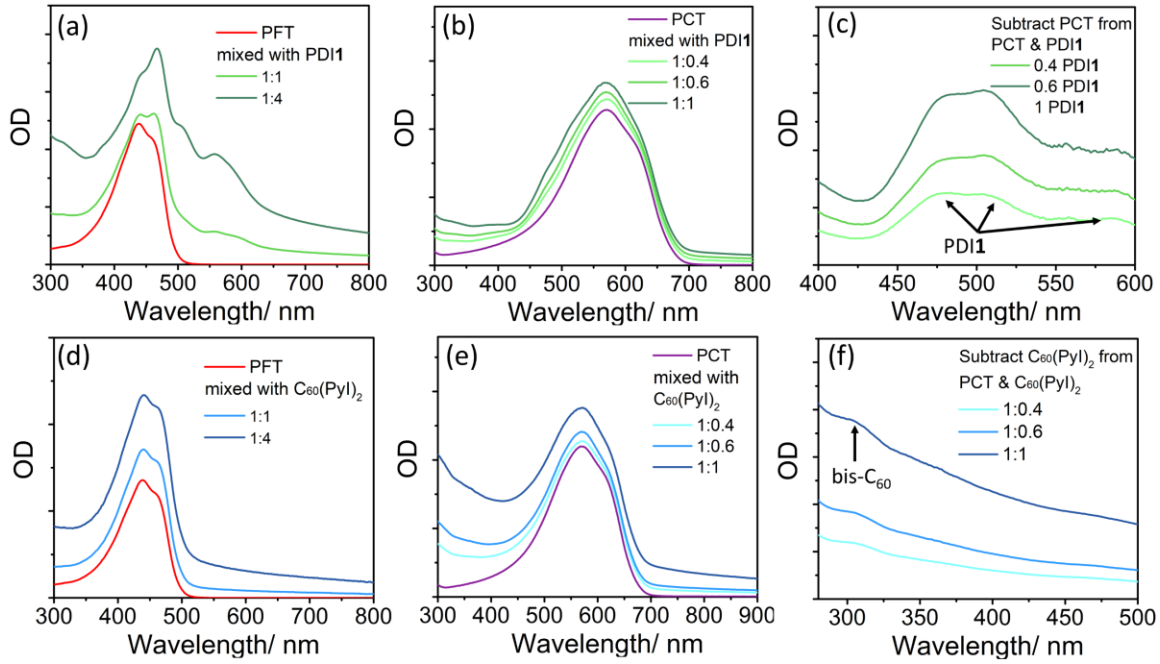

Figure S9: Absorbance of polymers with acceptors and only acceptors in water corresponding to Figure 5.2 in main text. (a) PFT with PDI**1**, (b) PCT with PDI**1**, (c) Subtract PCT from PCT&PDI**1** mixtures in panel b. PDI**1** dissolves in water and form aggregates with the arrows pointing to the absorbance peaks. (d) PFT with $C_{60}(PyI)_2$, (e) PCT with $C_{60}(PyI)_2$, and (f) Subtract PCT from PCT&$C_{60}(PyI)_2$ mixtures in panel e. $C_{60}(PyI)_2$ barely dissolve in water and only show a weak absorbance peak at around 300nm.

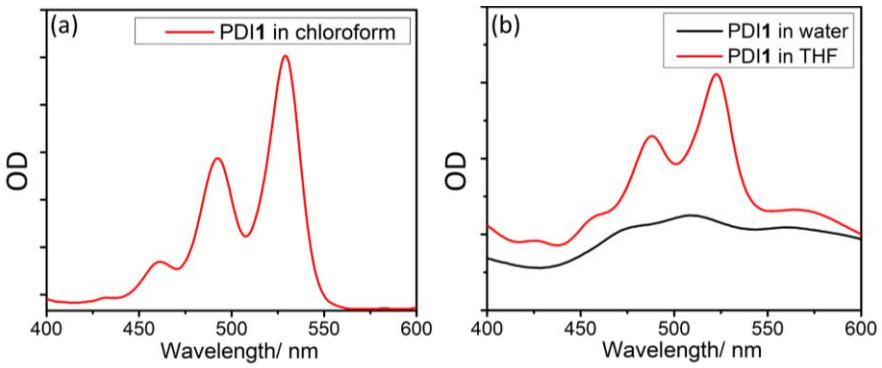

Figure S10: (a) Absorbance of **PDI1** in chloroform after filtration, showing the PDI**1** monomer absorbance. (b) Absorbance of **PDI1** in water (black) and in THF (red). THF is able to dissolve PDI**1** aggregates.

PL Spectroscopy

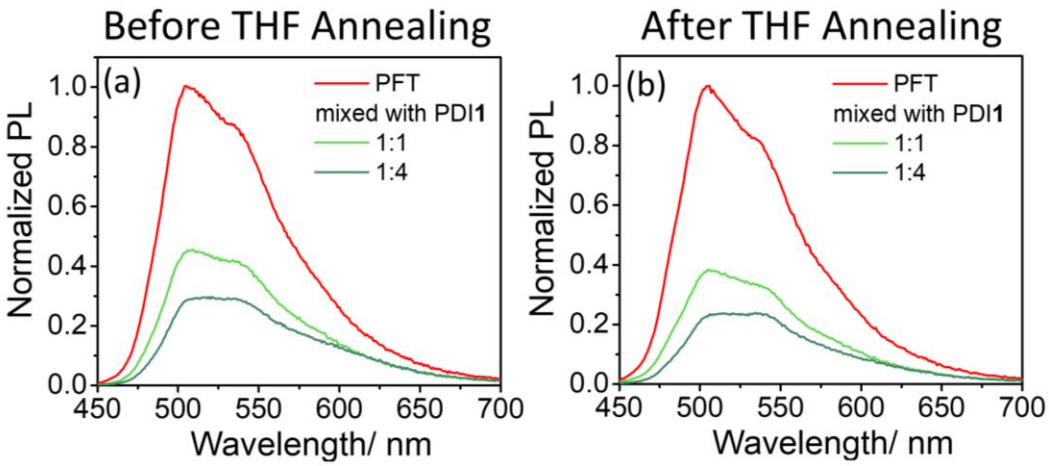

Figure S11: Normalized PFT PL quenched by PDI1 before (a) and after (b) THF annealing. PFT PL quenching by PDI1 does not show obvious change after THF annealing.

Table 1: Normalized PL quenching of PCT by different ratio of acceptors.

	PCT	0.4 PDI**1**	0.6 PDI**1**	1 PDI**1**	0.4 $C_{60}(PyI)_2$	0.6 $C_{60}(PyI)_2$	1 $C_{60}(PyI)_2$
Normalized PL	1	0.60	0.41	0.80	0.80	0.66	0.62

Table 2: Normalized PL quenching of PFT by different ratio of acceptors.

	PFT	1 PDI**1**	4 PDI**1**	1 $C_{60}(PyI)_2$	4 $C_{60}(PyI)_2$
Normalized PL	1	0.45	0.29	0.45	0.28

Table 3: Normalized PL quenching of PCT by PDI1 before and after THF annealing

	PCT	0.3 PDI**1**	0.5 PDI**1**	Annealed PCT	Ann 0.3 PDI**1**	Ann 0.5 PDI**1**
Normalized PL	1	0.72	0.64	1	0.62	0.47

Table 4: Normalized PL quenching of PCT by $C_{60}(PyI)_2$ before and after THF annealing

	PCT	0.3 $C_{60}(PyI)_2$	0.5 $C_{60}(PyI)_2$	Annealed PCT	Ann 0.3 $C_{60}(PyI)_2$	Ann 0.5 $C_{60}(PyI)_2$
Normalized PL	1	0.72	0.66	1	0.60	0.46

Table 5: Normalized PL quenching of PFT by PDI1 before and after THF annealing

	PFT	1 PDI**1**	4 PDI**1**	Annealed PFT	Ann 1 PDI**1**	Ann 4 PDI**1**
Normalized PL	1	0.45	0.29	1	0.38	0.24

5.6 References

(1) Sumliner, J. M.; Lv, H.; Fielden, J.; Geletii, Y. V.; Hill, C. L. Polyoxometalate Multi-Electron-Transfer Catalytic Systems for Water Splitting. *Eur. J. Inorg. Chem.* **2014**, *2014* (4), 635–644.

(2) Choi, G. J.; Zhu, Q.; Miller, D. C.; Gu, C. J.; Knowles, R. R. Catalytic Alkylation of Remote C-H Bonds Enabled by Proton-Coupled Electron Transfer. *Nature* **2016**, *539* (7628), 268–271.

(3) Nelson, J. Polymer: Fullerene Bulk Heterojunction Solar Cells. *Mater. Today* **2011**, *14* (10), 462–470.

(4) Tiwari, S.; Singh, A. K.; Joshi, L.; Chakrabarti, P.; Takashima, W.; Kaneto, K.; Prakash, R. Poly-3-Hexylthiophene Based Organic Field-Effect Transistor: Detection of Low Concentration of Ammonia. *Sensors Actuators, B Chem.* **2012**, *171–172*, 962–968.

(5) Romero, E.; Augulis, R.; Novoderezhkin, V. I.; Ferretti, M.; Thieme, J.; Zigmantas, D.; Van Grondelle, R. Quantum Coherence in Photosynthesis for Efficient Solar-Energy Conversion. *Nat. Phys.* **2014**, *10* (9), 676–682.

(6) Ghosh, A. Quantum Chemical Studies of Molecular Structures and Potential Energy Surfaces of Porphyrins and Hemes. *ChemInform* **2003**, *34* (19).

(7) Gust, D.; Moore, T. A.; Moore, A. L. Molecular Mimicry of Photosynthetic Energy and Electron Transfer. *Acc. Chem. Res.* **1993**, *26* (4), 198–205.

(8) Goetz, K. P.; Vermeulen, D.; Payne, M. E.; Kloc, C.; McNeil, L. E.; Jurchescu, O. D. Charge-Transfer Complexes: New Perspectives on an Old Class of Compounds. *J. Mater. Chem. C* **2014**, *2* (17), 3065–3076.

(9) Goetz, K. P.; Vermeulen, D.; Payne, M. E.; Kloc, C.; McNeil, L. E.; Jurchescu, O. D. Charge-Transfer Complexes: New Perspectives on an Old Class of Compounds. *J. Mater. Chem. C* **2014**, *2* (17), 3065–3076.

(10) Chandra, B. K. C.; D'Souza, F. Design and Photochemical Study of Supramolecular Donor-Acceptor Systems Assembled via Metal-Ligand Axial Coordination. *Coord. Chem. Rev.* **2016**, *322*, 104–141.

(11) Melkozernov, A. N.; Barber, J.; Blankenship, R. E. Light Harvesting in Photosystem I Supercomplexes. *Biochemistry* **2006**, *45* (2), 331–345.

(12) Axelrod, H. L.; Okamura, M. Y. The Structure and Function of the Cytochrome C2: Reaction Center Electron Transfer Complex from Rhodobacter Sphaeroides. *Photosynth. Res.* **2005**, *85* (1), 101–114.

(13) Zhang, X. F.; Xi, Q. A Graphene Sheet as an Efficient Electron Acceptor and Conductor for Photoinduced Charge Separation. *Carbon N. Y.* **2011**, *49* (12), 3842–3850.

(14) D'Souza, F.; Ito, O. Supramolecular Donor-Acceptor Hybrids of Porphyrins/Phthalocyanines with Fullerenes/Carbon Nanotubes: Electron Transfer, Sensing, Switching, and Catalytic Applications. *Chem. Commun.* **2009**, No. 33, 4913–4928.

(15) Smilowitz, L.; Sariciftci, N. S.; Wu, R.; Gettinger, C.; Heeger, A. J.; Wudl, F. Photoexcitation Spectroscopy of Conducting-Polymer-C60 Composites: Photoinduced Electron Transfer. *Phys. Rev. B* **1993**, *47* (20), 13835–13842.

(16) Shoaee, S.; Clarke, T. M.; Eng, M. P.; Huang, C.; Barlow, S. Charge Photogeneration in Donor / Acceptor Organic Solar Cells. *Science (80-.).* **2010**, 6736–6767.

(17) Zhang, S.; Ye, L.; Hou, J. Breaking the 10% Efficiency Barrier in Organic Photovoltaics: Morphology and Device Optimization of Well-Known PBDTTT Polymers. *Adv. Energy Mater.* **2016**, *6* (11), 1–20.

(18) Wicklein, A.; Ghosh, S.; Sommer, M.; Würthner, F.; Thelakkat, M. Self-Assembly of Semiconductor Organogelator Nanowires for Photoinduced Charge Separation. *ACS Nano* **2009**, *3* (5), 1107–1114.

(19) Zhou, H.; Yang, L.; You, W. Rational Design of High Performance Conjugated Polymers for Organic Solar Cells. *Macromolecules* **2012**, *45* (2), 607–632.

(20) Lu, L.; Yu, L. Understanding Low Bandgap Polymer PTB7 and Optimizing Polymer Solar Cells Based on IT. *Adv. Mater.* **2014**, *26* (26), 4413–4430.

(21) Hellmann, C.; Paquin, F.; Treat, N. D.; Bruno, A.; Reynolds, L. X.; Haque, S. A.; Stavrinou, P. N.; Silva, C.; Stingelin, N. Controlling the Interaction of Light with Polymer Semiconductors. *Adv. Mater.* **2013**, *25* (35), 4906–4911.

(22) Bakulin, A. A.; Dimitrov, S. D.; Rao, A.; Chow, P. C. Y.; Nielsen, C. B.; Schroeder, B. C.; McCulloch, I.; Bakker, H. J.; Durrant, J. R.; Friend, R. H. Charge-Transfer State Dynamics Following Hole and Electron Transfer in Organic Photovoltaic Devices. *J. Phys. Chem. Lett.* **2013**, *4* (1), 209–215.

(23) Salleo, A. Charge Transport in Polymeric Transistors. *Mater. Today* **2007**, *10* (3), 38–45.

(24) Roy, A.; Beaupré, S.; Cho, S.; Lee, K.; Park, S. H.; Moses, D.; Moon, J. S.; Heeger, A. J.; Coates, N.; Leclerc, M. Bulk Heterojunction Solar Cells with Internal Quantum Efficiency Approaching 100%. *Nat. Photonics* **2009**, *3* (5), 297–302.

(25) Cao, X.; Li, Y.; Liu, B.; Gao, A.; Cao, J.; Yu, Y.; Hei, X. A Fluorescent Conjugated Polymer Photocatalyst Based on Knoevenagel Polycondensation for Hydrogen Production. *New J. Chem.* **2019**, *43* (18), 7093–7098.

(26) Li, H.; Dailey, J.; Kale, T.; Besar, K.; Koehler, K.; Katz, H. E. Sensitive and Selective NO2 Sensing Based on Alkyl- and Alkylthio-Thiophene Polymer Conductance and Conductance Ratio Changes from Differential Chemical Doping. *ACS Appl. Mater. Interfaces* **2017**, *9* (24), 20501–20507.

(27) Chen, D.; Nakahara, A.; Wei, D.; Nordlund, D.; Russell, T. P. P3HT/PCBM Bulk Heterojunction Organic Photovoltaics: Correlating Efficiency and Morphology. *Nano Lett.* **2011**, *11* (2), 561–567.

(28) Street, R. A.; Song, K. W.; Northrup, J. E.; Cowan, S. Photoconductivity Measurements of the Electronic Structure of Organic Solar Cells. *Phys. Rev. B - Condens. Matter Mater. Phys.* **2011**, *83* (16), 1–13.

(29) Ferreira, A. S.; Aguirre, J. C.; Subramaniyan, S.; Jenekhe, S. A.; Tolbert, S. H.; Schwartz, B. J. Understanding How Polymer Properties Control OPV Device Performance: Regioregularity, Swelling, and Morphology Optimization Using Random Poly(3-Butylthiophene-Co-3-Octylthiophene) Polymers. *J. Phys. Chem. C* **2016**, *120* (39), 22115–22125.

(30) Steyrleuthner, R.; Di Pietro, R.; Collins, B. A.; Polzer, F.; Himmelberger, S.; Schubert, M.; Chen, Z.; Zhang, S.; Salleo, A.; Ade, H.; et al. The Role of Regioregularity, Crystallinity, and Chain Orientation on Electron Transport in a High-Mobility n-Type Copolymer. *J. Am. Chem. Soc.* **2014**, *136* (11), 4245–4256.

(31) Untilova, V.; Biskup, T.; Biniek, L.; Vijayakumar, V.; Brinkmann, M. Control of Chain Alignment and Crystallization Helps Enhance Charge Conductivities and Thermoelectric Power Factors in Sequentially Doped P3HT:F4TCNQ Films. *Macromolecules* **2020**.

(32) Zhang, G.; Huber, R. C.; Ferreira, A. S.; Boyd, S. D.; Luscombe, C. K.; Tolbert, S. H.; Schwartz, B. J. Crystallinity Effects in Sequentially Processed and Blend-Cast Bulk-Heterojunction Polymer/Fullerene Photovoltaics. *J. Phys. Chem. C* **2014**, *118* (32), 18424–18435.

(33) Ghosh, R.; Luscombe, C. K.; Hambsch, M.; Mannsfeld, S. C. B.; Salleo, A.; Spano, F. C. Anisotropic Polaron Delocalization in Conjugated Homopolymers and Donor–Acceptor Copolymers. *Chem. Mater.* **2019**, acs.chemmater.9b01704.

(34) Hamidi-Sakr, A.; Biniek, L.; Bantignies, J. L.; Maurin, D.; Herrmann, L.; Leclerc, N.; Lévêque, P.; Vijayakumar, V.; Zimmermann, N.; Brinkmann, M. A Versatile Method to Fabricate Highly In-Plane Aligned Conducting Polymer Films with Anisotropic Charge Transport and Thermoelectric Properties: The Key Role of Alkyl Side Chain Layers on the Doping Mechanism. *Adv. Funct. Mater.* **2017**, *27* (25), 1–13.

(35) Gu, K. L.; Zhou, Y.; Gu, X.; Yan, H.; Diao, Y.; Kurosawa, T.; Ganapathysubramanian, B.; Toney, M. F.; Bao, Z. Tuning Domain Size and Crystallinity in Isoindigo/PCBM Organic Solar Cells via Solution Shearing. *Org. Electron.* **2017**, *40*, 79–87.

(36) Shao, M.; Keum, J. K.; Kumar, R.; Chen, J.; Browning, J. F.; Das, S.; Chen, W.; Hou, J.; Do, C.; Littrell, K. C.; et al. Understanding How Processing Additives Tune the Nanoscale Morphology of High Efficiency Organic Photovoltaic Blends: From Casting Solution to Spun-Cast Thin Film. *Adv. Funct. Mater.* **2014**, *24* (42), 6647–6657.

(37) Chen, H.; Hsiao, Y. C.; Hu, B.; Dadmun, M. Tuning the Morphology and Performance of Low Bandgap Polymer:Fullerene Heterojunctions via Solvent Annealing in Selective Solvents. *Adv. Funct. Mater.* **2014**, *24* (32), 5129–5136.

(38) Clark, A. P. Z.; Shi, C.; Ng, B. C.; Wilking, J. N.; Ayzner, A. L.; Stieg, A. Z.; Schwartz, B. J.; Mason, T. G.; Rubin, Y.; Tolbert, S. H. Self-Assembling Semiconducting Polymers - Rods and Gels from Electronic Materials. *ACS Nano* **2013**, *7* (2), 962–977.

(39) Winchell, K. J.; Yee, P. Y.; Li, Y. L.; Beren, C.; Thompson, R. J.; Salamat, C. Z.; Jordan, R. S.; Schwartz, B. J.; Gelbart, W. M.; Tolbert, S. H. Designing Cationic Conjugated Polymers for Amphiphilic Assembly into Micelles with Straight Chains. 1–30.

(40) Huber, R. C.; Ferreira, A. S.; Thompson, R.; Kilbride, D.; Knutson, N. S.; Devi, L. S.;

Toso, D. B.; Challa, J. R.; Zhou, Z. H.; Rubin, Y.; et al. Long-Lived Photoinduced Polaron Formation in Conjugated Polyelectrolyte-Fullerene Assemblies. *Science (80-.).* **2015**, *348* (6241), 1340–1343.

(41) Huber, R. C.; Ferreira, A. S.; Aguirre, J. C.; Kilbride, D.; Toso, D. B.; Mayoral, K.; Zhou, Z. H.; Kopidakis, N.; Rubin, Y.; Schwartz, B. J.; et al. Structure and Conductivity of Semiconducting Polymer Hydrogels. *J. Phys. Chem. B* **2016**, *120* (26), 6215–6224.

(42) Mertens, H. D. T.; Svergun, D. I. Structural Characterization of Proteins and Complexes Using Small-Angle X-Ray Solution Scattering. *J. Struct. Biol.* **2010**, *172* (1), 128–141.

(43) Putnam, D. K.; Lowe, E. W.; Meiler, J. Reconstruction of Saxs Profiles From Protein Structures. *Comput. Struct. Biotechnol. J.* **2013**, *8* (11), e201308006.

(44) Boldon, L.; Laliberte, F.; Liu, L. Review of the Fundamental Theories behind Small Angle X-Ray Scattering, Molecular Dynamics Simulations, and Relevant Integrated Application. *Nano Rev.* **2015**, *6* (1), 25661.

(45) Hammouda, B. A New Guinier-Porod Model. *J. Appl. Crystallogr.* **2010**, *43* (4), 716–719.

(46) Liu, H.; Zwart, P. H. Determining Pair Distance Distribution Function from SAXS Data Using Parametric Functionals. *J. Struct. Biol.* **2012**, *180* (1), 226–234.

(47) Related, P. Reports on Progress in Physics Related Content Small-Angle Scattering Studies of Biological Macromolecules in Solution Small-Angle Scattering Studies of Biological Macromolecules in Solution. **2003**.

(48) Jiang, Y.; Lu, L.; Yang, M.; Zhan, C.; Xie, Z.; Verpoort, F.; Xiao, S. Taking the Place of Perylene Diimide: Perylene Tetracarboxylic Tetraester as a Building Block for Polymeric Acceptors to Achieve Higher Open Circuit Voltage in All-Polymer Bulk Heterojunction Solar Cells. *Polym. Chem.* **2013**, *4* (23), 5612–5620.

(49) Liu, Y. X.; Summers, M. A.; Scully, S. R.; McGehee, M. D. Resonance Energy Transfer from Organic Chromophores to Fullerene Molecules. *J. Appl. Phys.* **2006**, *99* (9), 1–4.

(50) Sinturel, C.; Vayer, M.; Morris, M.; Hillmyer, M. A. Solvent Vapor Annealing of Block Polymer Thin Films. *Macromolecules* **2013**, *46* (14), 5399–5415.

(51) Wu, C.; McNeill, J. Swelling-Controlled Polymer Phase and Fluorescence Properties of Polyfluorene Nanoparticles. *Langmuir* **2008**, *24* (11), 5855–5861.

(52) Sun, K.; Xiao, Z.; Hanssen, E.; Klein, M. F. G.; Dam, H. H.; Pfaff, M.; Gerthsen, D.; Wong, W. W. H.; Jones, D. J. The Role of Solvent Vapor Annealing in Highly Efficient Air-Processed Small Molecule Solar Cells. *J. Mater. Chem. A* **2014**, *2* (24), 9048–9054.

(53) Hu, Y.; Chen, S.; Zhang, L.; Zhang, Y.; Yuan, Z.; Zhao, X.; Chen, Y. Facile Approach to Perylenemonoimide with Short Side Chains for Nonfullerene Solar Cells. *J. Org. Chem.* **2017**, *82* (11), 5926–5931.